



THE UNIVERSITY *of* EDINBURGH

Edinburgh Research Explorer

A mouse model of human mitofusin 2-related lipodystrophy exhibits adipose-specific mitochondrial stress and reduced leptin secretion

Citation for published version:

Mann, JP, Duan, X, Patel, S, Tábara, LC, Scurria, F, Alvarez-Guaita, A, Haider, A, Luijten, I, Page, M, Protasoni, M, Lim, K, Virtue, S, O'Rahilly, S, Armstrong, M, Prudent, J, Semple, RK & Savage, DB 2023, 'A mouse model of human mitofusin 2-related lipodystrophy exhibits adipose-specific mitochondrial stress and reduced leptin secretion', *eLIFE*, vol. 12. <https://doi.org/10.7554/eLife.82283>

Digital Object Identifier (DOI):

[10.7554/eLife.82283](https://doi.org/10.7554/eLife.82283)

Link:

[Link to publication record in Edinburgh Research Explorer](#)

Document Version:

Peer reviewed version

Published In:

eLIFE

General rights

Copyright for the publications made accessible via the Edinburgh Research Explorer is retained by the author(s) and / or other copyright owners and it is a condition of accessing these publications that users recognise and abide by the legal requirements associated with these rights.

Take down policy

The University of Edinburgh has made every reasonable effort to ensure that Edinburgh Research Explorer content complies with UK legislation. If you believe that the public display of this file breaches copyright please contact openaccess@ed.ac.uk providing details, and we will remove access to the work immediately and investigate your claim.



1 **A mouse model of human mitofusin 2-related lipodystrophy exhibits adipose-**
2 **specific mitochondrial stress and reduced leptin secretion**

3

4 Mann JP¹

5 Duan X¹

6 Patel S¹

7 Tábara LC²

8 Scurria F¹

9 Alvarez-Guaita A¹

10 Haider A¹

11 Luijten I³

12 Page M⁴

13 Protasoni M²

14 Lim K¹

15 Virtue S¹

16 O'Rahilly S¹

17 Armstrong M⁵

18 Prudent J²

19 *Semple RK^{2,6}

20 *Savage DB¹

21

22 **Affiliations**

23 1. University of Cambridge Metabolic Research Laboratories, Wellcome Trust-MRC Institute
24 of Metabolic Science, Cambridge, CB2 0QQ, UK

25 2. Medical Research Council Mitochondrial Biology Unit, University of Cambridge,
26 Cambridge, UK

27 3. Centre for Cardiovascular Science, University of Edinburgh, Edinburgh, UK

28 4. UCB Biopharma UK, Bath Road, Slough, UK

29 5. UCB Pharma, Chemin du Foriest 1, 1420 Braine l'Alleud, Belgium

30 6. MRC Human Genetics Unit, Institute of Genetics and Cancer, University of Edinburgh,
31 Edinburgh, UK

32

33 *Joint senior and corresponding authors

34 **Correspondence:**

35 Prof. David B. Savage

36 Metabolic Research Laboratories

37 Level 4, Institute of Metabolic Science

38 Addenbrooke's Hospital
39 Cambridge, CB2 0QQ
40 Tel: +44 1223 767932; email: dbs23@cam.ac.uk

41 OR

42 Prof. Robert K. Semple
43 University of Edinburgh Centre for Cardiovascular Science
44 Queen's Medical Research Institute
45 47 Little France Crescent
46 Edinburgh, EH16 4TJ
47 Tel: +44 131 242 6051; email: rsemple@ed.ac.uk

48

49 **Financial Support**

50 **Authors' declaration of personal interests:**

51 The authors have no conflicts of interest to declare.

52

53 **Funding:**

54 This work was supported by the Wellcome Trust (grant Nos. WT 210752 to R.K.S., WT
55 219417 to D.B.S., WT 216329/Z/19/Z to J.P.M, and WT 214274 to S.O'R., respectively), the
56 National Institute for Health Research (NIHR) Cambridge Biomedical Research Centre, the
57 Swedish Research Council (to I.L.) and the Medical Research Council UK (MRC;
58 MC_UU_00015/7 and MC_UU_00028/5 to J.P). The Disease Model Core, Biochemistry
59 Assay Lab, the Histology Core and the Genomics and Transcriptomics Core are funded by
60 MRC MC_UU_00014/5, MRC MRC_MC_UU_12012/5, and a Wellcome Trust Strategic
61 Award (208363/Z/17/Z). L.C.T. was a recipient of a Ramon Areces postdoctoral fellowship.

62 The funders had no role in study design, data collection and interpretation, or submitting the
63 work for publication.

64

65 **Acknowledgements**

66 We are grateful to the team at the University of Cambridge Advanced Imaging Centre for
67 access to their facilities and for their expertise. We thank the Disease Model Core from the
68 Wellcome-MRC Institute of Metabolic Science for their technical assistance in animal work.

69 We also thank the Genomics and Transcriptomics core, the Histology core and G. Strachan
70 from the Imaging core for technical assistance. Finally we thank M. Mimmack for his
71 assistance with *in vitro* experiments.

72

73

74

75 **Abstract**

76 Mitochondrial dysfunction has been reported in obesity and insulin resistance, but primary
77 genetic mitochondrial dysfunction is generally not associated with these, arguing against a
78 straightforward causal relationship. A rare exception, recently identified in humans, is a
79 syndrome of lower body adipose loss, leptin-deficient severe upper body adipose
80 overgrowth, and insulin resistance caused by the p.Arg707Trp mutation in *MFN2*, encoding
81 mitofusin 2. How the resulting selective form of mitochondrial dysfunction leads to tissue-
82 and adipose depot-specific growth abnormalities and systemic biochemical perturbation is
83 unknown. To address this, *Mfn2*^{R707W/R707W} knock-in mice were generated and phenotyped
84 on chow and high fat diets. Electron microscopy revealed adipose-specific mitochondrial
85 morphological abnormalities. Oxidative phosphorylation measured in isolated mitochondria
86 was unperturbed, but the cellular integrated stress response was activated in adipose tissue.
87 Fat mass and distribution, body weight, and systemic glucose and lipid metabolism were
88 unchanged, however serum leptin and adiponectin concentrations, and their secretion from
89 adipose explants were reduced. Pharmacological induction of the integrated stress response
90 in wild-type adipocytes also reduced secretion of leptin and adiponectin, suggesting an
91 explanation for the *in vivo* findings. These data suggest that the p.Arg707Trp MFN2 mutation
92 selectively perturbs mitochondrial morphology and activates the integrated stress response
93 in adipose tissue. In mice, this does not disrupt most adipocyte functions or systemic
94 metabolism, whereas in humans it is associated with pathological adipose remodelling and
95 metabolic disease. In both species, disproportionate effects on leptin secretion may relate to
96 cell autonomous induction of the integrated stress response.

97

98

99

100 **Keywords**

101 Mitochondria, mitofusin, adipose tissue, integrated stress response, leptin

102

103

104

105 **Introduction**

106 Mitochondrial dysfunction has been implicated in the pathogenesis of a wide range of
107 congenital and acquired conditions¹⁻³. However, despite being central to cellular energy
108 homeostasis, there has been little mechanistic evidence of a causal role for deranged
109 mitochondrial function in human adiposity. Instead, most patients with inherited
110 mitochondrial disorders have a neurological phenotype, though multisystem involvement is
111 common^{1,4}. This is true for disorders caused by many different mutations affecting
112 mitochondrial proteins, whether encoded by the mitochondrial or nuclear genome. The
113 mechanisms underlying such tissue-selective disease manifestations even in the face of
114 constitutional mutations are unclear, but differing tissue requirements for oxidative
115 phosphorylation, and interactions between the nuclear and mitochondrial genome may play
116 a role⁵⁻⁷.

117 We⁸ and others⁹⁻¹³ recently identified biallelic R707W mutations in the nuclear *MFN2* gene in
118 patients with a remarkable adipose phenotype characterised by extreme upper body
119 adiposity (lipomatosis) and lower body lipodystrophy. Affected patients also showed non-
120 alcoholic fatty liver disease, dyslipidaemia and insulin resistant type 2 diabetes, likely
121 secondary to the changes in adipose tissue. *MFN2* encodes mitofusin 2, a mitochondrial
122 outer membrane protein that plays a key role in mitochondrial fusion and tethering to other
123 organelles¹⁴. Like patients with heterozygous complete loss-of-function mutations in *MFN2*,
124 patients with the R707W mutation also often exhibit axonal peripheral neuropathy known as
125 Charcot-Marie Tooth type 2A (CMT2A)¹⁵⁻¹⁷, but the adipose and metabolic phenotype has
126 uniquely been associated with the R707W allele to date. Evidence suggesting that the *MFN2*
127 R707W mutation does disrupt mitochondrial function in humans includes elevated serum
128 lactate in affected patients, abnormal mitochondrial morphology seen on transmission
129 electron microscopy of affected adipose tissue⁸, and strong transcriptomic signatures of
130 mitochondrial dysfunction and activation of the integrated stress response (ISR)⁴ in the same
131 tissue.

132 Despite normal or raised whole body adipose mass, and the relatively normal histological
133 appearance of lipomatous upper body fat, plasma leptin concentrations were very low in the
134 patients reported by Rocha *et al.*⁸. This observation was supported by Sawyer *et al.* who
135 reported one patient with undetectable serum leptin (<0.6 ng/mL)⁹ and Capel *et al.* who
136 described five patients with serum leptin concentrations <1.6 ng/mL despite body mass
137 indices (BMIs) within the normal range¹⁰. Leptin is a critical endocrine signal of adipose
138 stores and yet what determines the rate of adipocyte leptin secretion remains poorly
139 understood¹⁸. This surprising observation thus offered a rare opportunity to address this
140 important issue. Circulating leptin concentration correlates with fat mass, and is usually

141 higher in women than men, with some adipose depots reported to release more than
142 others¹⁹. Leptin secretion is increased by insulin stimulation²⁰ but this effect is modest in the
143 context of serum leptin concentrations. Adipose depots that secrete higher leptin have
144 increased *LEP* mRNA and, at least *in vitro*, *LEP* mRNA increases in response to insulin
145 stimulation²¹.

146 Most neuropathy-associated *MFN2* mutations are located within the protein's GTPase
147 domain²²⁻²⁵, but to date, all patients with *MFN2*-associated multiple symmetric lipomatosis
148 (MSL) have had at least one R707W allele. Most cases have been homozygous for the
149 R707W mutation, with others compound heterozygous for R707W and a second, functionally
150 null mutation⁸⁻¹³. Arginine 707 lies in the highly conserved heptad-repeat (HR)2 region of
151 *MFN2* but consensus on the precise orientation and/or function of this domain has not yet
152 been established²⁶. The dominant model holds that the HR2 domains of Mitofusin 1 (*MFN1*)
153 and/or *MFN2* face the cytosol and interact in *trans*, forming mitofusin homodimers or
154 heterodimers required for mitochondrial fusion and tethering to other organelles^{27,28}. The
155 R707W mutation may disrupt this binding and subsequent *MFN* oligomerisation and
156 mitochondrial fusion/tethering.

157 Global knock-out of the core mitochondrial fusion-fission machinery proteins *Mfn1*, *Mfn2*,
158 *Opa1*, and *Drp1* in mice confers embryonic lethality in all cases²⁹⁻³¹. Two homozygous loss-
159 of-function *Mfn2* knock-ins - H361Y and R94W - have also been reported. H361Y was also
160 embryonically lethal due to complete loss of detectable *Mfn2* protein³², while homozygous
161 R94W mice died at post-natal day 1³³. *Mfn2*^{R94W} is expressed but is GTPase defective,
162 increasing mitochondrial fragmentation and preventing formation of *Mfn2* homodimers³⁴.

163 Multiple tissue-specific knock-outs of *Mfn2* (and/or *Mfn1*) have been studied, including three
164 in adipose tissue³⁵⁻³⁸. Adipose-specific *Adipoq::Cre Mfn2* knock-out increased fat mass,
165 attributed to reduced energy expenditure, whether it occurred in embryonic life³⁶ or was
166 induced by tamoxifen in adult mice³⁸, with ultrastructural evidence of more rounded
167 mitochondria with fewer lipid droplet contacts³⁶. Both *Adipoq::Cre* driven (adipose-specific)
168 and *Ucp1::Cre* driven (brown adipose-specific) *Mfn2* knock-out also caused cold intolerance
169 with "whitened" brown adipose tissue³⁷. Plasma leptin concentrations were not reported in
170 *Adipoq-Cre* or *Ucp1::Cre Mfn2* knock-outs, but leptin concentration was higher and
171 adiponectin concentration lower in the tamoxifen-inducible adult *Adipoq::Cre Mfn2* knockout
172 model³⁸.

173 These studies suggest that *Mfn2* has a non redundant role in adipose tissues, but findings to
174 date are not readily reconcilable with the phenotype observed in humans with the *MFN2*^{R707W}
175 mutation. We thus generated and characterised mice homozygous for *Mfn2*^{R707W} to

176 determine the extent of tissue-specific manifestations of mitochondrial dysfunction and to
177 interrogate the effect of this mutant on adipose leptin secretion.
178

179 Results

180 *Generation of Mfn2^{R707W/R707W} mice*

181 *Mfn2^{R707W/R707W}* mice were generated by CRISPR-Cas9 genomic engineering using an
182 ssODN (single-stranded oligo donor) template recoding Arginine to Tryptophan in codon 707
183 (**Figure 1A**). A single round of targeting yielded one founder (F0) mouse (**Figure 1B**) which
184 was used to expand a colony on a C57/BL6J background. An additional silent mutation
185 introducing an EcoRV restriction site was introduced to facilitate genotyping (**Figure 1C, D**).
186 We first compared expression of Mfn2 and its paralogue, Mfn1, in knock-in (KI) mice and
187 wild-type (WT) littermates in order to determine if the R707W change perturbed expression
188 of the mutant Mfn2 protein and/or resulted in a compensatory change in Mfn1. We observed
189 no consistent differences in Mfn1 or Mfn2 expression, relative to WT, in inguinal white
190 adipose tissue (WAT), liver, heart, or skeletal muscle in both chow and high fat diet (HFD)
191 fed mice (**Figure 1E, Figure 1-Figure supplements 1-4**). However, in brown adipose tissue
192 (BAT) expression of Mfn1 was lower in KI than in WT mice fed with chow diet for 6 months
193 (**Figure 1-Figure supplement 1D and 2D**). Similarly, expression of Mfn1 was lower in KI
194 than WT mice after only 4 weeks of chow diet (**Figure 1-Figure supplement 1G and 2G**). In
195 HFD fed mice, both Mfn1 and Mfn2 expression was lower in BAT in KI compared to WT
196 mice (**Figure 1E, Figure 1-Figure supplement 3D and 4D**). In epididymal WAT, expression
197 of Mfn1 was also lower in KI than in WT mice fed with chow diet (**Figure 1-Figure**
198 **supplement 1F and 2F**), but no differences were observed in HFD fed mice (**Figure 1-**
199 **Figure supplement 3F and 4F**). We interpret these data as suggesting that the R707W
200 missense mutation does not directly reduce expression of Mfn2, nor does it result in a
201 compensatory change in Mfn1 in most tissues. However, in BAT the data suggests that the
202 cellular perturbation induced in brown adipocytes is associated with a very modest reduction
203 in expression of Mfn1 and 2.

204 *Mfn2^{R707W/R707W} mice show adipose-selective alterations of mitochondrial structure* 205 *and function*

206 Next, we used transmission electron microscopy (TEM) to examine mitochondrial
207 ultrastructure (**Figure 2A**). In BAT, mitochondria from KI mice had a tendency to exhibit a
208 decreased mitochondrial perimeter compared to WT mice (**Figure 2B**), but significantly
209 reduced size, assessed by the mitochondrial cross-sectional length/ width aspect ratio
210 analysis (**Figure 2C**), indicating that Mfn2^{R707W} leads to mitochondrial fragmentation in BAT.
211 Double membrane-bound structures representing autophagosomes consistent with
212 mitophagy were observed in lipomatous adipose tissue from human patients with the
213 MFN2^{R707W} mutation⁸, but these were not identified in the murine tissues examined.

214 Mitofusins may mediate contact between mitochondria and lipid droplets³⁶, and the extent of
215 these contacts was reduced in BAT from KI animals (**Figure 2D**). In addition, mitochondrial
216 cristae were disrupted in KI compared to WT animals (**Figure 2E**). In both inguinal (**Figure**
217 **2-figure supplement 1A-C**) and epididymal WAT (**Figure 2-figure supplement 1D-F**),
218 similar mitochondrial fragmentation and cristae defects were observed. In contrast, no
219 change in mitochondrial morphology, cristae number, or cristae structure was seen in the
220 heart, skeletal muscle or liver of KI mice (**Figure 2-figure supplement 2**).

221 Perturbed mitochondrial dynamics have been associated with decreased mitochondrial DNA
222 (mtDNA) content, as replication of mtDNA relies on balanced fusion and fission³⁹. In
223 *Mfn2*^{R707W/R707W} mice, mtDNA was reduced in BAT in both diet conditions, but not in any
224 other tissue analysed (WAT, heart, skeletal muscle, or liver) (**Figure 2F-G**). Immunoblotting
225 of electron transport chain components from chow fed animals showed no changes in liver
226 or heart (**Figure 2-Figure supplement 3A-B and 4A-B**). However, mtCo1 (complex IV) and
227 Ndufb8 (complex I) were reduced in KI mice in brown and white adipose tissue (**Figure 2-**
228 **Figure supplement 3C-E and 4C-E**). In addition, Uqcrc2 (complex III) was also lower in
229 inguinal WAT.

230 To determine if these changes altered mitochondrial oxidative phosphorylation, we assessed
231 oxidative capacity in freshly isolated mitochondria from BAT and liver by high resolution
232 respirometry using Oroboros Oxygraphy. No significant differences were detected between
233 WT and KI mitochondria (**Figure 2-figure supplement 5A-B**). We further assessed
234 mitochondrial function in BAT *in vivo* by challenging mice with noradrenaline in cold (10
235 degrees) or thermoneutral (30 degrees) conditions to determine maximum thermogenic
236 capacity. Again, despite a trend towards reduced thermogenic capacity in KI animals, the
237 difference was not significant, and both groups manifested the expected increase in energy
238 expenditure at 10°C (**Figure 2-figure supplement 5C-G**).

239 *Body composition and metabolic phenotype of Mfn2*^{R707W/R707W} mice

240 We next assessed whether *Mfn2*^{R707W/R707W} mice phenocopy the severely abnormal adipose
241 topography and metabolic abnormalities of patients harbouring the same mutations. Male
242 mice fed with either chow or HFD for up to 6 months were assessed. Whole body mass and
243 composition, and masses of individual adipose depots and other organs were similar in KI
244 and WT mice throughout the study period (**Table 1, Figure 3A-C & Figure 3-figure**
245 **supplement 1A-D**). Moreover, no difference in hepatic steatosis nor lipid droplet size was
246 detected histologically in BAT or WAT (**Figure 3D-E & Figure 3-figure supplement 1F-G**).
247 In keeping with the normal body composition, fasting serum glucose, insulin, triglycerides,
248 cholesterol, lactate, and liver transaminase concentrations showed no difference between

249 WT and KI mice (**Figure 3F-I & Figure 3-figure supplement 1E, H**). There was also no
250 differences in hepatic expression of genes related to lipid metabolism or steatohepatitis
251 (**Figure 3-figure supplement 1I**). Dynamic testing of glucose and insulin tolerance was also
252 similar between genotypes (**Figure 3G-K**).

253

254 Similar results were observed in female mice harbouring the *Mfn2*^{R707W} mutation.
255 Specifically, there was no difference in body weight, fat mass, fasting glucose or insulin
256 between high fat fed WT and KI mice (**Figure 3-Figure supplement 2A-C**).

257 *Adipose-tissue specific activation of the integrated stress response in Mfn2*^{R707W}
258 *mice*

259 Mitochondrial dysfunction is sensed by cells, and triggers a series of adaptive responses to
260 maintain mitonuclear balance and cellular homeostasis⁴⁰. Precise sensing and transducing
261 mechanisms vary among different forms of mitochondrial perturbation⁴¹, and show some
262 redundancy⁴². Although details of the integration of these mechanisms in different tissue and
263 cellular contexts are not fully elucidated, it is clear that the transcription factor Atf4 plays a
264 crucial role⁴³. Atf4 is translationally upregulated following phosphorylation of eIF2 α , which is
265 a point of convergence of several cellular stress sensing pathways. The canonical eIF2 α
266 kinase HRI is most closely implicated in linking mitochondrial dysfunction to eIF2 α
267 phosphorylation^{44,45}, but mTORC1 appears to play a role in Atf4 upregulation independently
268 of eIF2 α phosphorylation⁴⁶. The response to sustained mitochondrial dysfunction overlaps
269 significantly with the response to many other cellular stressors including unfolded protein
270 induced stress (i.e. the unfolded protein response (UPR)), and is best characterised as a
271 cellular ISR⁴⁷.

272

273 Strong transcriptional evidence of ISR activation was found in adipose tissue of patients with
274 *MFN2*^{R707W}-related lipodystrophy⁸. We thus screened multiple tissues from the KI mice for
275 ISR activation. mRNA levels of *Atf4*, *Atf5*, and *Ddit3* (Chop), all sentinel markers of the ISR,
276 were increased in BAT and epididymal WAT of KI mice (**Figure 4A-C**). *Ddit3* was also
277 higher in inguinal WAT from KI animals. mRNA levels of *Atf4*, *Atf5*, and *Ddit3* (Chop) were
278 unchanged in liver, heart, and skeletal muscle, except for a 1.4-fold rise in *Atf5* (p.adj = 0.03)
279 in skeletal muscle only. Phosphorylation of eIF2 α and protein expression of Mthfd2, an Atf4-
280 upregulated enzyme playing a rate-limiting role in mitochondrial one carbon metabolism⁴⁸⁻⁵⁰,
281 were also both strongly increased in BAT and in WAT in KI mice (**Figure 4D-F & Figure 4-
282 figure supplement 1E-G and 2**), whereas they were unchanged in the liver, skeletal muscle
283 and heart. mRNA expression of two important secreted mediators of the organismal
284 metabolic response to mitochondrial dysfunction, *Gdf15* and *Fgf21*, trended towards an

285 increase in adipose tissue, but serum concentrations were unchanged in KI mice (**Figure 4-**
286 **figure supplement 1A-D**). This differs from observations in patients with MFN2^{R707W}-related
287 lipodystrophy⁵⁰⁻⁵², and may relate to the fact that such patients manifest non-alcoholic fatty
288 liver disease, which was not seen in the KI animals.

289

290 Given the recent evidence implicating HRI kinase as a key mediator of eIF2 α
291 phosphorylation induced by mitochondrial dysfunction^{44,45}, we next sought to determine if
292 this pathway was active in R707W KI mice. The pathway activating HRI kinase was reported
293 to be initiated by activation of the metalloendopeptidase Oma1^{53,54}. In addition to cleaving
294 Dele1⁵⁵, which activates HRI kinase, Oma1 also cleaves Opa1 (optic atrophy type 1)⁵⁶ and
295 itself upon activation. We thus immunoblotted tissue lysates for Opa1 and Oma1. No
296 evidence for Oma1 activity was found in liver, skeletal muscle or heart (**Figure 4-figure**
297 **supplement 3**). In BAT, we did detect a modest change in Oma1 expression and a slight
298 increase in the short / long Opa1 ratio, providing some evidence that the pathway may be
299 activated (**Figure 4-figure supplement 4**). However, the differences observed were small
300 precluding a confident conclusion at this stage. In WAT, clear bands for all five Opa1 forms
301 could not be visualised on repeated attempts and so we did not attempt to quantify the data.
302 Current WAT data thus do not suggest Oma1 activation (**Figure 4-figure supplement 4C-**
303 **D**). As far as we are aware, Oma1 activation has yet to be examined in Mfn2 tissue-specific
304 KO models so we cannot infer anything from those studies either. Thus we conclude that the
305 ISR is activated in selected tissues in the KI mice, but the question of how this is linked to
306 the Mfn2 R707W mutation remains open.

307 To obtain an unbiased view of the transcriptional consequences of the lipodystrophy-
308 associated Mfn2 mutation, we next applied bulk RNA sequencing (RNAseq) to BAT and
309 inguinal WAT from HFD fed mice. Inguinal, rather than epididymal, WAT was selected as
310 subcutaneous adipose tissue is predominantly affected in human MFN2-related and other
311 partial lipodystrophies⁵⁷. Induction of the ISR was confirmed in both BAT and WAT (**Figure**
312 **4G-I & Figure 4-figure supplement 5**), with the “unfolded protein response” gene set, a
313 surrogate for the ISR, the top upregulated gene set in BAT and 6th in inguinal WAT. *Atf5*
314 and *Mthfd2* were confirmed among the most highly upregulated mRNAs in both tissues, and
315 a range of other well established ISR genes also showed increased expression. These
316 included *Ddit3* (Chop), *Trib3*, an Atf4-driven ISR component that exerts negative feedback
317 on the ISR, and *Gadd45a*, involved in ISR-induced G2/M checkpoint arrest⁵⁸.

318 The top upregulated gene set in inguinal WAT was “oxidative phosphorylation”, driven solely
319 by increased expression of nuclear-encoded mitochondrial genes (**Figure 4-figure**
320 **supplement 1H**). In contrast, mitochondria-encoded genes were nearly universally

321 downregulated (**Figure 4-figure supplement 1I**), recapitulating the pattern seen in affected
322 human WAT⁸. In BAT, a similar but weaker pattern was seen on inspection of heatmaps, but
323 this was not sufficient to reach statistical significance.

324 Another finding common to mouse and human was the transcriptional evidence of mTORC1
325 activation. The “mTorc signalling” gene set was the second most upregulated group in BAT
326 and third most upregulated in WAT (**Figure 4-figure supplement 5B&E**). This activation is
327 consistent with the proposed role for mTORC1 in mediating the proximal ISR⁴⁶, and is of
328 interest given accumulating evidence that the mTORC1 inhibitor sirolimus may exert
329 beneficial effects in various mitochondrial diseases⁵⁹.

330 Although no increase in adipose tissue mass was seen in *Mfn2*^{R707W} mice the “adipogenesis”
331 gene set was upregulated in inguinal WAT under both diet conditions (**Figure 4H & Figure**
332 **4-figure supplement 5B**). However, closer inspection revealed a mixed profile of individual
333 gene expression. The most consistent finding was downregulation of the adipokine-encoding
334 mature adipocyte genes *Adipoq* and *Lep* in *Mfn2*^{R707W} mice (discussed below). *Adipoq* and
335 *Lep* were also downregulated in BAT (fold changes 0.64 (p.adj=6.3x10⁻⁴) and 0.31 (p.adj=0.03)
336 respectively), but the adipogenesis gene set was not enriched overall (**Figure 4-figure**
337 **supplement 5E**).

338 To assess for other potential drivers of adipose hyperplasia, we also examined
339 downregulated gene sets. The signature of epithelial-mesenchymal transition (EMT) was the
340 most strongly down-regulated set in mouse BAT and WAT (**Figure 4I & Figure 4-figure**
341 **supplement 5C, F**), and was also previously found to be downregulated in overgrown
342 human WAT in MFN2-associated multiple symmetric lipomatosis⁸. In bulk transcriptomic
343 data it is not possible to discern the cell type(s) responsible for this consistent signature.
344 However TGFβ family ligands are important mediators of EMT, some family members inhibit
345 adipogenesis⁶⁰, and they also play important roles in regulating mitochondrial function and in
346 responding to mitochondrial dysfunction⁶¹.

347 We next sought to assess whether the increased demand for adipose expansion imposed by
348 HFD feeding exacerbates the transcriptional consequences of *Mfn2* R707W homozygosity.
349 RNAseq was thus undertaken of inguinal WAT from mice maintained on HFD for 6 months.
350 Comparison to WT animals revealed strikingly concordant findings to those seen in chow-fed
351 mice (**Figure 4-figure supplement 5G**). No general differences were seen in the magnitude
352 of transcriptional changes induced by *Mfn2* R707W homozygosity between conditions.
353 Oxidative phosphorylation, unfolded protein response and adipogenesis genes and Hallmark
354 gene sets were strongly upregulated, whereas genes in the EMT set were downregulated in
355 KI mice on both diets. An exception was the group of mRNAs related to cholesterol

356 homeostasis, for which diet strikingly modified the effect of genotype. They were the top
357 downregulated gene set in inguinal WAT in HFD-fed animals but were not significantly
358 altered on chow in the same depot and were upregulated in BAT (**Figure 4I & Figure 4-
359 figure supplement 5E**). Lower expression of key enzymes in cholesterol metabolism (e.g.
360 Hydroxymethylglutaryl-CoA synthase (*Hmgcs1*), mevalonate kinase (*Mvk*), and squalene
361 monooxygenase (*Sqle*)) in WAT on HFD is consistent with the response to inhibition of the
362 mitochondrial respiratory chain in primary human fibroblasts⁶².

363 *Lower circulating leptin and adiponectin in mice homozygous for Mfn2^{R707W}*

364 One of the most striking aspects of the *Mfn2^{R707W}*-associated lipodystrophy phenotype is the
365 low or undetectable serum leptin concentration despite abundant whole body adiposity,
366 accounted for mostly by excess upper body adipose tissue of relatively normal histological
367 appearance⁸. Serum adiponectin concentrations are also low, however this is in keeping with
368 the “adiponectin paradox” widely seen in obesity with insulin resistance⁶³. Mirroring these
369 human observations, KI mice showed low serum leptin and adiponectin concentrations on
370 both chow and HFD (**Figure 5A-C**), though unlike humans, the mice had normal fat mass
371 and insulin sensitivity. In both WT and KI mice serum leptin concentrations correlated
372 positively with whole body adiposity on chow and HFD, but a generalised linear model
373 revealed marked attenuation of the relationship between serum leptin concentration and
374 adipose mass in the KI mice (**Figure 5C & Figure 5 supplement 1A**). Immunoblotting of
375 WAT samples from KI mice fed a HFD confirmed that both leptin and adiponectin expression
376 was reduced (**Figure 5-Figure supplement 2**). Findings were similar in female mice, in
377 which serum adiponectin was significantly lower in KI mice (**Figure 3-Figure supplement
378 2F**), with a trend towards lower leptin (**Figure 3-Figure supplement 2G-I**).

379 RNAseq showed *Lep* mRNA in inguinal WAT to be lower in *Mfn2^{R707W}* than in WT mice under
380 both chow (fold change 0.35; p.adj = 3.2×10^{-4} , **Figure 4-Figure Supplement 5A**) and HFD
381 (fold change 0.66; p.adj = 5.3×10^{-4} , **Figure 4G**). *Adipoq* mRNA was also significantly lower in
382 chow (fold change 0.66; p.adj = 2.7×10^{-4} , **Figure 4-Figure Supplement 5A**) and HF fed mice
383 (fold change 0.57; p.adj = 3.3×10^{-15} , **Figure 4G**). RT-qPCR analysis confirmed lower *Lep*
384 mRNA in epididymal WAT from chow fed *Mfn2^{R707W}* animals (**Figure 5D**). RT-qPCR analysis
385 also found 50% lower *Adipoq* mRNA in both inguinal and epididymal WAT in chow fed
386 *Mfn2^{R707W}* mice and in inguinal WAT from HFD fed *Mfn2^{R707W}* mice (**Figure 5E**).

387 To assess leptin secretion directly, we studied production of adipokines from adipose
388 explants. Explants from KI mice fed on HFD for 4 weeks showed lower secretion of leptin
389 and adiponectin per gram of tissue (**Figure 5-figure supplement 1A-B**). KI explants also
390 exhibited minimal increase in leptin secretion after insulin and dexamethasone stimulation.

391 *Adipoq* mRNA was lower in KI than WT explants at baseline whereas *Lep* mRNA was no
392 different at baseline but failed to increase in KI explants following insulin and
393 dexamethasone stimulation (**Figure 5-figure supplement 1C**).

394 To assess whether induction of the ISR in adipose tissue may be responsible for the relative
395 leptin deficiency in both humans and mice homozygous for MFN2 R707W, we studied
396 adipocytes freshly isolated from mouse gonadal fat in floating culture, adapting a recently
397 described protocol⁶⁴. We induced the ISR using each of two different well characterised
398 activators, namely thapsigargin (TG), an inhibitor of the endoplasmic reticulum (ER) Ca²⁺
399 ATPase that depletes ER calcium^{65,66}, or tunicamycin (TN), which blocks protein
400 glycosylation. ISR induction was confirmed by increased *Atf4* and *Ddit3* mRNA and/or
401 protein expression, and by eIF2 α phosphorylation (**Figure 5F-L**). *Lep* mRNA was modestly
402 reduced by TG but not by TN (**Figure 5H**), whereas both agents reduced intracellular leptin
403 protein expression (**Figure 5L**) and secretion (**Figure 5J**). Expression of adiponectin was
404 also reduced without a change in mRNA level whereas expression of Akt and the insulin
405 receptor beta subunit were not altered (**Figure 5I, K & L**). These data suggest that ISR
406 activation may have a bigger impact on secreted proteins than on intracellular proteins, in
407 keeping with the previous suggestion that the ISR tends to prevent a fall in intracellular
408 amino acid concentrations⁶⁶. In seeking to validate this notion, we proceeded to measure the
409 serum concentration of adipisin, another 'adipokine' selectively secreted by adipocytes.
410 Serum adipisin concentrations were significantly lower in the KI mice than in WT controls in
411 both chow and HFD fed mice (**Figure 5M**), suggesting that low serum leptin and adiponectin
412 may be part of a wider pattern of reduced adipocyte-derived secreted proteins in *MFN2*^{R707W}
413 KI mice.

414

415

416 **Discussion**

417 The recent discovery that humans homozygous for the MFN2 R707W mutation manifest
418 striking adipose redistribution associated with serious metabolic disease is probably the
419 clearest example to date of a causal link in humans between a mitochondrial perturbation
420 and adipose dysregulation. MFN2-related lipodystrophy has some remarkable and currently
421 poorly understood features. These include: a) a marked and often dramatic increase in
422 upper body adiposity, contrasting with loss of lower limb adipose tissue; b) a severe
423 reduction in plasma leptin concentration despite abundant, histologically near-normal upper
424 body fat. These problems have to date been associated only with the R707W mutation. To
425 investigate the molecular pathogenesis of MFN2 R707W-related lipodystrophy, and the role
426 of MFN2 in leptin synthesis and secretion, we generated and characterised homozygous
427 *Mfn2*^{R707W/R707W} mice.

428 *Mfn2* knock-out mice die in early embryogenesis³¹ while mice homozygous for either of two
429 human neuropathy-associated, GTPase null missense mutations (H361Y or R94W) die on
430 day 0-1³³. *Mfn2* is nearly ubiquitously co-expressed with its closely related paralogue *Mfn1*,
431 and this demonstrates that it has essential, non-redundant functions. Homozygous *Mfn2*
432 R707W mice, in contrast, were viable and bred normally, showing that *Mfn2* R707W retains
433 significant function. *Mfn2* also has key metabolic functions in mature adipocytes: mice
434 lacking *Mfn2* in all adipocytes³⁶ or in brown adipocytes alone³⁷ did not show reduced adipose
435 tissue, but they did exhibit lower energy expenditure, reduced expression of multiple
436 oxidative phosphorylation subunits, and impaired cold tolerance. Paradoxically, however,
437 both lines were protected from systemic insulin resistance. Mice in which *Mfn2* was deleted
438 in all adipocytes in adulthood showed increased obesity and elevated blood glucose³⁸. In
439 contrast, homozygous *Mfn2* R707W mice showed no overt change in adipose mass,
440 metabolic function, or thermogenic capacity even though the genetic alteration was
441 constitutional. This confirms some retained *Mfn2* function also in adipose lineages.

442 Primary anatomical and/or functional defects in humans with MFN2 R707W homozygosity
443 have been observed only in adipose tissue and peripheral nerves, with some but not all
444 people reported to have sensorimotor neuropathy. Such neuropathy is commonly observed
445 in people with heterozygous loss of MFN2 function^{15,67}. Although homozygous *Mfn2* R707W
446 KI mice had no overt anatomical adipose abnormality, and failed to show obvious
447 neurological phenotypes, ultrastructural studies did reveal mitochondrial network disruption
448 in adipose tissues, but not liver, skeletal muscle, or heart. The structural changes in mouse
449 adipose mitochondria resembled those in adipose tissue from patients homozygous for the
450 MFN2 R707W mutation⁸, and in both species these were associated with robust activation of
451 the ISR, which was also seen previously in tissue-specific *Mfn2* knock-out mice⁶⁸. The ISR

452 was not activated in liver, muscle, and heart, strengthening evidence that Mfn2 R707W has
453 deleterious effects selectively in adipose tissue. We cannot conclusively exclude the
454 possibility that tissues other than brown and white adipose tissue are affected, as we have
455 not studied every tissue in the mice or patients, but if present, it is not associated with overt
456 phenotypes.

457 The reason for adipose-selectivity of abnormalities in Mfn2 R707W homozygous mice is not
458 established, but disruption of the function of Mfn2 in establishment or maintenance of
459 mitochondrial-lipid droplet contact sites, perhaps through interaction with an adipose-specific
460 protein, is plausible. We did observe reduced mitochondrial-lipid droplet contacts in brown
461 adipose tissue from Mfn2 R707W KI mice, as reported in adipocyte *Mfn2* knock-out animals,
462 but we were unable to replicate the direct mitofusin 2-perilipin 1 interaction previously
463 reported using co-immunoprecipitation³⁶. This requires further characterisation in the context
464 of Mfn2^{R707W}.

465 Whether mitochondrial structural and functional perturbation mediates the overgrowth of
466 some adipose depots and loss of others in humans with MFN2 R707W homozygosity
467 remains to be proven. If it does, the mechanisms transducing dysfunction of a key organelle
468 into cellular hyperplasia in some adipose depots but loss of adipose tissue in others are also
469 unexplained. KI mice exhibit neither adipose loss nor hyperplasia, even when challenged by
470 a HFD. This failure to model the gross anatomical adipose abnormalities of humans, despite
471 evidence of mitochondrial dysfunction and attendant ISR, establishes that the cellular
472 abnormalities we describe are not sufficient to perturb adipose growth, but they may still be
473 necessary. Whether a permissive genetic background, or an undefined additional stressor,
474 are required as cofactors, remains to be determined.

475 Some of the transcriptomic changes observed that are common to mouse and human
476 adipose tissue do suggest both potential opportunities to intervene pharmacologically, and
477 mechanistic hypotheses relating to adipose hyperplasia that warrant further investigation.
478 For example, transcriptional evidence of strong mTORC1 activation, likely part of the
479 proximal ISR triggered by mitochondrial dysfunction, suggests that mTOR inhibitors such as
480 sirolimus are worthy of testing. It is possible that they may reduce the ISR, thereby
481 restraining compensatory adipose hyperplasia or even inducing synthetic lethality in cases of
482 MFN2 R707W homozygosity. Several previous studies have suggested that mTOR inhibition
483 may have beneficial effects in other primary mitochondrial disorders^{59,69}. Downregulation of
484 TGF β also merits further investigation as one candidate mechanism linking Mfn2 R707W
485 homozygosity to adipose hyperplasia. This is based on strong transcriptional evidence of
486 downregulated EMT in both mice and humans, on the important roles of TGF β in EMT and

487 adipogenesis^{70,71}, and on the inter-relationship of TGF β signalling with mitochondrial
488 dysfunction⁷²⁻⁷⁵.

489 A further notable difference between the mice and humans with the homozygous MFN2
490 R707W mutation is that serum concentrations of GDF15 and FGF21 were increased in
491 people but not mice (**Table 2**). This likely reflects the fact that affected humans also have
492 fatty liver disease and diabetes, both strongly associated with elevated stress hormone
493 levels^{76,77}. In keeping with this, we have shown in mice that the liver is the predominant
494 source of circulating FGF21 and GDF15, with little or no contribution from adipose tissue⁷⁸.

495 Although abnormal adipose growth and metabolic disease were not seen in KI mice, the low
496 plasma leptin concentration seen in human adipose overgrowth associated with MFN2
497 mutations was replicated. Leptin concentrations were not reported in previously described
498 adipocyte *Mfn2* knock-out mice^{36,38}, and although a different model of adipose-specific
499 mitochondrial dysfunction (*Tfam* knock-out) did show reduced serum leptin, fat mass was
500 also reduced compared to WT⁷⁹. Lower adipose leptin secretion caused by *Mfn2* R707W
501 does not appear to be predominantly transcriptionally mediated in mice, as in some
502 analyses, for example of adipose explants under basal conditions, leptin secretion was
503 reduced (**Figure 5-figure supplement 1A**) without alteration of leptin mRNA (**Figure 5-
504 figure supplement 1C**). Our findings suggest instead that the lower leptin secretion is a
505 consequence of ISR activation. Synthesis of adipokines is an amino acid-intensive process,
506 and activation of the UPR typically results in conservation of amino acids, in part through
507 reduction of protein secretion^{66,80-82}. Stressing primary adipocytes with tunicamycin or
508 thapsigargin reduced leptin secretion without any effect on expression of non-secreted
509 proteins such as the insulin receptor. We also observed upregulation of pathways related to
510 amino acid metabolism (particularly in BAT) (**Figure 4 – Figure Supplement 4**), which
511 would be consistent with the known transcriptional effects of Atf4⁸³. This suggests that the
512 low leptin may not be due to a mitofusin-specific mechanism, rather secondary to activation
513 of the ISR in adipose tissue as part of amino acid conservation. KI mouse data suggest that
514 other adipokines, including adiponectin and adipisin, are similarly affected.

515 This study has limitations. We characterised male homozygous KI mice only in detail, so
516 cannot extrapolate our results to females with confidence, though case series do not
517 suggest significant sexual dimorphism in the human disorder⁸⁻¹⁰. We also did not study
518 heterozygous animals, but as human MFN2 R707W-associated lipodystrophy shows
519 recessive inheritance, and as even homozygous mice do not exhibit lipodystrophy, a
520 phenotype in heterozygous animals seems unlikely. It is unclear to what extent the
521 phenotype observed in BAT is due to reduction in expression of both the mitofusins. Given
522 the concomitant reduction in expression of Oxphos components in BAT, the lower mitofusin

523 expression may be more reflective of general mitochondrial perturbation. Lastly, this study
 524 has not directly assessed the ability of Mfn2^{R707W} mutants to mediate mitochondrial fusion.
 525 However given the normal mitochondrial network morphology in non-adipose tissues in
 526 homozygous KI mice and in dermal fibroblasts from humans homozygous for MFN2
 527 R707W⁸, any defect is likely mild and context dependent.

528 **Conclusion**

529 Mfn2^{R707W} KI mice show adipose-selective alteration of mitochondrial morphology and robust
 530 activation of the integrated stress response, but no abnormal adipose growth or systemic
 531 metabolic derangement. The KI mice do show suppressed leptin expression and plasma
 532 leptin concentration, likely secondary to the adipose selective mitochondrial stress response.
 533 The unique association of human lipodystrophy with the MFN2 R707W allele remains
 534 unexplained, but transcriptomic analysis suggested that reduced TGFβ signalling warrants
 535 further explanation as a potential cause of adipose hyperplasia, while mTOR inhibitors are
 536 worthy of testing in models as a potential targeted therapy.

537 **Methods**

538

539

Key Resources Table				
Reagent type (species) or resource	Designation	Source or reference	Identifiers	Additional information
strain, strain background (<i>Mus musculus</i> , C57BL/6J)	Mfn2 ^{R707W}	This paper		See "Generation of the Mfn2 ^{R707W/R707W} knock-in mouse"
antibody	Mouse monoclonal anti-Adiponectin	GeneTex	Cat# GTX80683	WB (1:1000)
antibody	Rabbit polyclonal anti-Leptin	Abcam	Cat# ab9749	WB (1:1000)

antibody	Mouse monoclonal anti-Mfn1	Abcam	Cat# Ab126575	WB (1:250)
antibody	Rabbit monoclonal anti-Mfn2	Cell signalling	Cat# D2D10	WB (1:1000)
antibody	Rabbit polyclonal anti-Mthfd2	Proteintech	Cat# 12270-1-AP	WB (1:1000)
antibody	Rabbit polyclonal anti-Oma1	Proteintech	Cat# 17116-1-AP	WB (1:1000)
antibody	Mouse monoclonal anti-Opa1	BD Biosciences	Cat# 612606	WB (1:1000)
antibody	Mouse monoclonal OXPHOS cocktail	Abcam	Cat# Ab110413	WB (1:1000)
antibody	Rabbit monoclonal anti-Phos-Eif2a	Epitomics	Cat# 10901	WB (1:1000)

540 A full list of antibodies and primers are available in Supplementary Tables 1 and 2.

541

542 Generation of the *Mfn2*^{R707W/R707W} knock-in mouse

543 *Mfn2*^{R707W} mice were generated using CRISPR-Cas9 microinjection of fertilised oocytes at
544 The Wellcome Trust Centre for Human Genetics (Oxford, UK). Two single guide RNA
545 (sgRNA) sequences targeting exon 18 of the mouse *Mfn2* gene (ENSMUSE00000184630)
546 were used, namely 5'- CACCGTTCCTGCTCCAGATTATCTC-3' and 5'-
547 AAACGAGATAATCTGGAGCAGGAAC-3'. The single-strand donor oligonucleotide (ssODN)
548 incorporated the desired R707W mutation by recoding codon 707 from CGA to TGG. (This
549 involved two point mutations in order to avoid a stop codon.) A silent mutation was added
550 upstream to generate an EcoRV restriction site (Figure 1).

551 Superovulated 3-week old C57BL/6J female mice were mated with C57BL/6J males.
552 Embryos were extracted on day 0.5 of pregnancy and cultivated until two pronuclei were
553 visible. One pronucleus was injected with purified sgRNA (20ng/μL), Cas9 protein (100
554 ng/μL), and the ssODN template (10ng/μL). Embryos were reimplanted into pseudopregnant
555 CD1 foster mothers at day 0.5 post-coitum. *Mfn2*^{R707W} was confirmed by Sanger sequencing
556 of F0 founder males (with one additional upstream silent mutation ACC>ACA). Following
557 cryopreservation of embryos, the line was re-derived in a colony of C57BL/6J mice in
558 Cambridge, UK.

559 Genotyping utilised the upstream EcoRV restriction enzyme digestion site. For genotyping,
560 ear biopsies were digested in Chelix and proteinase K (0.1mg/mL) for 45 min at 50°C to
561 extract gDNA for use in PCR. gDNA was amplified using primers 5'-
562 AGTCCCTTCCTTGCTCACTTAGT-3' and 5'-ATCTCACAAGAAAGCGAAATCC-3' and GoTaq
563 DNA Polymerase (Promega), then digested using EcoRV (New England Biosciences). Wild-
564 type (WT) *Mfn2* generates a PCR product of 523bp, homozygous knock-ins (KI) have two
565 bands at 327bp and 196bp, and heterozygotes have all three bands (Figure 1).

566 Mouse husbandry and phenotyping

567 All experiments were performed under UK Home Office-approved Project License 70/8955
568 except for thermogenic capacity assessments which were conducted under P0101ED1D.
569 Protocols were approved by the University of Cambridge Animal Welfare and Ethical Review
570 Board. Animals were co-housed in groups of 2-5 littermates of mixed genotype, on 12 hr
571 light/dark cycles. They had access to food and water *ad libitum* except when fasting prior to
572 experimental procedures.

573 Separate cohorts of male and female mice were studied. Unless otherwise stated (**Figure 3**
574 **– Figure Supplement 2**), data represents results from male mice. WT and KI male mice
575 aged 5 weeks were randomly allocated to HFD (45% kcal as fat, 4.7kcal/g, Research Diets
576 D12451i) or chow (Safe Diets R105-25) for up to 6 months. Investigators were blinded to
577 animal genotype at the point of data collection. Mice were weighed weekly. Tail blood
578 samples were collected four weekly into heparinised capillary tubes (Hawksley) and spun at
579 13,000g for 4 min for plasma analysis of leptin and adiponectin. 6 hr fasted blood samples
580 were obtained on weeks 16 and 24 of diet, and prior to sacrifice, for analysis of glucose,
581 insulin, and lactate, whilst other blood samples were from fed animals. For lactate, tail vein
582 blood was collected into fluoride oxalate tubes and centrifuged immediately before freezing
583 of plasma at -80°C.

584 An intraperitoneal glucose tolerance test (IPGTT) was performed on week 31 of chow and
585 HFD and an intraperitoneal insulin tolerance test (IPITT) was performed on week 32 of HFD
586 (only) after a 6 hr fast. 1g/kg of glucose and 0.75 units/kg of insulin were administered for

587 the IPGTT and IPITT, respectively. Blood glucose was measured at 0, 10, 20, 30, 60, 90,
588 and 120 min after the injections using a glucometer (Abbot Laboratories) and glucose test
589 strips (Abbot Laboratories). Insulin was measured at 0 min at the start of IPGTT from a tail
590 vein blood sample.

591

592 Body composition (lean and fat mass) was assessed prior to sacrifice by Time-Domain
593 Nuclear Magnetic Resonance (TD-NMR) using a Minispec Live Mouse Analyzer (Bruker).
594 Mice were sacrificed at 4- or 33- weeks on diet after a 6 hr fast. Tissues were weighed,
595 sections were removed for histological or electron microscopic analysis, and remaining
596 tissue was snap frozen in liquid nitrogen.

597

598 To estimate the number of mice required for experimental groups, We used data from the
599 *Adipoq::Cre Mfn2* knock-out mouse³⁶, aiming to determine a difference between fat mass in
600 *Mfn2*^{R707W} and wild-type. Mean fat mass in adipose-specific *Mfn2* knock-out = 3.8±0.43g.
601 Mean fat mass in wild-type = 2.9±0.14g. For 80% power at 0.05 significance, to detect 0.9g
602 difference, sample size: 8 animals per group.

603

604 Calorimetry studies

605 Eight-week-old chow-fed male mice were housed in either cold (10°C) or thermoneutrality
606 (30°C) for 4 weeks. Animals were anaesthetised using 90mg/kg of pentobarbital by
607 intraperitoneal injection and were placed in 2.7 l calorimetry chambers (Oxymax, Columbus
608 instruments, Ohio) attached to a Promethion calorimetry system (Sable Systems, Las
609 Vegas, NV, USA) pre-warmed to 30°C for 20 min for measurement of basal energy
610 expenditure. They were then given a subcutaneous injection of 2 µl/g of 0.5 mg/mL
611 noradrenaline bitartrate (NA) plus 1.66 µl/g of 18 µg/µl pentobarbital and NA-stimulated
612 energy expenditure was measured for 25 min. Animals were then sacrificed, and tissues
613 snap frozen as described above. Basal energy expenditure was calculated from the three
614 readings prior to NA-injection. Peak energy expenditure was calculated from the three
615 greatest readings 5-25 min after NA-injection. NA-induced energy expenditure was
616 calculated as the difference between peak and basal energy expenditure.

617 Transmission Electron Microscopy (TEM)

618 Chow-fed mice aged 8 weeks were sacrificed and white adipose tissue (inguinal and
619 epididymal), brown adipose tissue, skeletal muscle (quadriceps), heart, and liver were
620 removed, cut into <1 mm³ cubes and fixed (2% glutaraldehyde/2% formaldehyde in 0.05 M
621 sodium cacodylate buffer pH 7.4 containing 2 mM calcium chloride) on a rocker at 4°C
622 overnight. Samples were then washed five times with 0.05 M sodium cacodylate buffer pH

623 7.4 and osmicated (1% osmium tetroxide, 1.5 % potassium ferricyanide, 0.05 M sodium
624 cacodylate buffer pH 7.4) for 3 days at 4°C.

625 Following initial osmication, samples were washed five times in DIW (deionised water) then
626 treated with 0.1 % (w/v) thiocarbohydrazide/DIW for 20 min at room temperature in the dark.
627 After washing five times in DIW, samples were osmicated a second time for 1 hr at room
628 temperature (2% osmium tetroxide/DIW). After washing five times in DIW, samples were
629 block stained with uranyl acetate (2% uranyl acetate in 0.05 M maleate buffer pH 5.5) for 3
630 days at 4°C. Samples were washed five times in DIW and then dehydrated in a graded
631 series of ethanol (50%/70%/95%/100%/100% dry) 100% dry acetone and 100% dry
632 acetonitrile, three times in each for at least 5min. Samples were infiltrated with a 50/50
633 mixture of 100% dry acetonitrile/Quetol resin (without benzyldimethylamine (BDMA))
634 overnight, followed by 3 days in 100% Quetol (without BDMA). Then, samples were
635 infiltrated for 5 days in 100% Quetol resin with BDMA, exchanging the resin each day. The
636 Quetol resin mixture is: 12 g Quetol 651, 15.7 g NSA, 5.7 g MNA and 0.5 g BDMA (all from
637 TAAB). Samples were placed in embedding moulds and cured at 60°C for 3 days.

638 Thin sections were cut using an ultramicrotome (Leica Ultracut E) and placed on bare 300
639 mesh copper TEM grids. Samples were imaged in a Tecnai G2 TEM (FEI/Thermo Fisher
640 Scientific) run at 200 keV using a 20 µm objective aperture to improve contrast. Images were
641 acquired using an ORCA HR high resolution CCD camera (Advanced Microscopy
642 Techniques Corp, Danvers USA).

643 Analysis was performed by manual measurement of individual mitochondrion from all
644 obtained images using Fiji⁸⁴/ImageJ measurement tools by an investigator who was blinded
645 to the genotype of tissues/cells. In all tissues, mitochondrial perimeter and aspect ratio
646 (length/width) were determined. In addition, in brown adipose tissue, the number of cristae
647 per mitochondrion and mitochondrial-lipid droplet contacts were quantified. There were
648 insufficient mitochondrial-lipid droplet contact sites with high quality preservation to permit
649 this in white adipose tissue. In liver, mitochondrial-endoplasmic reticulum contact sites were
650 quantified. It was not possible to assess for mitochondria-ER contacts in other tissues due to
651 quality of preservation.

652 Isolation of mitochondria for Oroboros analysis

653 For *ex vivo* measurement of mitochondrial respiratory capacity, mitochondria were isolated
654 from BAT and liver of 12 week old chow-fed male mice using the protocols from McLaughlin
655 *et al.*⁸⁵ for BAT and Fernández-Vizarra *et al.*⁸⁶ for liver. In brief, tissues were isolated and
656 washed in buffer 'B' then homogenised using a drill-driven Teflon pestle and borosilicate
657 glass vessel. Homogenates were centrifuged at 800 x *g* for 10 min at 4°C to remove cellular
658 debris. Supernatant was removed, and then re-centrifuged at 10,000 x *g* for 10 min at 4°C

659 to enrich mitochondria. Supernatant was discarded and mitochondria were resuspended in
660 buffer 'A'. Mitochondria were quantified using a BioRad Protein Assay.

661 Fifty μg of protein were used per chamber for high-resolution respirometry, using Oroboros
662 (Innsbruck, Austria). There was sequential injection of: 20 μl of 1 M glutamate and 10 μl of 1
663 M malate (liver only), 20 μl of 0.5 M ADP, 20 μl of 1 M pyruvate, 20 μl of 2 M succinate, 1 μl
664 of 1 mM CCCP (liver only), 2 μl of 2 mM rotenone, and 2 μl of 2 mM antimycin A.

665 mtDNA content assay

666 Relative mtDNA content was assayed using real-time quantitative polymerase chain reaction
667 (RT-qPCR) quantification of mitochondrial *Rnr2* and nuclear *Hk2* DNA. DNA was extracted
668 from snap frozen murine tissue, using a DNeasy kit (Qiagen) as per the manufacturer's
669 instructions. DNA was quantified on Nanodrop and diluted to 4 ng/ μl . RT-qPCR was
670 performed in triplicate for each sample using 8 ng DNA with primers for *Hk2* and *Rnr2*.
671 mtRnr2/nHk2 was calculated using the standard curve method and expressed relative to
672 WT.

673 Protein extraction for WB

674 Fifty mg of frozen tissue was crushed using a pestle and mortar in liquid nitrogen. Powdered
675 tissue was dissolved in 800 μl of RIPA buffer (Sigma, R0278) containing protease (Sigma,
676 11836170001) and phosphatase inhibitors (Roche, 04906837001). Samples were sonicated
677 twice for 5 s at 30 Hz before centrifugation at 10,000 \times g for 5 min at 4°C. Supernatant was
678 extracted and, for adipose samples, re-centrifuged to remove excess lipid.

679 Thirty-45 μg of protein lysates were mixed with NuPAGE 4x LDS buffer (ThermoFisher
680 Scientific), containing 0.05% 2-mercaptoethanol, and denatured for 5 min at 95°C. Samples
681 were run on 4-12% Bis-Tris gels (Invitrogen) and transferred onto a nitrocellulose membrane
682 using iBlot-2 (ThermoFisher Scientific). For Opa1 immunoblotting, protein lysates were
683 prepared using 4x BOLT™ LDS sample buffer and resolved using BOLT™ 8% Bis-Tris with
684 BOLT™ MOPS SDS running buffer (ThermoFisher Scientific). Membranes were washed in
685 Tris-buffered saline with 0.1% (vol/vol) Tween 20 (TBST, Sigma) before blocking in 5%
686 (wt/vol) skimmed milk powder dissolved in TBST. Membranes were incubated with primary
687 antibodies (**Supplementary Table 1**) at 4°C for 16 hr, washed with TBST five times for 5
688 min, followed by incubation with horseradish peroxidase (HRP)-conjugated secondary
689 antibodies for 1 hr at room temperature. Blots were developed using Immobilon Western
690 Chemiluminescent HRP Substrate (Millipore) with images acquired on BioRad ChemiDoc
691 Imaging system or ImageQuant LAS 4000 (GE Healthcare).

692 For Opa1 quantification, Opa1-cleaved S-Opa1 bands were calculated as described by
693 Shammas *et al.*⁸⁷, with the intensity of each of the five Opa1 bands on the blot measured.,

694 The intensity of c and e bands were summed and divided by the sum of the five bands (a–e)
695 to obtain the percentage of S-Opa1 generated by Oma1 from total Opa1.

696

697 RNA isolation and qPCR analysis

698 At the end of the study, tissues were harvested and immediately snap frozen in liquid
699 nitrogen and stored at -80°C. For RNA isolation, 30-50 mg of tissue was placed in Lysing
700 Matrix D tubes and homogenized in 800 µl TRI Reagent (T9424, Sigma) using the Fastprep-
701 24 Homogenizer for 30 s at 4-6 m/s (MP Biomedical). Homogenate was transferred to an
702 RNase free tube and 200 µl chloroform (Sigma) added. The samples were vortexed and
703 centrifuged at 13,000 rpm for 15 min at 4°C. The upper phase was then transferred to an
704 RNase free tube and mixed with an equal volume of 70% ethanol before loading onto RNA
705 isolation spin columns. RNA was extracted using a RNeasy Mini Kit (74106, Qiagen)
706 isolation kit following the manufacturer's instructions.

707 Total RNA of 600 ng was quantified using Nanodrop and converted to cDNA using MMLV
708 Reverse Transcriptase with random primers and RNase inhibitor (Promega). RT-qPCR was
709 performed using SYBR Green or TaqMan Universal PCR MasterMixes (Applied Biosystems)
710 on QuantStudio 7 Flex Real time PCR system (Applied Biosystems). Primers are listed in
711 **Supplementary Table 2**. Reactions were performed in triplicate and RNA expression was
712 normalised to *36b4*, *Hprt*, and *B2m* expression using the standard curve method.

713 Immunoassays

714 Mouse sera and plasma were analysed by the Cambridge Biochemical Assay Laboratory,
715 University of Cambridge. Leptin was measured using a 2-plex Mouse Metabolic
716 immunoassay kit from Meso Scale Discovery Kit (Rockville, MD, USA) according to the
717 manufacturers' instructions and with supplied calibrants. GDF15 was measured using a
718 modified Mouse GDF15 DuoSet ELISA (R&D Systems) as an electrochemiluminescence
719 assay on the Meso Scale Discovery platform. Adiponectin (K152BYC-2, MSD) was analysed
720 individually using the Meso Scale Discovery Kit (Rockville, MD, USA). NEFA were analysed
721 using the Free Fatty Acid Kit (half-micro test) (11383175001, Roche) and TG was measured
722 using an enzymatic assay (DF69A, Siemens Healthcare). Alanine aminotransferase (ALT,
723 product code DF143), aspartate aminotransferase (AST, product code DF41A), and total
724 cholesterol (product code DF27) were measured using automated enzymatic assays on the
725 Siemens Dimension EXL analyzer. Mouse Fgf21 was measured using an enzyme-linked
726 immunosorbent assay kit (R&D/ Biochne, cat no. MF2100).

727 Histological processing

728 Fresh tissue was fixed in 10% formalin for 24 hr at room temperature immediately following
729 sacrifice. Tissue was then embedded in paraffin and 4 μ m sections were cut then baked
730 overnight at 50°C. For haematoxylin & eosin (H&E) staining, slides were dewaxed in xylene
731 for 5 min twice, then dehydrated in 100% ethanol for 2 min twice. Following a 3 min water
732 wash, slides were stained with filtered Mayer's haematoxylin (Pioneer Research Chemicals)
733 for 7 min and blued in water for 4 min. Slides were then stained with 1% aqueous eosin
734 (Pioneer Research Chemicals) for 4 min and briefly washed in water before dehydrating in
735 100% ethanol (1 min, twice) and cleared in xylene (2 min, twice) and mounting with Pertex.
736 Slides were imaged using a Axio Scan Z1 slide scanner (Zeiss). Lipid droplet area and
737 hepatic steatosis was quantified automatically using Halo software (Indica Labs).

738 Transcriptomic profiling in white and brown adipose tissue

739 RNA was isolated from three tissues/dietary conditions for RNA sequencing: (1) inguinal
740 WAT from chow fed animals (n=7 WT, n=6 KI, single technical replicates); (2) inguinal WAT
741 from HFD-fed animals (n=8 WT, n=8 KI, two technical replicates per animal); and (3) BAT
742 from HFD-fed animals (n=6 WT, n=6 KI, single technical replicate). RNA was quantified
743 using Agilent 2100 Bioanalyzer (Agilent Technologies Inc) and only samples with RNA
744 Integrity Number ≥ 8 were used for library preparation. cDNA libraries were made using
745 Illumina TruSeq RNA sample kits and sequencing was performed on Illumina NovaSeq 6000
746 with paired-end 150 bp reads (Novogene, Cambridge, UK). Raw reads all passed quality
747 control for Q_{score} , error rate distribution, and AT/GC distribution.

748 Adapter sequences were removed from raw FASTQ files using cutadapt⁸⁸ and aligned to
749 *Mus musculus* reference genome (GRCm38) using STAR⁸⁹. Binary alignment/map (BAM)
750 files were sorted using samtools⁹⁰ and counts were performed using featureCounts⁹¹.
751 Differential gene expression (DGE) between WT and KI was performed using DESeq2⁹²,
752 where significance was considered as a Benjamini-Hochberg false-discovery rate (FDR)
753 corrected p-value $< .01$. Pathway analysis was performed with the EnrichR package for R⁹³⁻⁹⁵
754 using significantly differentially expressed genes to determine enriched Hallmark⁹⁶ and
755 Kyoto Encyclopaedia of Genes and Genomes (KEGG)⁹⁷ gene sets. Gene sets with FDR-
756 corrected p-value $< .05$ were considered enriched. Figures were generated in R 4.0.2⁹⁸ using
757 packages pheatmap, ggplot2, and dplyr.

758 Adipose explant experiments

759 Inguinal (subcutaneous) and epididymal (visceral) adipose tissue was harvested from 12-
760 week-old male C57BL/6J mice fed either chow or HFD for 4 weeks (i.e. 8-12 weeks of age).
761 Tissue was placed in Hanks' Balanced Salt Solution (HBSS, H9269, Sigma) and kept on ice

762 before cutting into 1-2 mm fragments. Approximately 100 mg fragments were incubated in a
763 12-well plate with M199 media \pm 7 nM insulin (Actrapid, Novo Nordisk) and 25 nM
764 dexamethasone (D4902, Sigma). After 24 hr incubation, media were collected, spun down at
765 5,000 x g and stored at -80°C until leptin and adiponectin assay as above. Explant tissues
766 were weighed and snap frozen for RNA analysis.

767 Primary adipocyte experiments

768 Mature white adipocytes were isolated from 12-20-week-old chow-fed male or female
769 C57BL/6J or C57BL/6N mice as previously described^{64,99} with modifications. Briefly, after
770 dissection, gonadal adipose tissue was washed, minced finely, and dissociated to a single-
771 cell suspension in Hanks' Balanced Salt Solution containing 2.25% (w/v) BSA (Sigma, Cat.
772 H9269) and 1 mg/mL collagenase (Sigma, C6885-1G) for approximately 15 min at 37°C in a
773 shaking incubator. Digested material was diluted with 6x volume of high glucose DMEM
774 media (Sigma, Cat. D6546) and connective tissue or undigested pieces were removed by
775 passing through a 100 μ m nylon mesh (Fisherbrand, 11517532). Floating adipocytes were
776 washed twice with 6x volume of high glucose DMEM media before being used for
777 downstream experiments.

778 Mature adipocytes with a packed volume of 60 μ L were then cultured in 500 μ L of high
779 glucose DMEM media (supplemented with 10% FBS (Gibco Cat. 10270-106), 2 mM L-
780 glutamine (Sigma Cat. G7513) and 1 x Penn/Strep (Sigma Cat. P0781)) per well in the
781 presence of 100 nM insulin in a 24-well plate. On the third day of in vitro culture, 100 μ L of
782 media was sampled followed by media replenishment. Cells were treated with indicated
783 concentration of Thapsigargin or Tunicamycin for 6 hr. Media were sampled at the end of
784 treatment and cells collected for subsequent RT-qPCR or western blotting. Adipokine
785 secretion from adipocytes during the 6 hr window was calculated as $X=B-A*400/500$ (A/B =
786 medium adipokine concentration before/after treatment).

787 Statistical analysis

788 Continuous data were expressed as mean \pm standard error (SE). Normally distributed data
789 were analysed by t-test (for two group pairwise comparison) and one-way ANOVA (for three
790 or more groups) with post-hoc Bonferroni multiple comparisons test. FDR-corrected p-value
791 $<.05$ was considered significant.

792 Statistical tests of TEM data (pairwise comparisons of mutant to WT) were based on the
793 mean of independent biological replicates (i.e. the number of different samples, not the
794 number of mitochondria) and FDR adjustment for the number of tests¹⁰⁰.

795

796 All experiments were conducted at least three times using, where possible, randomisation of
797 sample order and blinding of experimenters handling samples. No data were excluded from

798 analysis. Data were analysed using R 4.0.2⁹⁸ and GraphPad Prism version 9 (GraphPad,
799 San Diego). Figures were made using BioRender.

800

801 Materials availability

802 All reagents used are publicly available. Primer sequences and antibodies are detailed in
803 Supplementary Tables 1 and 2. Code used in analysis is available from:
804 <https://doi.org/10.5281/zenodo.5770057>. Raw counts from transcriptomic analysis are
805 available from GEO under accession ID: GSE210771.

806

807

808 **References**

- 809 1. Gorman, G. S. *et al.* Mitochondrial diseases. *Nature Reviews Disease Primers* **2**, 16080
810 (2016).
- 811 2. Thompson, K. *et al.* Recent advances in understanding the molecular genetic basis of
812 mitochondrial disease. *J. Inherit. Metab. Dis.* **43**, 36–50 (2020).
- 813 3. Craven, L., Alston, C. L., Taylor, R. W. & Turnbull, D. M. Recent Advances in
814 Mitochondrial Disease. *Annu. Rev. Genomics Hum. Genet.* **18**, 257–275 (2017).
- 815 4. Suomalainen, A. & Battersby, B. J. Mitochondrial diseases: the contribution of organelle
816 stress responses to pathology. *Nat. Rev. Mol. Cell Biol.* **19**, 77–92 (2018).
- 817 5. Pacheu-Grau, D., Rucktäschel, R. & Deckers, M. Mitochondrial dysfunction and its role
818 in tissue-specific cellular stress. *Cell Stress Chaperones* **2**, 184–199 (2018).
- 819 6. Alston, C. L., Rocha, M. C., Lax, N. Z., Turnbull, D. M. & Taylor, R. W. The genetics and
820 pathology of mitochondrial disease. *J. Pathol.* **241**, 236–250 (2017).
- 821 7. Schon, E. A. & Manfredi, G. Neuronal degeneration and mitochondrial dysfunction. *J.*
822 *Clin. Invest.* **111**, 303–312 (2003).
- 823 8. Rocha, N. *et al.* Human biallelic MFN2 mutations induce mitochondrial dysfunction,
824 upper body adipose hyperplasia, and suppression of leptin expression. *Elife* **6**, e23813
825 (2017).
- 826 9. Sawyer, S. L. *et al.* Homozygous mutations in MFN2 cause multiple symmetric
827 lipomatosis associated with neuropathy. *Hum. Mol. Genet.* **24**, 5109–5114 (2015).
- 828 10. Capel, E. *et al.* MFN2-associated lipomatosis: Clinical spectrum and impact on adipose
829 tissue. *J. Clin. Lipidol.* (2018) doi:10.1016/j.jacl.2018.07.009.
- 830 11. Carr, A. S. *et al.* MFN2 deletion of exons 7 and 8: Founder mutation in the UK
831 population. *J. Peripher. Nerv. Syst.* **20**, 67–71 (2015).
- 832 12. Masingue, M. *et al.* Homozygous p.R707W MFN2 mutation is associated with
833 neuropathy, lipomatosis, peripheral lipoatrophy and metabolic alterations. *Neuromuscul.*
834 *Disord.* **27**, S148 (2017).
- 835 13. Piscoquito, G. *et al.* Mutational mechanisms in MFN2 -related neuropathy: Compound
836 heterozygosity for recessive and semidominant mutations. *J. Peripher. Nerv. Syst.* **20**,
837 380–386 (2015).
- 838 14. Giacomello, M., Pyakurel, A., Glytsou, C. & Scorrano, L. The cell biology of
839 mitochondrial membrane dynamics. *Nat. Rev. Mol. Cell Biol.* **21**, 204–224 (2020).
- 840 15. Chung, K. W. *et al.* Early onset severe and late-onset mild Charcot-Marie-Tooth disease
841 with mitofusin 2 (MFN2) mutations. *Brain* **129**, 2103–2118 (2006).
- 842 16. Verhoeven, K. *et al.* MFN2 mutation distribution and genotype/phenotype correlation in
843 Charcot-Marie-Tooth type 2. *Brain* **129**, 2093–2102 (2006).
- 844 17. Neusch, C. *et al.* Mitofusin 2 gene mutation (R94Q) causing severe early-onset axonal
845 polyneuropathy (CMT2A). *Eur. J. Neurol.* **14**, 575–577 (2007).
- 846 18. Szkudelski, T. Intracellular mediators in regulation of leptin secretion from adipocytes.
847 *Physiol. Res.* **56**, 503–512 (2007).
- 848 19. Montague, C. T., Prins, J. B., Sanders, L., Digby, J. E. & O’Rahilly, S. Depot- and sex-
849 specific differences in human leptin mRNA expression: implications for the control of
850 regional fat distribution. *Diabetes* **46**, 342–347 (1997).
- 851 20. Cammisotto, P. G. Regulation of leptin secretion from white adipocytes by insulin,
852 glycolytic substrates, and amino acids. *AJP: Endocrinology and Metabolism* **289**, E166–
853 E171 (2005).
- 854 21. Alvarez-Guaita, A. *et al.* Phenotypic characterization of Adig null mice suggests roles for
855 adipogenin in the regulation of fat mass accrual and leptin secretion. *Cell Rep.* **34**,
856 108810 (2021).
- 857 22. Kijima, K. *et al.* Mitochondrial GTPase mitofusin 2 mutation in Charcot-Marie-Tooth
858 neuropathy type 2A. *Hum. Genet.* **116**, 23–27 (2005).
- 859 23. Züchner, S. *et al.* Mutations in the mitochondrial GTPase mitofusin 2 cause Charcot-
860 Marie-Tooth neuropathy type 2A. *Nat. Genet.* **36**, 449–451 (2004).

- 861 24. Feely, S. M. E. *et al.* MFN2 mutations cause severe phenotypes in most patients with
862 CMT2A. *Neurology* **76**, 1690–1696 (2011).
- 863 25. Stuppia, G. *et al.* MFN2-related neuropathies: Clinical features, molecular pathogenesis
864 and therapeutic perspectives. *J. Neurol. Sci.* **356**, 7–18 (2015).
- 865 26. Mattie, S., Riemer, J., Wideman, J. G. & McBride, H. M. A new mitofusin topology
866 places the redox-regulated C terminus in the mitochondrial intermembrane space. *J.*
867 *Cell Biol.* **217**, 507–515 (2018).
- 868 27. Koshiba, T. *et al.* Structural basis of mitochondrial tethering by mitofusin complexes.
869 *Science* **305**, 858–862 (2004).
- 870 28. Franco, A. *et al.* Correcting mitochondrial fusion by manipulating mitofusin
871 conformations. *Nature* **540**, 1–20 (2016).
- 872 29. Davies, V. J. *et al.* Opa1 deficiency in a mouse model of autosomal dominant optic
873 atrophy impairs mitochondrial morphology, optic nerve structure and visual function.
874 *Hum. Mol. Genet.* **16**, 1307–1318 (2007).
- 875 30. Ishihara, N. *et al.* Mitochondrial fission factor Drp1 is essential for embryonic
876 development and synapse formation in mice. *Nat. Cell Biol.* **11**, 958–966 (2009).
- 877 31. Chen, H. *et al.* Mitofusins Mfn1 and Mfn2 coordinately regulate mitochondrial fusion and
878 are essential for embryonic development. *J. Cell Biol.* **160**, 189–200 (2003).
- 879 32. Misko, A., Jiang, S., Wegorzewska, I., Milbrandt, J. & Baloh, R. H. Mitofusin 2 is
880 necessary for transport of axonal mitochondria and interacts with the Miro/Milton
881 complex. *J. Neurosci.* **30**, 4232–4240 (2010).
- 882 33. Strickland, A. V. *et al.* Characterization of the mitofusin 2 R94W mutation in a knock-in
883 mouse model. *J. Peripher. Nerv. Syst.* **19**, 152–164 (2014).
- 884 34. Li, Y.-J. *et al.* Structural insights of human mitofusin-2 into mitochondrial fusion and
885 CMT2A onset. *Nat. Commun.* **10**, 4914 (2019).
- 886 35. Chen, H., McCaffery, J. M. & Chan, D. C. Mitochondrial Fusion Protects against
887 Neurodegeneration in the Cerebellum. *Cell* **130**, 548–562 (2007).
- 888 36. Boutant, M. *et al.* Mfn2 is critical for brown adipose tissue thermogenic function. *EMBO*
889 *J.* **41**, e201694914 (2017).
- 890 37. Mahdavian, K. *et al.* Mfn2 deletion in brown adipose tissue protects from insulin
891 resistance and impairs thermogenesis. *EMBO Rep.* **18**, e201643827 (2017).
- 892 38. Mancini, G. *et al.* Mitofusin 2 in Mature Adipocytes Controls Adiposity and Body Weight.
893 *Cell Rep.* **26**, 2849-2858.e4 (2019).
- 894 39. Silva Ramos, E. *et al.* Mitochondrial fusion is required for regulation of mitochondrial
895 DNA replication. *PLoS Genet.* **15**, e1008085 (2019).
- 896 40. Melber, A. & Haynes, C. M. UPRmt regulation and output: a stress response mediated
897 by mitochondrial-nuclear communication. *Cell Res.* **28**, 281–295 (2018).
- 898 41. D’Amico, D., Sorrentino, V. & Auwerx, J. Cytosolic Proteostasis Networks of the
899 Mitochondrial Stress Response. *Trends Biochem. Sci.* **42**, 712–725 (2017).
- 900 42. Condon, K. J. *et al.* Genome-wide CRISPR screens reveal multitiered mechanisms
901 through which mTORC1 senses mitochondrial dysfunction. *Proc. Natl. Acad. Sci. U. S.*
902 *A.* **118**, (2021).
- 903 43. Lu, P. D., Harding, H. P. & Ron, D. Translation reinitiation at alternative open reading
904 frames regulates gene expression in an integrated stress response. *J. Cell Biol.* **167**,
905 27–33 (2004).
- 906 44. Guo, X. *et al.* Mitochondrial stress is relayed to the cytosol by an OMA1-DELE1-HRI
907 pathway. *Nature* **579**, 427–432 (2020).
- 908 45. Fessler, E. *et al.* A pathway coordinated by DELE1 relays mitochondrial stress to the
909 cytosol. *Nature* **579**, 433–437 (2020).
- 910 46. Ben-Sahra, I., Hoxhaj, G., Ricoult, S. J. H., Asara, J. M. & Manning, B. D. mTORC1
911 induces purine synthesis through control of the mitochondrial tetrahydrofolate cycle.
912 *Science* **351**, 728–733 (2016).
- 913 47. Youle R. J. & van der Bliek, A. M. Mitochondrial fission, fusion, and stress. *Science* **337**,
914 1062–1065 (2012).

- 915 48. Shin, M., Momb, J. & Appling, D. R. Human mitochondrial MTHFD2 is a dual redox
916 cofactor-specific methylenetetrahydrofolate dehydrogenase/methenyltetrahydrofolate
917 cyclohydrolase. *Cancer Metab* **5**, 11 (2017).
- 918 49. Forsström, S. *et al.* Fibroblast Growth Factor 21 Drives Dynamics of Local and Systemic
919 Stress Responses in Mitochondrial Myopathy with mtDNA Deletions. *Cell Metab.* **30**,
920 1040-1054.e7 (2019).
- 921 50. Khan, N. A. *et al.* mTORC1 Regulates Mitochondrial Integrated Stress Response and
922 Mitochondrial Myopathy Progression. *Cell Metab.* **26**, 419-428.e5 (2017).
- 923 51. Fisher, F. M. & Maratos-Flier, E. Understanding the Physiology of FGF21. *Annu. Rev.*
924 *Physiol.* **78**, 223–241 (2016).
- 925 52. Patel, S. *et al.* GDF15 Provides an Endocrine Signal of Nutritional Stress in Mice and
926 Humans. *Cell Metab.* **29**, 707-718.e8 (2019).
- 927 53. Baker, M. J. *et al.* Stress-induced OMA1 activation and autocatalytic turnover regulate
928 OPA1-dependent mitochondrial dynamics. *EMBO J.* **33**, 578–593 (2014).
- 929 54. Anand, R. *et al.* The i-AAA protease YME1L and OMA1 cleave OPA1 to balance
930 mitochondrial fusion and fission. *J. Cell Biol.* **204**, 919–929 (2014).
- 931 55. Harada, T., Iwai, A. & Miyazaki, T. Identification of DELE, a novel DAP3-binding protein
932 which is crucial for death receptor-mediated apoptosis induction. *Apoptosis* **15**, 1247–
933 1255 (2010).
- 934 56. Head, B., Griparic, L., Amiri, M., Gandre-Babbe, S. & van der Blik, A. M. Inducible
935 proteolytic inactivation of OPA1 mediated by the OMA1 protease in mammalian cells. *J.*
936 *Cell Biol.* **187**, 959–966 (2009).
- 937 57. Mann, J. P. & Savage, D. B. What lipodystrophies teach us about the metabolic
938 syndrome. *J. Clin. Invest.* **130**, 4009–4021 (2019).
- 939 58. Lee, D. *et al.* ER Stress Induces Cell Cycle Arrest at the G2/M Phase Through eIF2 α
940 Phosphorylation and GADD45 α . *Int. J. Mol. Sci.* **20**, (2019).
- 941 59. Johnson, S. C. *et al.* mTOR inhibition alleviates mitochondrial disease in a mouse
942 model of Leigh syndrome. *Science* **342**, 1524–1528 (2013).
- 943 60. Zamani, N. & Brown, C. W. Emerging roles for the transforming growth factor- β
944 superfamily in regulating adiposity and energy expenditure. *Endocr. Rev.* **32**, 387–403
945 (2011).
- 946 61. Casalena, G., Daehn, I. & Bottinger, E. Transforming growth factor- β , bioenergetics,
947 and mitochondria in renal disease. *Semin. Nephrol.* **32**, 295–303 (2012).
- 948 62. Wall, C. T. J. *et al.* Mitochondrial respiratory chain dysfunction alters ER sterol sensing
949 and mevalonate pathway activity. *J. Biol. Chem.* **298**, 101652 (2022).
- 950 63. Arita, Y. *et al.* Paradoxical decrease of an adipose-specific protein, adiponectin, in
951 obesity. *Biochem. Biophys. Res. Commun.* **257**, 79–83 (1999).
- 952 64. Li, Q. *et al.* Obesity and hyperinsulinemia drive adipocytes to activate a cell cycle
953 program and senescence. *Nat. Med.* **27**, 1941–1953 (2021).
- 954 65. Wictome, M., Henderson, I., Lee, A. G. & East, J. M. Mechanism of inhibition of the
955 calcium pump of sarcoplasmic reticulum by thapsigargin. *Biochem. J* **283 (Pt 2)**, 525–
956 529 (1992).
- 957 66. Harding, H. P., Zhang, Y., Bertolotti, A., Zeng, H. & Ron, D. Perk is essential for
958 translational regulation and cell survival during the unfolded protein response. *Mol. Cell*
959 **5**, 897–904 (2000).
- 960 67. Pipis, M. *et al.* Natural history of Charcot-Marie-Tooth disease type 2A: a large
961 international multicentre study. *Brain* (2021) doi:10.1093/brain/awaa323.
- 962 68. Sebastian, D. *et al.* Mitofusin 2 (Mfn2) links mitochondrial and endoplasmic reticulum
963 function with insulin signaling and is essential for normal glucose homeostasis.
964 *Proceedings of the National Academy of Sciences* **109**, 5523–5528 (2012).
- 965 69. Civiletto, G. *et al.* Rapamycin rescues mitochondrial myopathy via coordinated
966 activation of autophagy and lysosomal biogenesis. *EMBO Mol. Med.* **10**, (2018).
- 967 70. Ishay-Ronen, D. *et al.* Gain Fat-Lose Metastasis: Converting Invasive Breast Cancer
968 Cells into Adipocytes Inhibits Cancer Metastasis. *Cancer Cell* **35**, 17-32.e6 (2019).

- 969 71. Battula, V. L. *et al.* Epithelial-mesenchymal transition-derived cells exhibit multilineage
970 differentiation potential similar to mesenchymal stem cells. *Stem Cells* **28**, 1435–1445
971 (2010).
- 972 72. Dimeloe, S. *et al.* Tumor-derived TGF- β inhibits mitochondrial respiration to suppress
973 IFN- γ production by human CD4⁺ T cells. *Sci. Signal.* **12**, (2019).
- 974 73. Patel, A. S. *et al.* Epithelial cell mitochondrial dysfunction and PINK1 are induced by
975 transforming growth factor-beta1 in pulmonary fibrosis. *PLoS One* **10**, e0121246 (2015).
- 976 74. Sun, Q. *et al.* TGF- β Upregulated Mitochondria Mass through the SMAD2/3 \rightarrow C/EBP β
977 \rightarrow PRMT1 Signal Pathway in Primary Human Lung Fibroblasts. *J. Immunol.* **202**, 37 – 47
978 (2019).
- 979 75. Yi, E.-Y., Park, S.-Y., Jung, S.-Y., Jang, W.-J. & Kim, Y.-J. Mitochondrial dysfunction
980 induces EMT through the TGF- β /Smad/Snail signaling pathway in Hep3B hepatocellular
981 carcinoma cells. *Int. J. Oncol.* **47**, 1845–1853 (2015).
- 982 76. Vila, G. *et al.* The relationship between insulin resistance and the cardiovascular
983 biomarker growth differentiation factor-15 in obese patients. *Clin. Chem.* **57**, 309–316
984 (2011).
- 985 77. Koo, B. K. *et al.* Growth differentiation factor 15 predicts advanced fibrosis in biopsy-
986 proven non-alcoholic fatty liver disease. *Liver Int.* **38**, 695–705 (2018).
- 987 78. Patel, S. *et al.* Endogenous GDF15 and FGF21 additively alleviate hepatic steatosis
988 and insulin resistance in obese mice. *bioRxiv* 2022.06.08.495255 (2022)
989 doi:10.1101/2022.06.08.495255.
- 990 79. Vernochet, C. *et al.* Adipose-specific deletion of TFAM increases mitochondrial
991 oxidation and protects mice against obesity and insulin resistance. *Cell Metab.* **16**, 765–
992 776 (2012).
- 993 80. Cortopassi, G. *et al.* Mitochondrial disease activates transcripts of the unfolded protein
994 response and cell cycle and inhibits vesicular secretion and oligodendrocyte-specific
995 transcripts. *Mitochondrion* **6**, 161–175 (2006).
- 996 81. Kilberg, M. S., Shan, J. & Su, N. ATF4-dependent transcription mediates signaling of
997 amino acid limitation. *Trends Endocrinol. Metab.* **20**, 436–443 (2009).
- 998 82. Hetz, C., Zhang, K. & Kaufman, R. J. Mechanisms, regulation and functions of the
999 unfolded protein response. *Nat. Rev. Mol. Cell Biol.* **21**, 421–438 (2020).
- 1000 83. Harding, H. P. *et al.* An Integrated Stress Response Regulates Amino Acid Metabolism
1001 and Resistance to Oxidative Stress National Institute of Environmental Health Sciences.
1002 *Mol. Cell* **11**, 619–633 (2003).
- 1003 84. Schindelin, J. *et al.* Fiji: an open-source platform for biological-image analysis. *Nat.*
1004 *Methods* **9**, 676–682 (2012).
- 1005 85. McLaughlin, K. L. *et al.* Novel approach to quantify mitochondrial content and intrinsic
1006 bioenergetic efficiency across organs. *Sci. Rep.* **10**, 17599 (2020).
- 1007 86. Fernández-Vizarra, E. *et al.* Isolation of mitochondria for biogenetical studies: An
1008 update. *Mitochondrion* **10**, 253–262 (2010).
- 1009 87. Shammass, M. K. *et al.* OMA1 mediates local and global stress responses against
1010 protein misfolding in CHCHD10 mitochondrial myopathy. *J. Clin. Invest.* **132**, (2022).
- 1011 88. Martin, M. Cutadapt removes adapter sequences from high-throughput sequencing
1012 reads. *EMBnet.journal* **17**, 10–12 (2011).
- 1013 89. Dobin, A. *et al.* STAR: ultrafast universal RNA-seq aligner. *Bioinformatics* **29**, 15–21
1014 (2013).
- 1015 90. Danecek, P. *et al.* Twelve years of SAMtools and BCFtools. *Gigascience* **10**, (2021).
- 1016 91. Liao, Y., Smyth, G. K. & Shi, W. featureCounts: an efficient general purpose program for
1017 assigning sequence reads to genomic features. *Bioinformatics* **30**, 923–930 (2014).
- 1018 92. Love, M. I., Huber, W. & Anders, S. Moderated estimation of fold change and dispersion
1019 for RNA-seq data with DESeq2. *Genome Biol.* **15**, 550 (2014).
- 1020 93. Xie, Z. *et al.* Gene Set Knowledge Discovery with Enrichr. *Curr Protoc* **1**, e90 (2021).
- 1021 94. Chen, E. Y. *et al.* Enrichr: interactive and collaborative HTML5 gene list enrichment
1022 analysis tool. *BMC Bioinformatics* **14**, 128 (2013).

- 1023 95. Kuleshov, M. V. *et al.* Enrichr: a comprehensive gene set enrichment analysis web
1024 server 2016 update. *Nucleic Acids Res.* **44**, W90-7 (2016).
- 1025 96. Liberzon, A. *et al.* The Molecular Signatures Database (MSigDB) hallmark gene set
1026 collection. *Cell Syst* **1**, 417–425 (2015).
- 1027 97. Kanehisa, M. & Goto, S. KEGG: kyoto encyclopedia of genes and genomes. *Nucleic*
1028 *Acids Res.* **28**, 27–30 (2000).
- 1029 98. R Core Team. A language and environment for statistical computing. Vienna, Austria: R
1030 Foundation for Statistical Computing. Preprint at (2019).
- 1031 99. Harms, M. J. *et al.* Mature Human White Adipocytes Cultured under Membranes
1032 Maintain Identity, Function, and Can Transdifferentiate into Brown-like Adipocytes. *Cell*
1033 *Rep.* **27**, 213-225.e5 (2019).
- 1034 100. Lord, S. J., Velle, K. B., Mullins, R. D. & Fritz-Laylin, L. K. SuperPlots: Communicating
1035 reproducibility and variability in cell biology. *J. Cell Biol.* **219**, (2020).
- 1036

Figure Legends

1037

1038

1039 **Figure 1. Generation of a Mfn2^{R707W} knock-in mouse.** (A) Wild-type (WT) nucleotide and amino
1040 acid sequence around the Arg 707 codon. The CRISPR/Cas9 nuclease target is indicated in *green*.
1041 Below is part of the ssODN template with mutated nucleotides in *blue*, including the upstream silent
1042 mutation (at codon 704-705) to generate an EcoRV restriction site. (B) Sanger sequencing
1043 confirmation of the knock-in (KI) with restriction site in a founder (F0). (C) Illustration of the genotyping
1044 strategy: mutant alleles will digest into 327 bp and 196 bp fragments in response to EcoRV digestion.
1045 (D) Ear biopsies were digested using chelix and *Mfn2* amplified by PCR, then digested using EcoRV.
1046 Representative SYBR Safe DNA gel demonstrating genotyping for two WT, heterozygous, and
1047 homozygous KI mice. Image is representative of other genotyping gels. (E) Western blot from inguinal
1048 and epididymal white adipose tissue (WAT), brown adipose tissue (BAT), liver and skeletal muscle for
1049 expression of Mfn1 and Mfn2. Tissues are from WT and homozygous Mfn2^{R707W} KI mice fed a 45%
1050 kcal high fat diet (HFD) for 6 months. Due to variability across tissues, both *Gapdh* and Beta-tubulin
1051 (*Tubb*) are given as loading controls. The image is representative of at least three biological
1052 replicates.

1053

1054

1055 **Figure 1-figure supplement 1. Expression of mitofusins on chow diet.** Western blots showing
1056 expression of Mfn2 and Mfn1 in liver (A), heart (B), skeletal muscle (C), BAT (D), inguinal WAT (E),
1057 and epididymal WAT (F) in WT and homozygous Mfn2^{R707W} KI mice fed chow diet for 6 months; and
1058 (G) expression of Mfn2 and Mfn1 in BAT in mice fed chow for 4 weeks. Each lane contains samples
1059 from a separate animal and blots are representative of at least three replicates. *Canx* (calnexin),
1060 *Gapdh*, and *Tubb* (β -tubulin) are loading controls.

1061

1062

1063 **Figure 1-figure supplement 2. Quantification of western blots for mitofusins in tissues of chow
1064 diet-fed mice.** Densitometric quantification of Mfn1 and Mfn2 bands from liver (A), heart (B), skeletal
1065 muscle (C), BAT (D), inguinal WAT (E), and epididymal WAT (F) in male mice fed chow diet for 6
1066 months; and (G) BAT in mice fed chow diet for 4 weeks. Data are from n=3-9 animals. Each point
1067 represents data from a separate animal. Asterisks indicate p-values from pairwise comparisons (T-
1068 tests) that are false-discovery rate (FDR)-adjusted for multiple tests (* p-FDR <.05). WT in *blue*,
1069 homozygous Mfn2^{R707W} KI in *green*.

1070

1071

1072 **Figure 1-figure supplement 3. Expression of mitofusins on high fat diet.** Western blots showing
1073 expression of Mfn2 and Mfn1 in liver (A), heart (B), skeletal muscle (C), BAT (D), inguinal WAT (E),
1074 and epididymal WAT (F) from WT and homozygous Mfn2^{R707W} KI mice fed a 45% kcal HFD for 6

1075 months. Each lane contains samples from a separate animal and blots are representative of at least
1076 three replicates. *Canx* (calnexin), *Gapdh*, and *Tubb* (β -tubulin) are given as loading controls.

1077

1078 **Figure 1-figure supplement 4.** Quantification of western blots for mitofusins in tissues of high fat
1079 diet-fed mice. Densitometric quantification of bands for Mfn1 and Mfn2 from male mice fed HFD for 6
1080 months is shown. Data are from liver (A), heart (B), skeletal muscle (C), BAT (D), inguinal WAT (E),
1081 and epididymal WAT (F). Data are from n=3-10 animals. Each point represents a separate animal.
1082 Asterisks indicate p-values from pairwise comparisons (T-tests) that are FDR-adjusted for multiple
1083 tests (* p-FDR <.05, ** p-FDR <.01). WT in *blue*, homozygous Mfn2^{R707W} KI in *green*.

1084

1085

1086 **Figure 2. Effect of Mfn2^{R707W} on mitochondrial structure and function.** (A) Representative
1087 transmission electron microscopy (TEM) images of BAT with zoomed-in images of mitochondria
1088 (highlighted in *yellow*) bordering lipid droplets (outlined in *red*). (B) Quantification of mitochondrial
1089 perimeter from TEM on BAT. Each dot represents data from an individual mitochondrial cross section
1090 with each diamond showing the separate 6 biological replicates. p.adj gives the FDR-adjusted p-value
1091 from across all TEM analyses. (C) Quantification of mitochondrial aspect ratio (length/width) from
1092 TEM of BAT. (D) Quantification of mitochondrial-lipid droplet contact from TEM, expressed as
1093 proportion (%) of lipid droplet in contact with mitochondrial membrane on BAT. (E) Number of cristae
1094 per mitochondrion from TEM of BAT. (F-G) Mitochondrial DNA content in tissues from mice fed chow
1095 diet (F) or HFD (G) for 6 months. Each data point represents a separate animal. p-values are from
1096 pairwise comparisons (T-tests) between WT and Mfn2^{R707W} KI that are FDR-adjusted for multiple tests
1097 (* p-FDR <.05). WT in *blue*, homozygous Mfn2^{R707W} KI in *green*. AU, arbitrary units.

1098

1099

1100 **Figure 2-figure supplement 1. Effect of Mfn2^{R707W} on mitochondrial morphology in white**
1101 **adipose tissue.** (A) Representative TEM images from inguinal WAT with zoomed-in images of
1102 mitochondria (highlighted in *yellow*) bordering lipid droplets (outlined in *red*). Quantification of
1103 mitochondrial perimeter (B) and aspect ratio (length/width) (C) from TEM in inguinal WAT. Each dot
1104 represents an individual mitochondrion with diamonds showing biological replicates. p.adj gives the
1105 FDR-adjusted p-value from across all TEM analyses. (D) TEM images from epididymal WAT with
1106 zoomed-in images of mitochondria (highlighted in *yellow*) bordering lipid droplets (outlined in *red*).
1107 Quantification of mitochondrial perimeter (E) and aspect ratio (length/width) (F) from TEM on
1108 epididymal WAT. FDR-adjusted p-values are from pairwise comparisons (T-tests) between WT and
1109 Mfn2^{R707W} KI. WT in *blue*, homozygous Mfn2^{R707W} KI in *green*.

1110

1111

1112 **Figure 2-figure supplement 2. Effect of Mfn2^{R707W} on mitochondrial morphology in liver, heart,**
1113 **and muscle.** (A) Representative TEM images from the heart with zoomed-in images of mitochondria
1114 (highlighted in *yellow*). (B) Quantification of mitochondrial perimeter from TEM on heart. Each dot

1115 represents an individual mitochondrion with diamonds showing biological replicates. p.adj gives the
1116 FDR-adjusted p-value from across all TEM analyses. (C) Quantification of mitochondrial aspect ratio
1117 (length/width) from TEM on heart. (D) TEM images from skeletal muscle with zoomed-in images of
1118 mitochondria (highlighted in *yellow*). Quantification of mitochondrial perimeter (E) and aspect ratio
1119 (length/width) (F) from TEM on skeletal muscle. (G) TEM images from liver with zoomed-in images of
1120 mitochondria (highlighted in *yellow*). Quantification of mitochondrial perimeter (H) and aspect ratio
1121 (length/width) (I) from TEM on liver. FDR-adjusted p-values are from pairwise comparisons (T-tests)
1122 between WT and Mfn2^{R707W} KI. WT in *blue*, homozygous Mfn2^{R707W} KI in *green*.

1123

1124

1125 **Figure 2-figure supplement 3. Altered expression of Oxphos protein subunits in adipose**
1126 **tissue.** Western blots showing expression of Oxphos protein subunit expression in mice fed chow diet
1127 for 6 months. Expression is shown from liver (A), heart (B), inguinal WAT (C), epididymal WAT (D),
1128 and BAT (E). Each lane contains samples from a separate animal and blots are representative of at
1129 least three replicates. *Canx* (calnexin) is used as total cellular control and *Tomm20* (or citrate
1130 synthetase (Cs)) is used as mitochondrial mass loading control.

1131

1132

1133 **Figure 2-figure supplement 4. Quantification of western blots for Oxphos subunits from**
1134 **tissues of chow diet-fed mice.** Densitometric quantification of bands for mitochondrial Oxphos
1135 subunits from male mice fed chow diet for 6 months. Data are from liver (A), heart (B), inguinal WAT
1136 (C), epididymal WAT (D), and BAT (E). Data are from n=3-8 animals per genotype. Each point
1137 represents a separate animal. Asterisks indicate p-values from pairwise comparisons (T-tests) that
1138 are FDR-adjusted for multiple tests (* p-FDR <.05, ** p-FDR <.01). WT in *blue*, homozygous
1139 Mfn2^{R707W} KI in *green*.

1140

1141

1142 **Figure 2-figure supplement 5. Mfn2^{R707W} does not impair brown adipose tissue thermogenic**
1143 **capacity.** *Ex vivo* mitochondrial respirometry in liver (A, n=4) and BAT (B, n=9). Each data point
1144 represents data from a separate animal. Eight-week-old chow diet fed mice were exposed to cold
1145 (10°C, n=16-18) or thermoneutrality (30°C, n=13-14) for 4 weeks and then maximum thermogenic
1146 capacity was tested using noradrenaline (NA) stimulation under anaesthesia. (C) Trend in energy
1147 expenditure (kcal/hr) before and after noradrenaline stimulation for cold (solid line) and thermoneutral
1148 (dashed line) housed animals. (D) Quantification of maximum (peak) energy expenditure. P-values
1149 represent the difference between groups comparing 10°C and 30°C. (E) Area under the curve
1150 analysis using the minimum value at the point of noradrenaline (NA) injection at the base of the curve.
1151 (F) Basal energy expenditure prior to NA injection. (G) Difference between peak and baseline energy
1152 expenditure under both conditions. WT in *blue*, homozygous Mfn2^{R707W} KI in *green*. Each data point
1153 represents results from an individual animal. FDR-adjusted p-values are from pairwise comparisons
1154 (T-tests) between groups as indicated.

1155

1156

1157 **Figure 3. No difference in fat mass or glucose homeostasis in Mfn2^{R707W} mice compared to WT**
1158 **mice on chow or high fat diet.** Seven-week-old mice were fed chow (n=8-12) or 45% kcal HFD
1159 (n=13-14) for 6 months. (A) Absolute body mass for mice fed chow (solid line) and HFD (dashed line)
1160 over 6 months. (B) Time-domain nuclear magnetic resonance (TD-NMR) measurement of fat and lean
1161 mass of mice fed HFD. (C) The ratio of tissue weights versus body mass for multiple tissues,
1162 including four WAT depots, from mice fed HFD. (D) Quantification of lipid droplet area from
1163 histological specimens of adipose tissue from mice fed HFD for 6 months. (E) Representative
1164 histological images from WAT, liver, and BAT from mice fed HFD. Analyses of mouse plasma lactate
1165 (F), plasma glucose (G), and insulin (H), homeostatic model of assessment of insulin resistance
1166 (HOMA-IR, I) after a 6 hr fast. Change in plasma glucose during intraperitoneal glucose tolerance test
1167 (J) and intraperitoneal insulin tolerance test (K). ns, p>.05 on unpaired T-tests, adjusted for multiple
1168 comparisons. WT in *blue*, homozygous Mfn2^{R707W} KI in *green*. Each data point represents an
1169 individual animal.

1170

1171

1172 **Figure 3-figure supplement 1. No evidence of altered fat mass or glucose homeostasis in**
1173 **Mfn2^{R707W} compared to WT mice on chow or high fat diet for 6 months.** Seven-week-old mice
1174 were fed chow diet (n=8-12) or 45% kcal HFD (n=13-14) for 6 months. (A) Relative (%) change of
1175 body mass for mice fed chow diet (solid line) and HFD (dashed line) over 6 months. (B) TD-NMR
1176 measurement of fat and lean mass in mice fed a chow diet for 6 months. (C) Analysis of mouse serum
1177 biochemistry after 6 months of diet and a 6 hr fast for total cholesterol. (D) The ratio of tissue weights
1178 versus body mass for multiple tissues, including four WAT depots, from mice fed chow diet for 6
1179 months. (E) Serum triglycerides. (F) Quantification of lipid droplet area from histological specimens of
1180 adipose tissue from mice fed chow diet for 6 months. (G) Quantification of relative hepatic steatosis
1181 from histological images of liver. (H) Serum aspartate aminotransferase. (I) qPCR of genes implicated
1182 in the integrated stress response, lipid metabolism or inflammation in liver from animals fed HFD for 6
1183 months. Raw expression values for target genes were normalised to three housekeeping genes
1184 (*36b4*, *B2m*, and *Hprt*) and expressed relative to WT liver. ns, p>.05 on unpaired T-tests, adjusted for
1185 multiple comparisons. WT in *blue*, homozygous Mfn2^{R707W} in *green*. Each data point represents
1186 results from an individual animal.

1187

1188

1189 **Figure 3-figure supplement 2. Similar phenotype in female Mfn2^{R707W} knock-in mice fed high fat**
1190 **diet for 6 months.** Seven-week-old female mice were fed 45% kcal HFD (n=5-11) for 6 months. (A)
1191 Absolute body mass for over 6 months. (B) Body mass after 12 weeks on HFD. (C) TD-NMR
1192 measurement of fat and lean mass of female mice after 12 weeks on HFD. (D-F) Analysis of mouse
1193 serum biochemistry after 12 weeks of diet and a 6 hr fast for serum glucose (D), serum insulin (E),
1194 and serum adiponectin (F). Analysis of mouse serum leptin at 4 weeks (G), 12 weeks (H), and 24

1195 weeks (I) on HFD after a 6 hr fast. WT in *blue*, homozygous Mfn2^{R707W} KI in *green*. Each data point
1196 represents an individual animal. Asterisks indicate p-values from pairwise comparisons (T-tests)
1197 between WT and Mfn2^{R707W} KI that are FDR-adjusted for multiple tests (** p-FDR <.001).

1198

1199

1200 **Figure 4. Mfn2^{R707W} causes an adipose tissue-specific induction of the integrated stress**
1201 **response.** qPCR of genes involved in the integrated stress response (ISR) for six tissues from
1202 animals fed chow diet for 6 months: *Atf4* (A), *Ddit3* (Chop, B), and *Atf5* (C). Each data point
1203 represents one animal. Target gene CT values were normalised to three housekeeping genes (*36b4*,
1204 *B2m*, and *Hprt*) and expressed relative to WT liver for each gene. WT in *blue*, homozygous Mfn2^{R707W}
1205 in *green*. p-values are FDR-adjusted for multiple tests. Western blots from BAT (D), epididymal WAT
1206 (E), and liver (F) illustrating Ser51-phosphorylation of eIF2 α and expression of Mthfd2 with calnexin
1207 (*Canx*) as loading control. Western blots are representative of at least three biological and technical
1208 replicates. (G) Volcano plot from bulk RNA sequencing (n=8 per genotype) of inguinal WAT from mice
1209 on HFD. Significantly differentially expressed genes (Log₂ fold change >1.5 and p-FDR <.001) are
1210 highlighted in orange. Pathway analysis using significantly differentially expressed genes for
1211 upregulated (H) and downregulated (I) Hallmark gene sets. The X-axis depicts a relative gene set
1212 enrichment score. All illustrated gene sets are enriched with p-FDR <.05. Asterisks indicate p-values
1213 from pairwise comparisons (T-tests) between WT and Mfn2^{R707W} KI that are FDR-adjusted for multiple
1214 tests (* p-FDR <.05, ** p-FDR <.01, *** p-FDR <.001, **** p-FDR <.0001).

1215

1216

1217 **Figure 4-figure supplement 1. Mfn2^{R707W} causes adipose tissue-specific induction of the**
1218 **integrated stress response with perturbation of mitochondrial gene expression.** qPCR of genes
1219 involved in the ISR for six tissues from animals fed a chow diet for 6 months: *Gdf15* (A) and *Fgf21* (B).
1220 Each data point represents data from a separate animal. Target gene CT values were normalised
1221 against three housekeeping genes (*36b4*, *B2m*, and *Hprt*) and expressed relative to WT liver for each
1222 gene. P-values are FDR-adjusted for multiple tests. Serum FGF-21 (C) and GDF-15 (D) after 6
1223 months of chow diet or HFD. Western blots from inguinal WAT (E), skeletal muscle (F), and heart (G)
1224 illustrating Ser51-phosphorylation of eIF2 α and expression of Mthfd2 with calnexin (*Canx*) as loading
1225 control. Western blots are representative of at least three biological replicates. Mthfd2 in heart (G) is
1226 the upper band within the box, as indicated by a horizontal line. (H) Heatmap of all genes from the
1227 citrate acid (tricarboxylic acid (TCA)) cycle KEGG pathway. Colour illustrates the Log₂ fold change
1228 normalised per gene. Those annotated with orange in the leftmost column had significant differential
1229 gene expression (DGE) with p-FDR <.001. (I) Heatmaps comparing mRNA expression of
1230 mitochondrial- and nuclear-encoded mitochondrial genes from inguinal WAT from HFD-fed animals.
1231 Asterisks indicate p-values from pairwise comparisons (T-tests) between WT and Mfn2^{R707W} KI that
1232 are FDR-adjusted for multiple tests (** p-FDR <.001).

1233

1234

1235 **Figure 4-figure supplement 2. Quantification of western blots for components of the integrated**
1236 **stress response in high fat diet-fed mice.** Densitometric quantification of bands for Mthfd2 and
1237 phosphorylated Ser-51 eIF2 α from male mice fed HFD for 6 months. (A) BAT, (B) epididymal WAT,
1238 (C) liver, (D) inguinal WAT, (E) skeletal muscle, and (F) heart. Data are from 3-9 animals. Each point
1239 represents a separate animal. Asterisks indicate p-values from pairwise comparisons (T-tests)
1240 between WT and Mfn2^{R707W} KI that are FDR-adjusted for multiple tests (* p-FDR <.05, ** p-FDR <.01,
1241 *** p-FDR <.001). WT in *blue*, homozygous Mfn2^{R707W} KI in *green*.

1242

1243

1244 **Figure 4-figure supplement 3. Mfn2^{R707W} does not affect Oma1 or Opa1 processing in heart,**
1245 **liver, and muscle.** Western blots of heart (A), liver (B), and skeletal muscle (C) for Opa1 and Oma1
1246 are shown. Tissues are from male mice fed chow diet for 6 months. Each lane contains samples from
1247 a separate animal, with band intensity quantified densitometrically. Opa1 is quantified as percentage
1248 of the short form of Opa1 (bands c and e of S-Opa1) to total Opa1 (long and short forms, bands a-e).
1249 ns, p>.05 on unpaired T-tests, adjusted for multiple comparisons. WT in *blue*, homozygous Mfn2^{R707W}
1250 KI in *green*.

1251

1252

1253 **Figure 4-figure supplement 4. Evidence of modest activation of the Oma1-Opa1 pathway in**
1254 **brown adipose tissue from Mfn2^{R707W} mice.** Western blots of BAT for Opa1 and Oma1 are shown.
1255 Tissues are from male mice fed chow diet. (A) BAT (chow diet for 4 weeks), (B) BAT (chow diet for 6
1256 months), (C) Epididymal WAT (chow diet for 6 months), and inguinal WAT (chow diet for 6 months).
1257 Each lane contains samples from a separate animal with band intensity quantified densitometrically.
1258 Opa1 is quantified as percentage of the short form of Opa1 (bands c and e of S-Opa1) to total Opa1
1259 (long and short forms, bands a-e). ns, p>.05 on unpaired T-tests, adjusted for multiple comparisons.
1260 WT in *blue*, homozygous Mfn2^{R707W} KI in *green*. * p-FDR <.05.

1261

1262

1263 **Figure 4-figure supplement 5. Transcriptional evidence of upregulation of the unfolded protein**
1264 **response and mTorc1 pathways in adipose tissue.** (A) Volcano plot from bulk RNA sequencing
1265 (n=7 WT and n=6 KI) of inguinal WAT from mice on chow diet, where significantly differentially
1266 expressed genes (Log₂ fold change >1.5 and p-FDR <.001) are highlighted in *orange*. Pathway
1267 analysis using significantly differentially expressed genes for upregulated (B) and downregulated (C)
1268 Hallmark gene sets. X-axis depicts a relative gene set enrichment score. (D) Volcano plot from bulk
1269 RNA sequencing (n=6 per genotype) of BAT from mice on HFD, where significantly differentially
1270 expressed genes (Log₂ fold change >1.5 and p-FDR <.001) are highlighted in *green*. Pathway
1271 analysis using significantly differentially expressed genes for upregulated (E) and downregulated (F)
1272 Hallmark gene sets. X-axis depicts a relative gene set enrichment score. All illustrated gene sets are
1273 enriched with p-FDR <.05. (G) Scatter plot of the top 100 up-/down-regulated genes from bulk RNA
1274 sequencing from inguinal WAT. For each gene, the fold change observed under HFD is plotted on the

1275 x-axis and fold change under chow diet is shown on the y-axis. P-values for each dietary condition are
1276 shown using size (HFD) and colour (chow diet).

1277

1278

1279 **Figure 5. Mfn2^{R707W} decreases adipose secretion of leptin and adiponectin.** Fasting serum leptin
1280 (A) and adiponectin (B) from mice after 6 months on chow diet or HFD. Asterisks indicate t-tests
1281 comparing WT and Mfn2^{R707W} KI with p-values adjusted for multiple testing. (C) Relationship between
1282 leptin and body weight for animals fed HFD. Each data point represents one measurement of leptin,
1283 with multiple measurements per animal. Shaded area represents the 95% confidence interval. Data
1284 are from n=13-14 animals. qPCR of *Lep* (D) and *Adipoq* (E) from WAT depots. Each data point
1285 represents data from a separate animal. Target gene CT values were normalised against three
1286 housekeeping genes (*36b4*, *B2m*, and *Hprt*) and expressed relative to WT for each condition. (F-I)
1287 mRNA expression of *Atf4*, *Chop*, *Lep*, and *Adipoq* in primary adipocytes treated with either DMSO
1288 control or Thapsigargin (TG, 150 nM) or Tunicamycin (TN, 5 µg/mL) for 6 hr. Each data point
1289 represents an individual well from a separate biological experiment (n=5). Asterisks indicate
1290 significance on one-way ANOVA with correction for multiple comparisons. (J) Leptin and (K)
1291 Adiponectin secretion from primary adipocytes treated with either DMSO control or Thapsigargin (TG,
1292 150 nM) or Tunicamycin (TN, 5 µg/mL) over 6 hr. Asterisks indicate significance on one-way ANOVA
1293 with correction for multiple comparisons. (L) Representative western blots of primary adipocytes
1294 treated with either DMSO control or Thapsigargin (TG, 150 nM) or Tunicamycin (TN, 5 µg/mL) for 6
1295 hr. (M) Fasting serum adipisin (complement factor D) from mice after 6 months on chow diet or HFD.
1296 Asterisks indicate p-values from pairwise comparisons (T-tests) between indicated groups that are
1297 FDR-adjusted for multiple tests (* p-FDR <.05, ** p-FDR <.01, *** p-FDR <.001, **** p-FDR <.0001).

1298

1299

1300 **Figure 5-figure supplement 1. Mfn2^{R707W} decreases adipose leptin and adiponectin secretion**
1301 **from multiple adipose depots and in different dietary conditions.** (A) Leptin secretion from
1302 explants of epididymal WAT in basal conditions and after insulin-dexamethasone stimulation. (B)
1303 Adiponectin secretion from epididymal WAT explants. (C) qPCR of *Lep* and *Adipoq* from epididymal
1304 explants from animals fed a HFD, where each data point represents an explant from a separate
1305 animal (n=11-13). (D) Relationship between leptin and body weight for animals on chow diet. Each
1306 data point represents one measurement of leptin, with multiple measurements per animal. Shaded
1307 area represents the 95% confidence interval. Data are from n=8-12 animals. Asterisks indicate p-
1308 values from pairwise comparisons (T-tests) between indicated groups that are FDR-adjusted for
1309 multiple tests (* p-FDR <.05, ** p-FDR <.01, **** p-FDR <.0001).

1310

1311

1312 **Figure 5-figure supplement 2. Mfn2^{R707W} decreases leptin and adiponectin protein expression**
1313 **in white adipose tissue.** Western blots showing expression of leptin and adiponectin in male mice
1314 fed 45% kcal HFD for 6 months from epididymal (A) and inguinal (B) WAT. Expression is shown from

1315 epididymal and inguinal WAT with *Gapdh* used as a loading control. Each lane contains samples from
1316 a separate animal with band intensity quantified densitometrically. Asterisks indicate p-values from
1317 pairwise comparisons (T-tests) between WT and Mfn2^{R707W} KI that are FDR-adjusted for multiple tests
1318 (** p-FDR <.01, **** p-FDR <.0001). WT in *blue*, homozygous Mfn2^{R707W} KI in *green*.
1319

1320

Tables

1321

1322

	Chow diet			High fat diet		
	WT	Knock-in	p-FDR	WT	Knock-in	p-FDR
Weight (g)	39.9 (1.2)	40.9 (1.4)	1	48.4 (1.7)	45.7 (1.5)	0.51
Lean mass (g)	19.97 (0.44)	20.53 (0.53)	0.85	16.50 (0.39)	15.51 (0.42)	0.2
Fat mass (g)	12.41 (0.97)	12.67 (1.29)	1	22.39 (1.63)	24.09 (1.10)	0.79
Leptin (ug/L)						
4 weeks	3.6 (0.9)	1.3 (0.2)	0.17	14.3 (2.6)	4.8 (0.5)	0.01
8 weeks	4.5 (0.8)	1.6 (0.3)	0.056	20.8 (3.3)	8.6 (0.9)	0.007
12 weeks	7.6 (0.4)	2.3 (0.5)	0.045	19.3 (4.0)	11.4 (1.5)	0.31
24 weeks (fasting)	15.4 (3.4)	6.0 (1.3)	0.047	57.0 (8.9)	15.6 (1.5)	0.003
Adiponectin (mg/L)						
4 weeks	24.8 (1.0)	16.4 (2.3)	0.068	21.0 (0.4)	11.0 (3.3)	4.20E-10
8 weeks	20.0 (0.7)	11.0 (0.7)	1.50E-05	29.4 (1.4)	16.0 (0.7)	5.30E-07
12 weeks	29.0 (1.4)	14.7 (0.7)	4.50E-05	33.0 (0.8)	18.2 (0.9)	7.20E-09
24 weeks (fasting)	29.0 (2.3)	15.4 (2.3)	0	27.9 (0.9)	15.5 (0.6)	4.30E-09
Fgf21 (ng/L)						
20 weeks	238 (26)	292 (22)	0.50	2,655 (203)	2,475 (268)	1
28 weeks	444 (51)	638 (96)	0.24	3,355 (911)	2,919 (289)	1
Gdf15 (ng/L) (28 weeks)	132 (6)	172 (14)	0.067	250 (36)	217 (23)	1
Glucose (mmol/L)	10.0 (0.5)	10.4 (0.4)	1	11.7 (0.5)	11.4 (0.5)	1
Insulin (µg/L) (33 weeks)	1.8 (0.3)	2.0 (0.3)	1	1.7 (0.2)	1.2 (0.1)	0.17
HOMA-IR	141.3 (29.0)	159.2 (23.3)	1	152.2 (22.9)	104.8 (12.1)	0.26
Insulin (µg/L) (GTT baseline)	1.8 (0.4)	2.3 (0.7)	1	2.3 (0.4)	1.4 (0.1)	0.1
Lactate (mmol/L)	4.2 (0.3)	4.4 (0.2)	1	4.5 (0.4)	4.8 (0.2)	1
NEFA (µmol/L)	1,688 (78)	1,564 (46)	0.39	922 (87)	1030 (90)	0.90
TG (mmol/L)	1.1 (0.1)	1.0 (0.1)	1	0.8 (0.1)	0.7 (0.0)	0.76
Total cholesterol (mmol/L)	3.0 (0.1)	3.1 (0.1)	1	6.3 (0.3)	5.2 (0.2)	0.042
ALT (IU/L)	64 (6)	68 (5)	1	144 (33)	45 (9)	0.076
AST (IU/L)	114 (20)	118 (16)	1	207 (32)	162 (22)	0.65

1323

1324

1325

1326

1327

1328

1329

1330

Table 1: Weights and serum biochemistry for mice on chow or high fat diet for 6 months. Seven-week-old mice were fed chow (n=8-12) or 45% kcal HFD (n=13-14) for 6 months. Blood was taken 4 weekly with 6 hr fasting blood taken on week 28. p-FDR are false-discovery rate adjusted p-values derived from unpaired T-tests. Values in brackets referred to standard error of the mean. ALT, alanine aminotransferase; AST, aspartate aminotransferase; FGF21, fibroblast growth factor 21; Gdf15, Growth and differentiation factor 15; HOMA-IR, Homeostatic Model Assessment for Insulin Resistance; NEFA, non-esterified fatty acids.

Human	Phenocopy?	Mouse
Upper body adipose overgrowth	No	No difference in weight of any adipose depots
Lower limb lipoatrophy	No	
Insulin resistance	No	No difference on GTT or fasting insulin
Lower serum leptin concentration	Yes	Seen on chow or HFD; lower secretion seen from adipose explants
Severely reduced adipose leptin mRNA expression	Partial	Modest decrease only; only significant in some analyses
Lower serum adiponectin concentration	Yes	Seen on chow or HFD; lower secretion seen from adipose explants
Severely reduced adipose adiponectin mRNA expression	Yes	Seen on chow or HFD and in adipose explants
No change in WAT MFN2 protein expression (only over-grown WAT studied)	Yes	No difference in any tissue studied, though variable in WAT and BAT.
No difference in adipocyte size	Yes	True on both chow and HFD
Disorganised, fragmented WAT mitochondria on TEM	Partial	More circular mitochondria with trend towards reduced cristae
Upregulation of nuclear and down regulation of mitochondrial Oxphos transcriptional pathway	Yes	True in inguinal and epididymal WAT, and BAT
Lower Oxphos complex II and III but preserved complex I and IV protein	Partial	Lower complex I and IV protein in WAT
Lower WAT mtDNA	Partial	Lower mtDNA in BAT but not WAT
Transcriptional activation of ISR	Yes	Seen in inguinal and epididymal WAT, and BAT

1332 **Table 2: Comparison of human *MFN2*^{R707W}-associated lipodystrophy with phenotype of**
1333 ***Mfn2*^{R707W/R707W} mice.** BAT, brown adipose tissue; GTT, glucose tolerance test; HFD, high fat diet;
1334 ISR, integrated stress response; MFN2, mitofusin 2; mRNA, messenger ribose nucleic acid; mtDNA,
1335 mitochondrial DNA; PLIN1, perilipin 1; TEM, transmission electron microscope; WAT, white adipose
1336 tissue.
1337

Supplementary Table Legends

1338

1339

1340 **Supplementary Table 1:** Antibodies used in this study.

1341

1342 **Supplementary Table 2:** Primer sequences used in this study. Fwd, forward primer; Rv, reverse
1343 primer.

1344

Source data titles

1345

1346

1347 **Figure 1-Source data.** Raw & annotated immunoblots from Figure 1 E.

1348 **Figure 1-Figure Supplement 1-Source data.** Raw & annotated immunoblots from Figure 1-
1349 Figure Supplement 1.

1350 **Figure 1-Figure Supplement 3-Source data.** Raw & annotated immunoblots from Figure 1-
1351 Figure Supplement 3.

1352 **Figure 2-Figure Supplement 3-Source data.** Raw & annotated immunoblots from Figure 2-
1353 Figure Supplement 3.

1354 **Figure 4-Source data.** Raw & annotated immunoblots from Figure 4 D-F.

1355 **Figure 4- Figure Supplement 1-Source data.** Raw & annotated immunoblots from Figure
1356 4-Figure Supplement 1 E-G.

1357 **Figure 4- Figure Supplement 3-Source data.** Raw & annotated immunoblots from Figure
1358 4-Figure Supplement 3.

1359 **Figure 4- Figure Supplement 4-Source data.** Raw & annotated immunoblots from Figure
1360 4-Figure Supplement 4.

1361 **Figure 5-Source data.** Raw & annotated immunoblots from Figure 5 L.

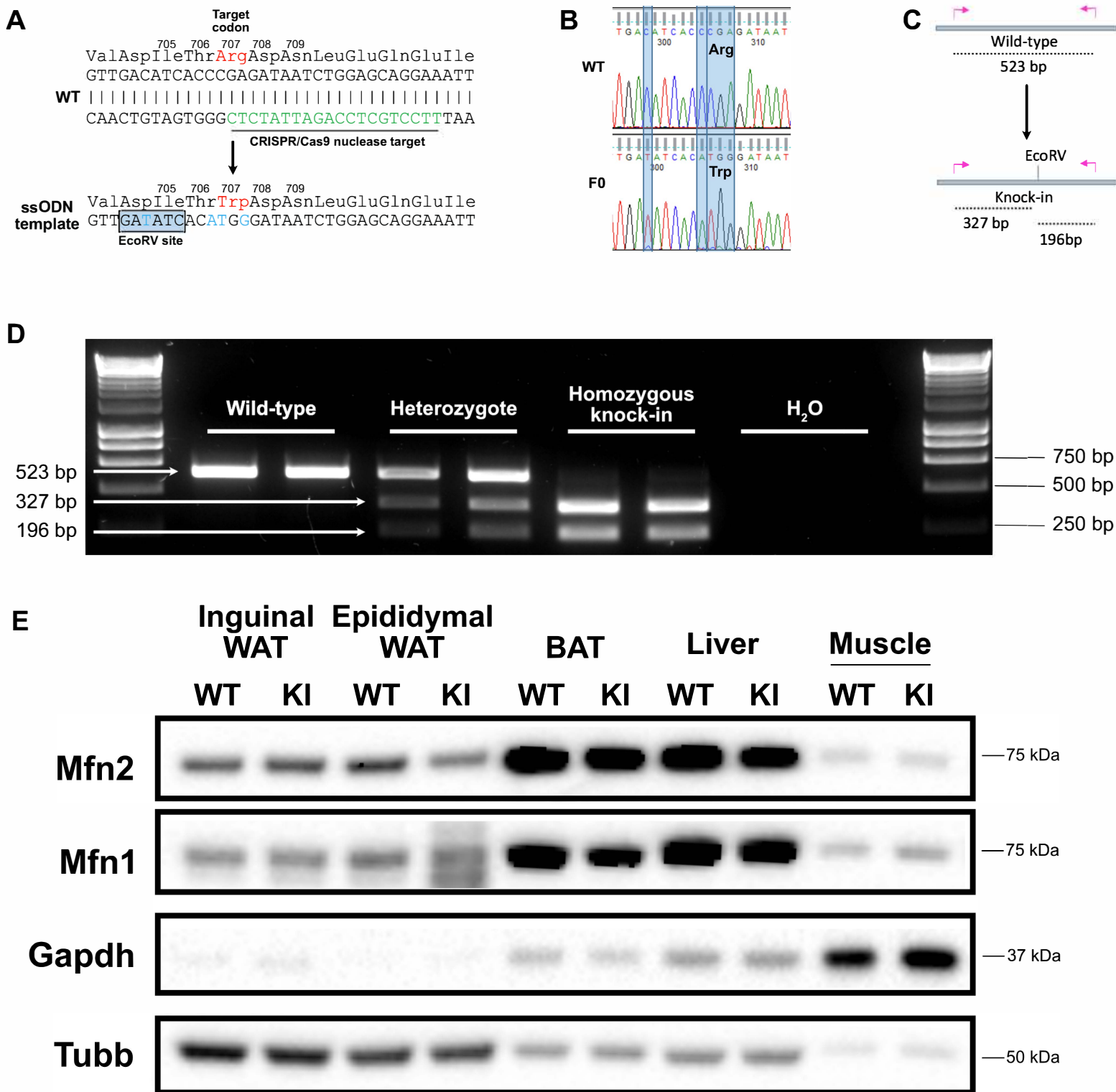


Figure 1

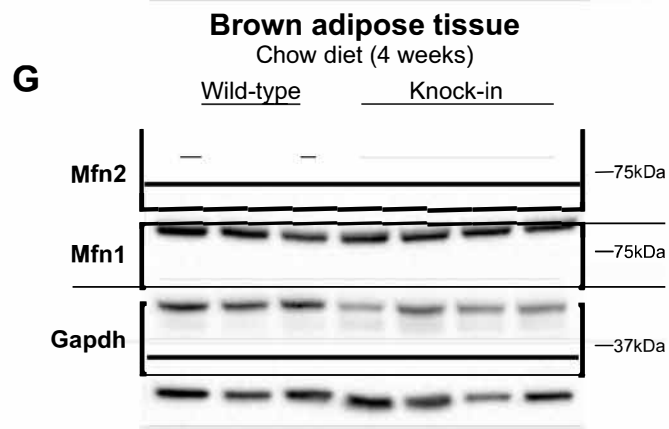
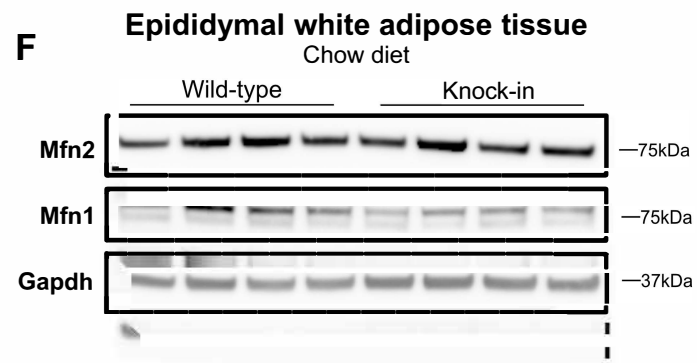
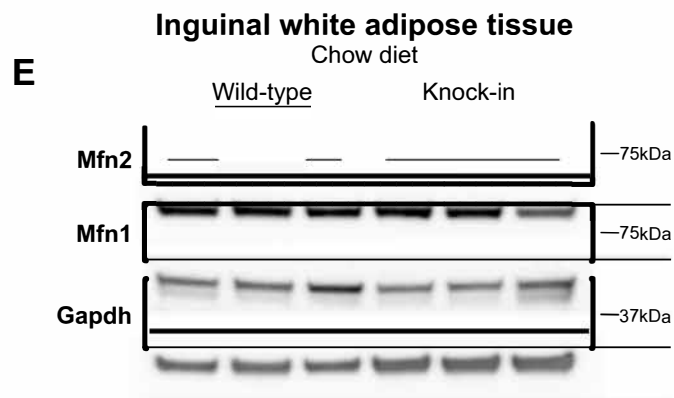
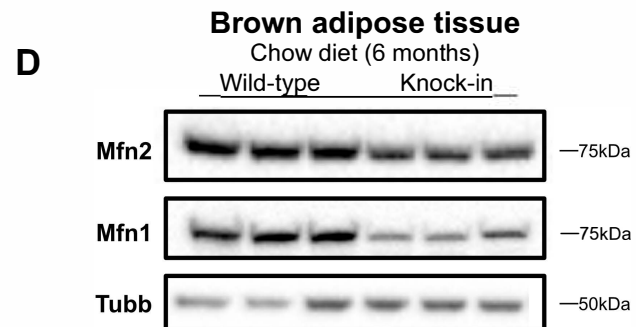
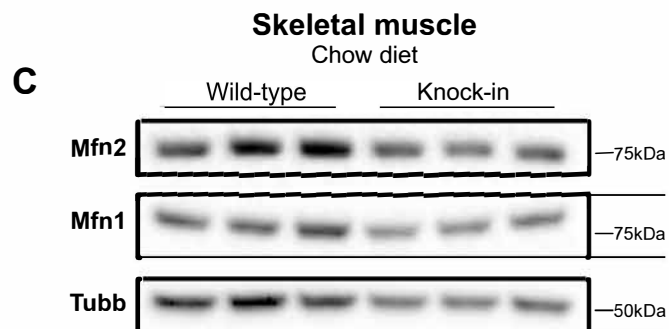
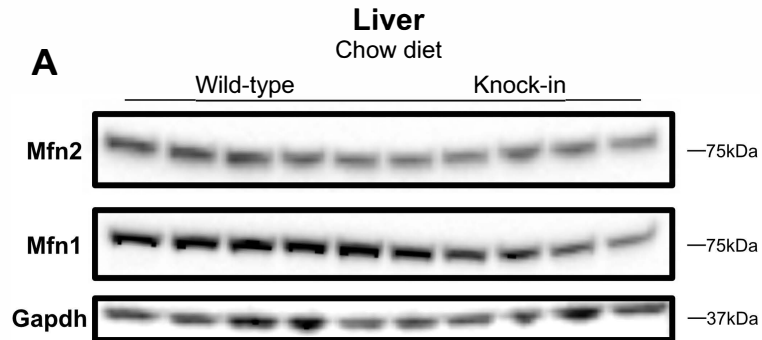


Figure 1 - Figure Supplement 1

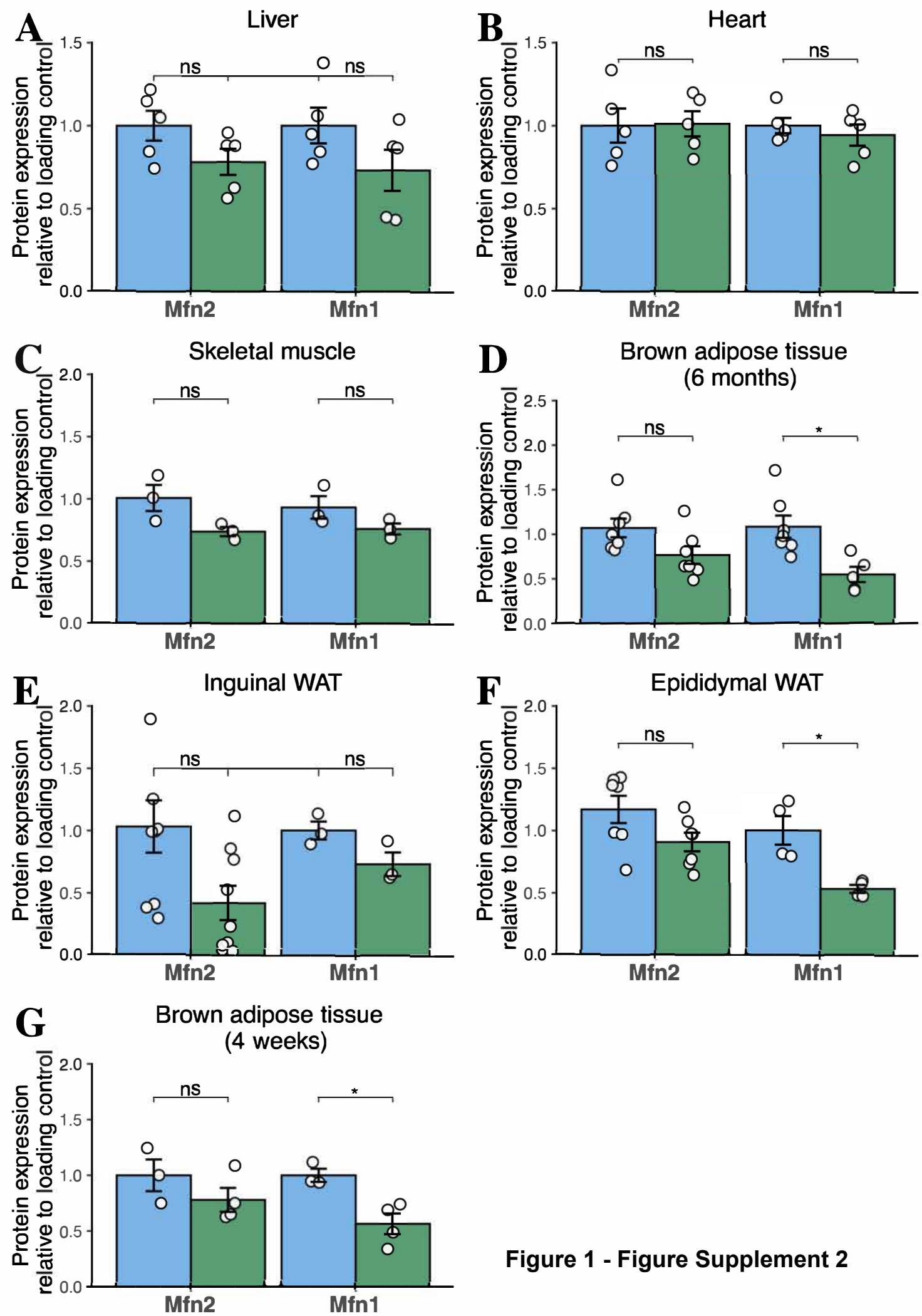


Figure 1 - Figure Supplement 2

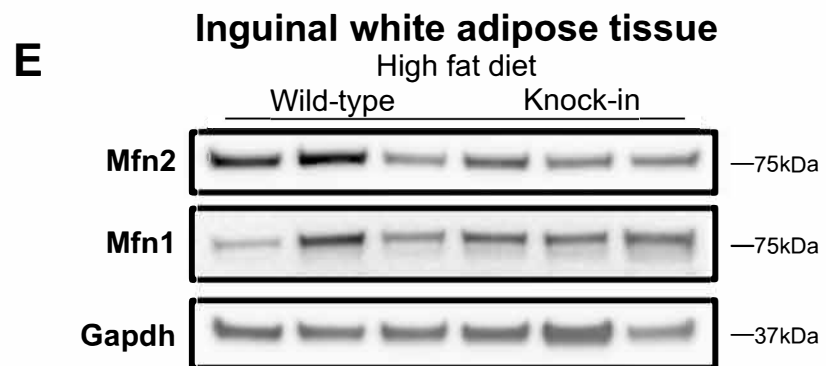
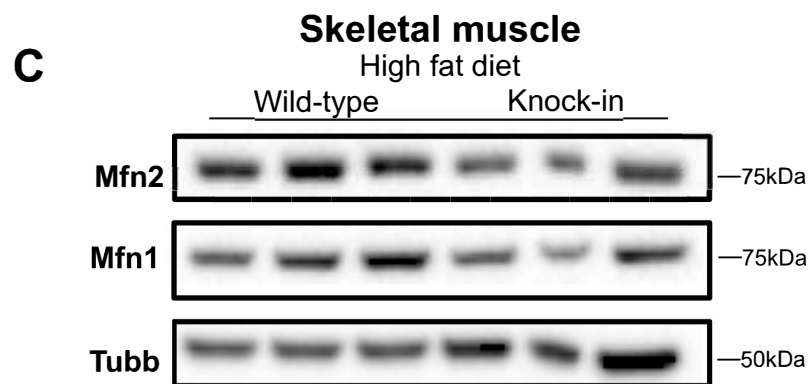
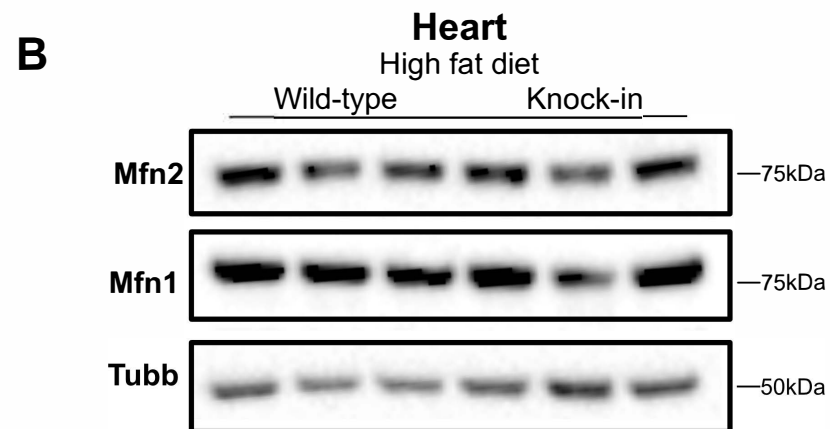
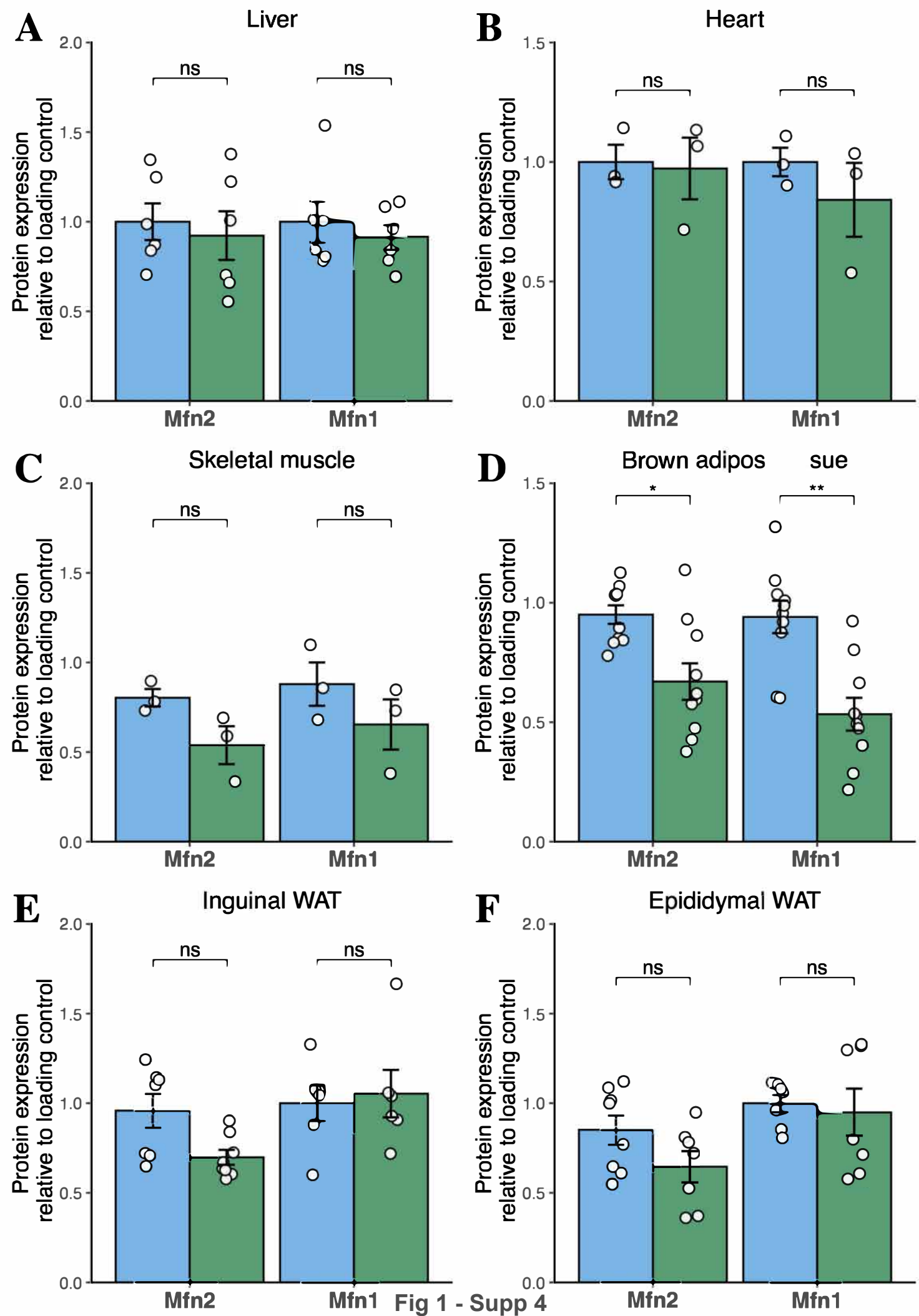


Figure 1 - Figure Supplement 3



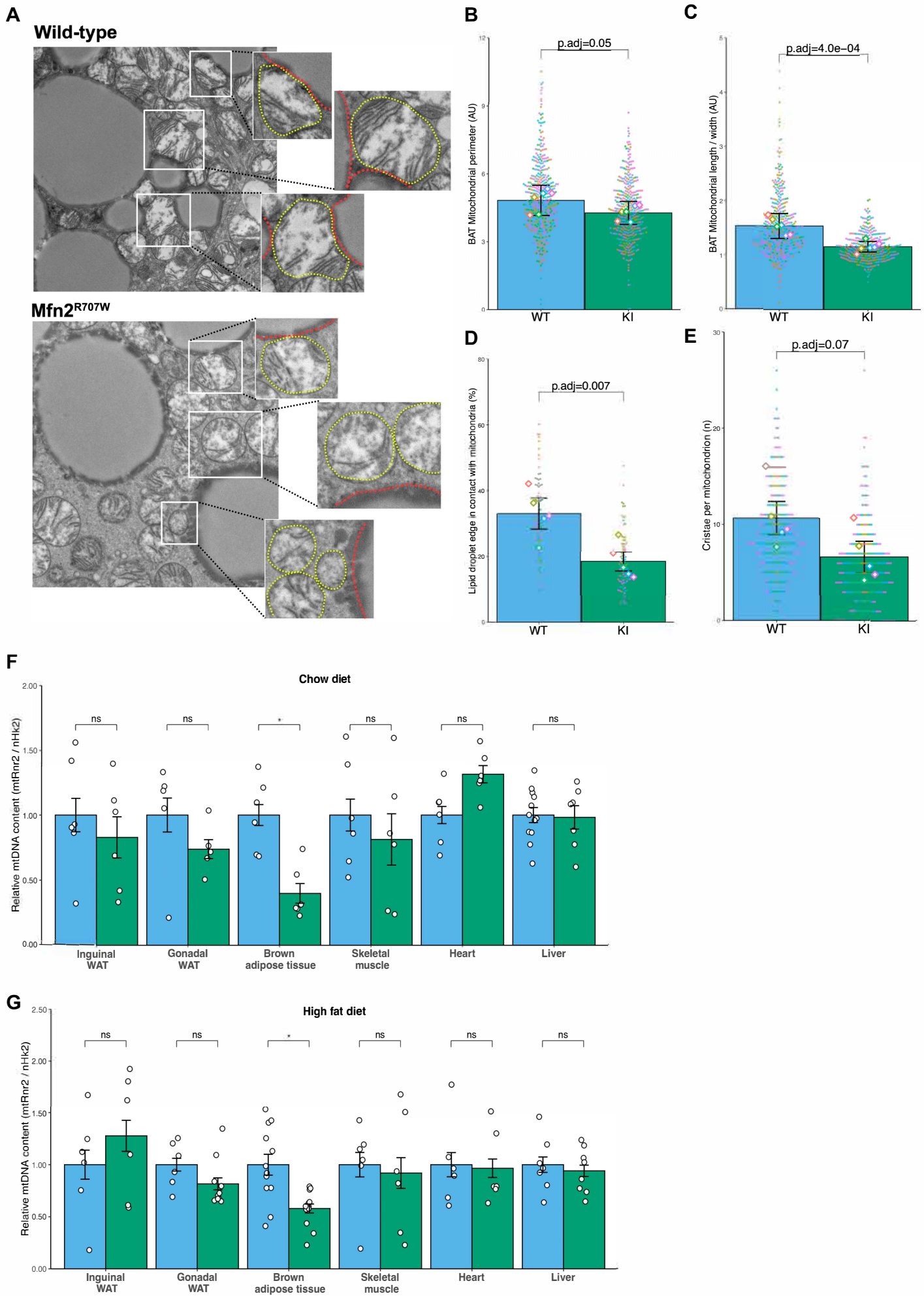


Figure 2

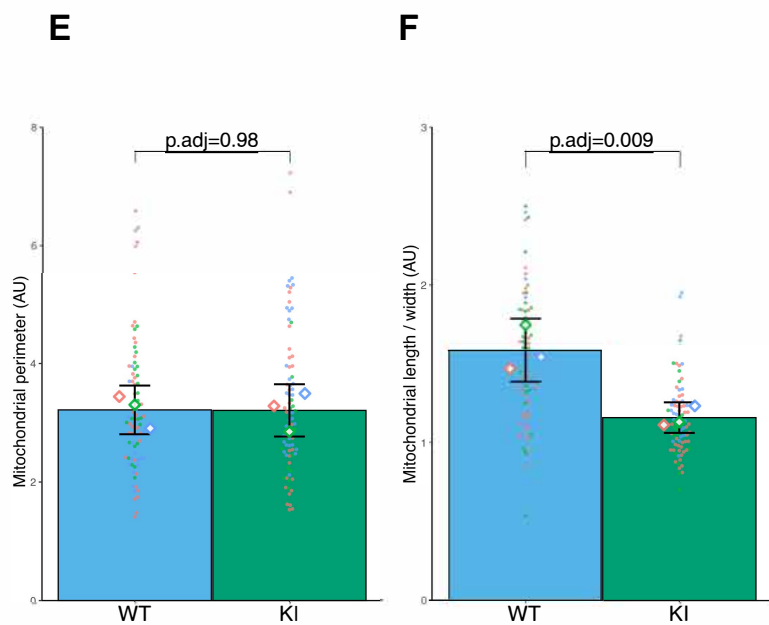
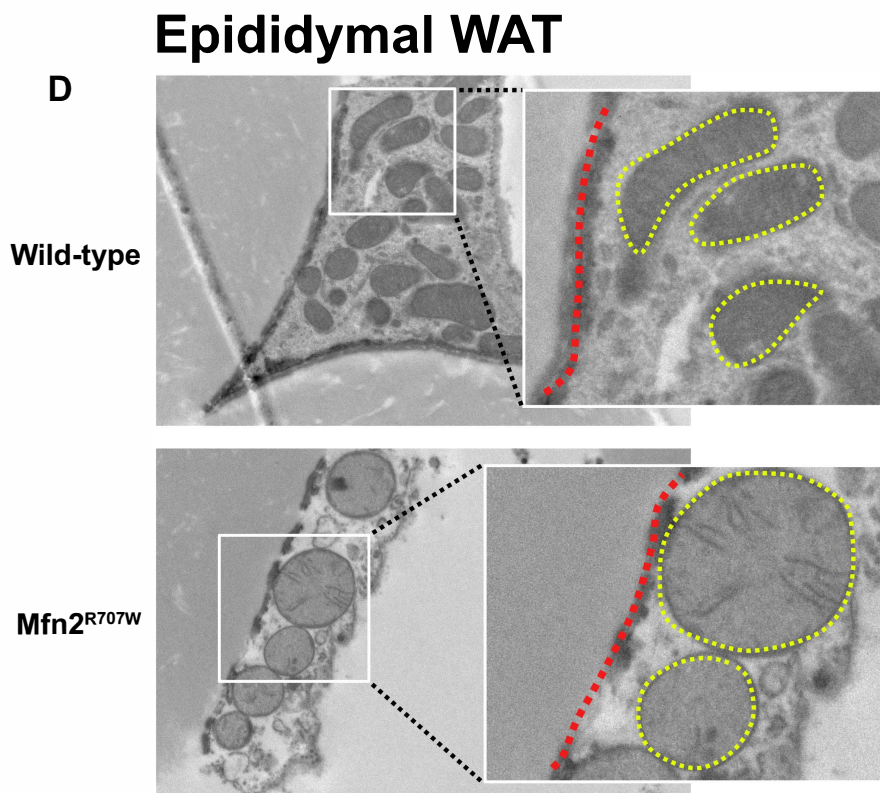
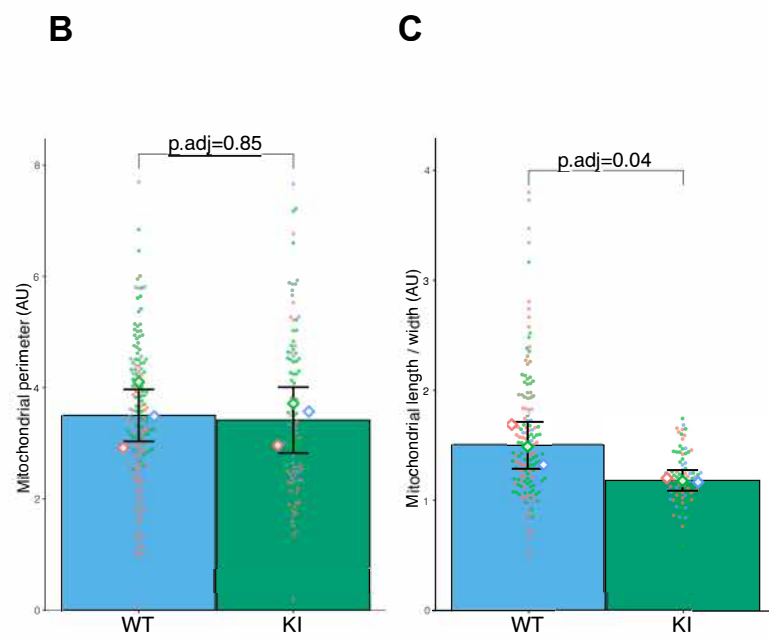
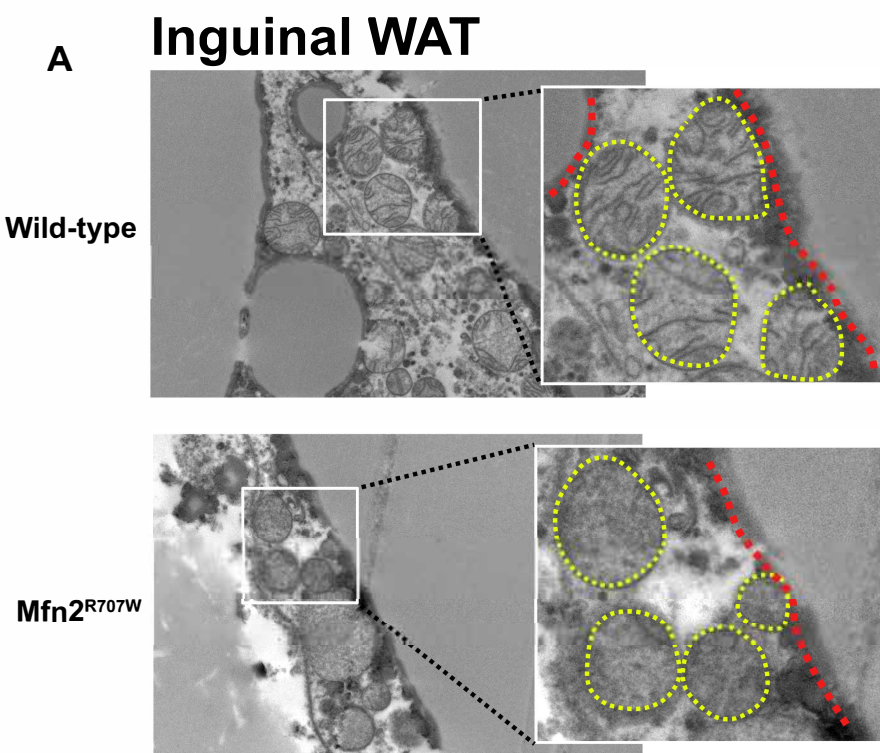


Figure 2 - Figure Supplement 1

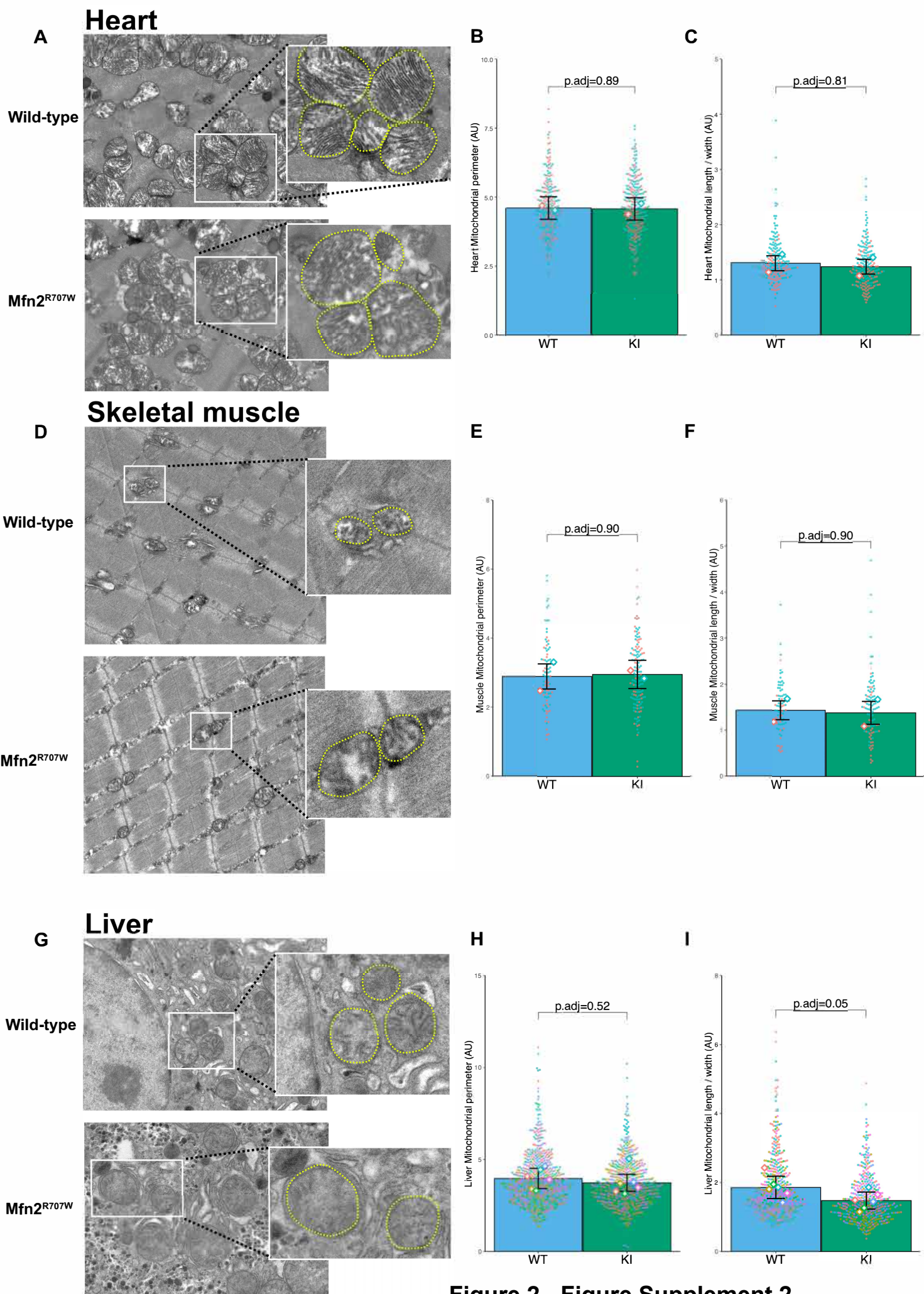


Figure 2 - Figure Supplement 2

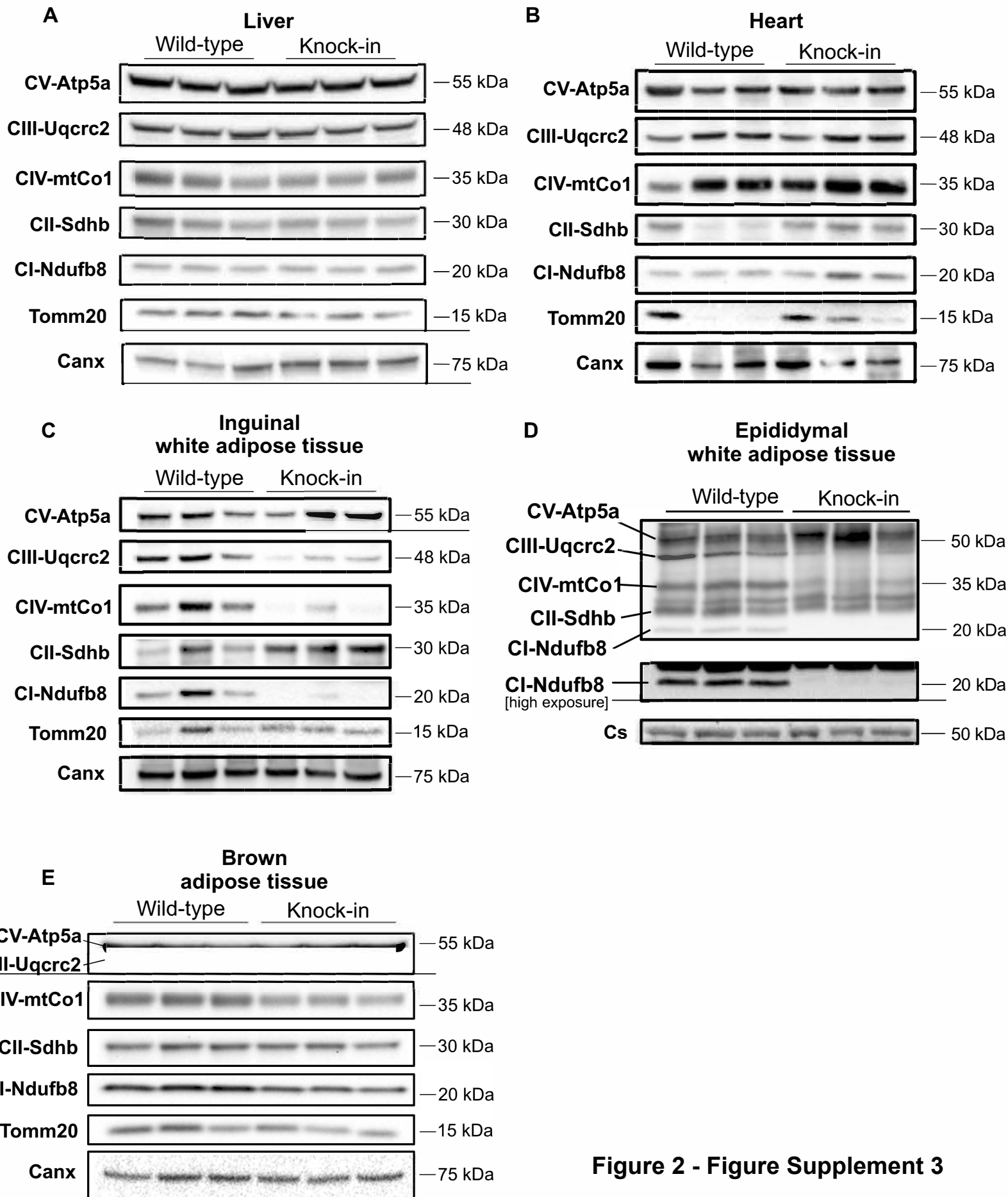


Figure 2 - Figure Supplement 3

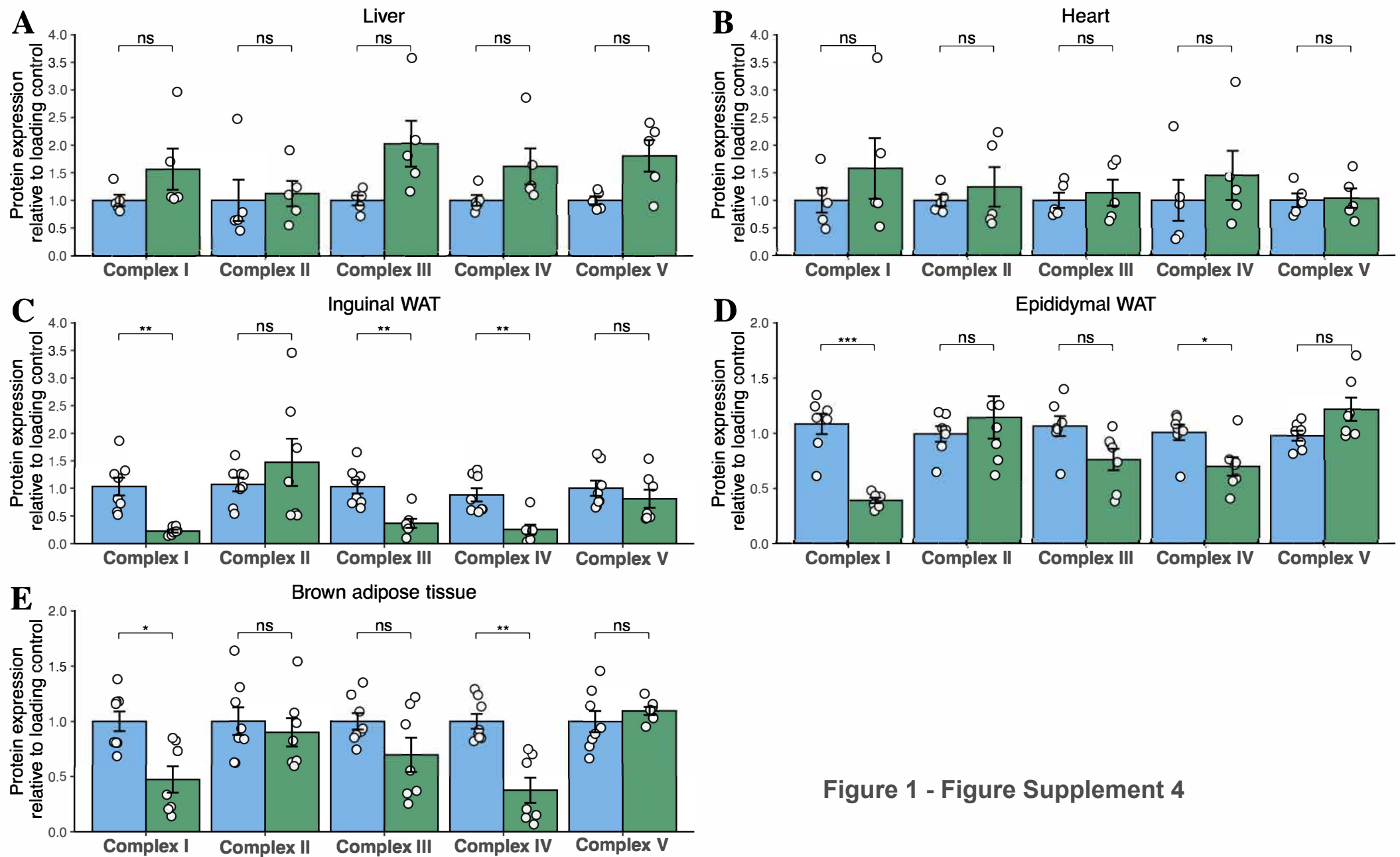


Figure 1 - Figure Supplement 4

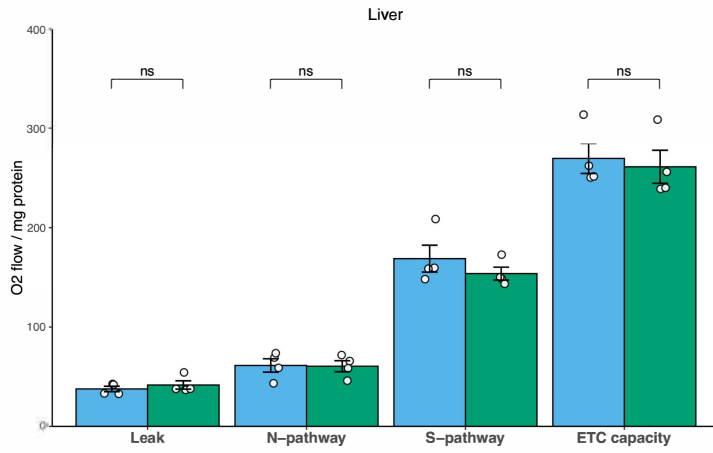
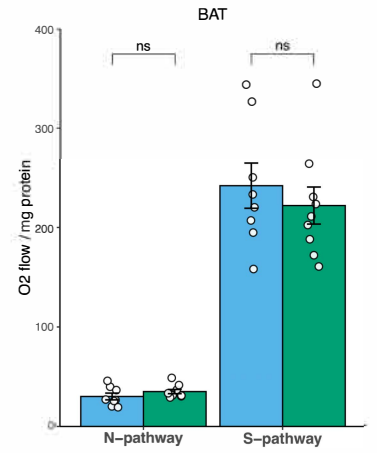
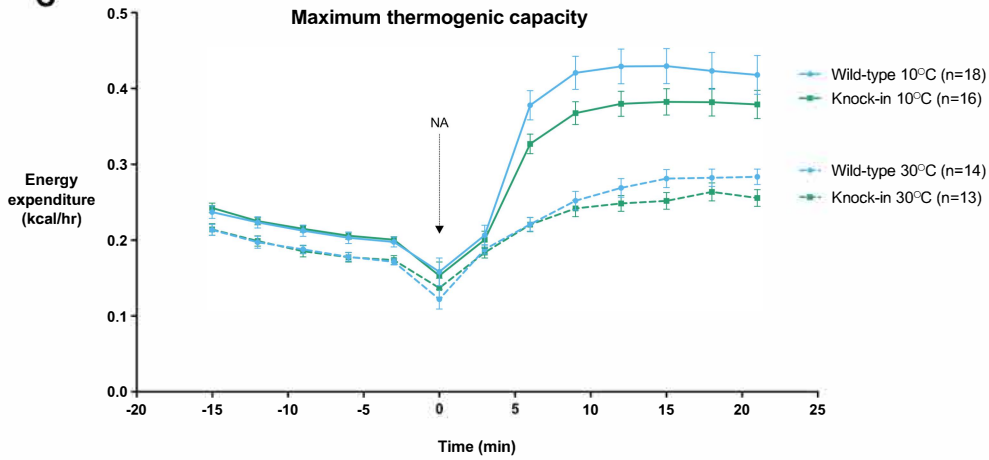
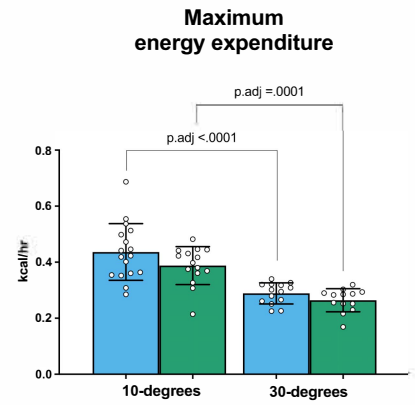
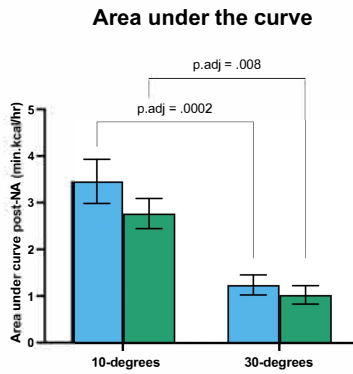
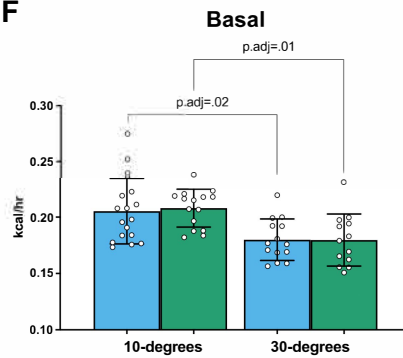
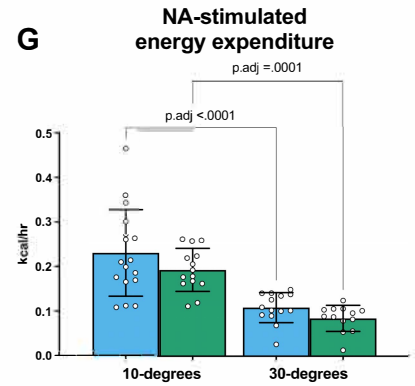
A**B****C****D****E****F****G**

Figure 1 - Figure Supplement 5

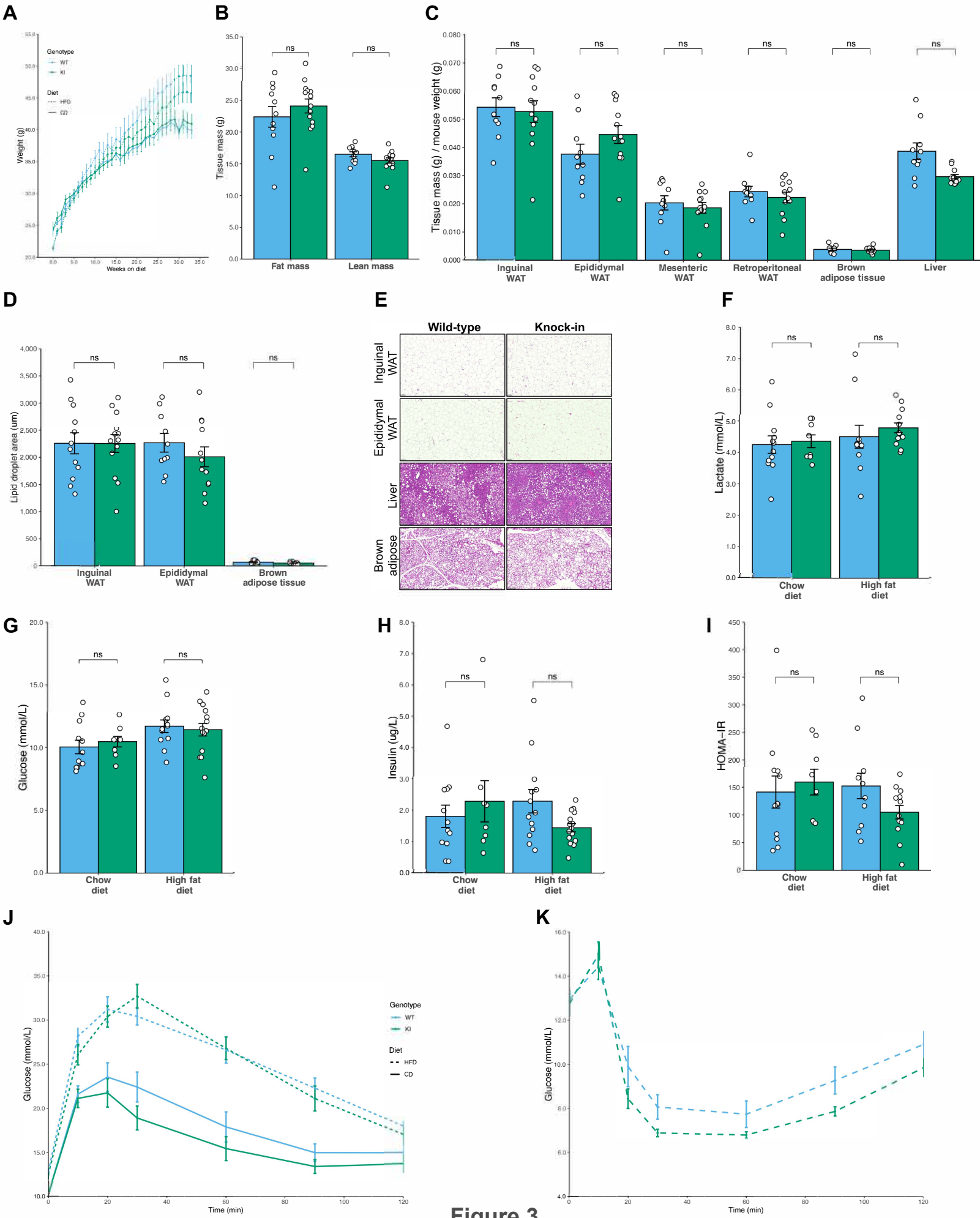


Figure 3

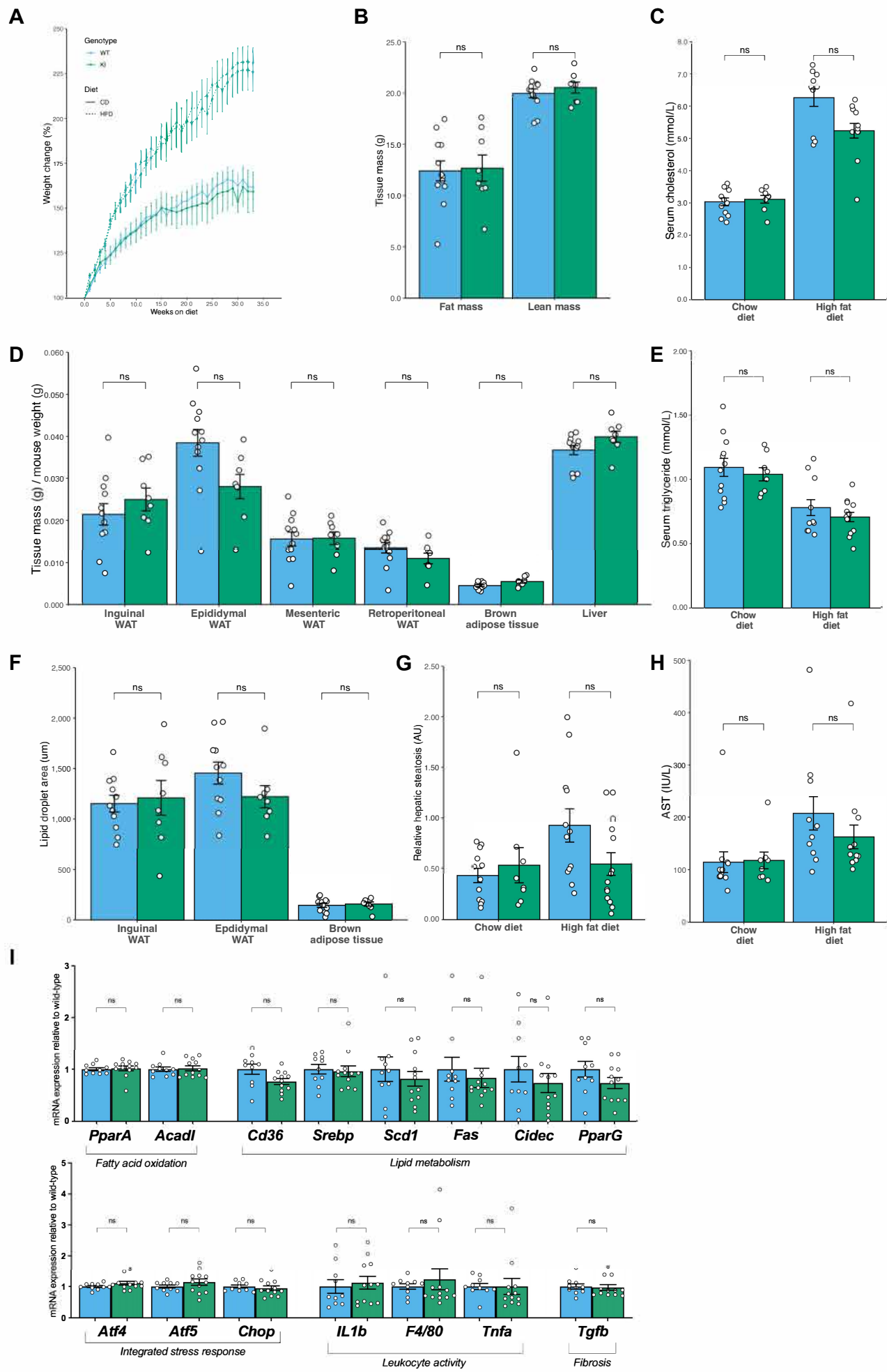


Figure 3 - Figure Supplement 1

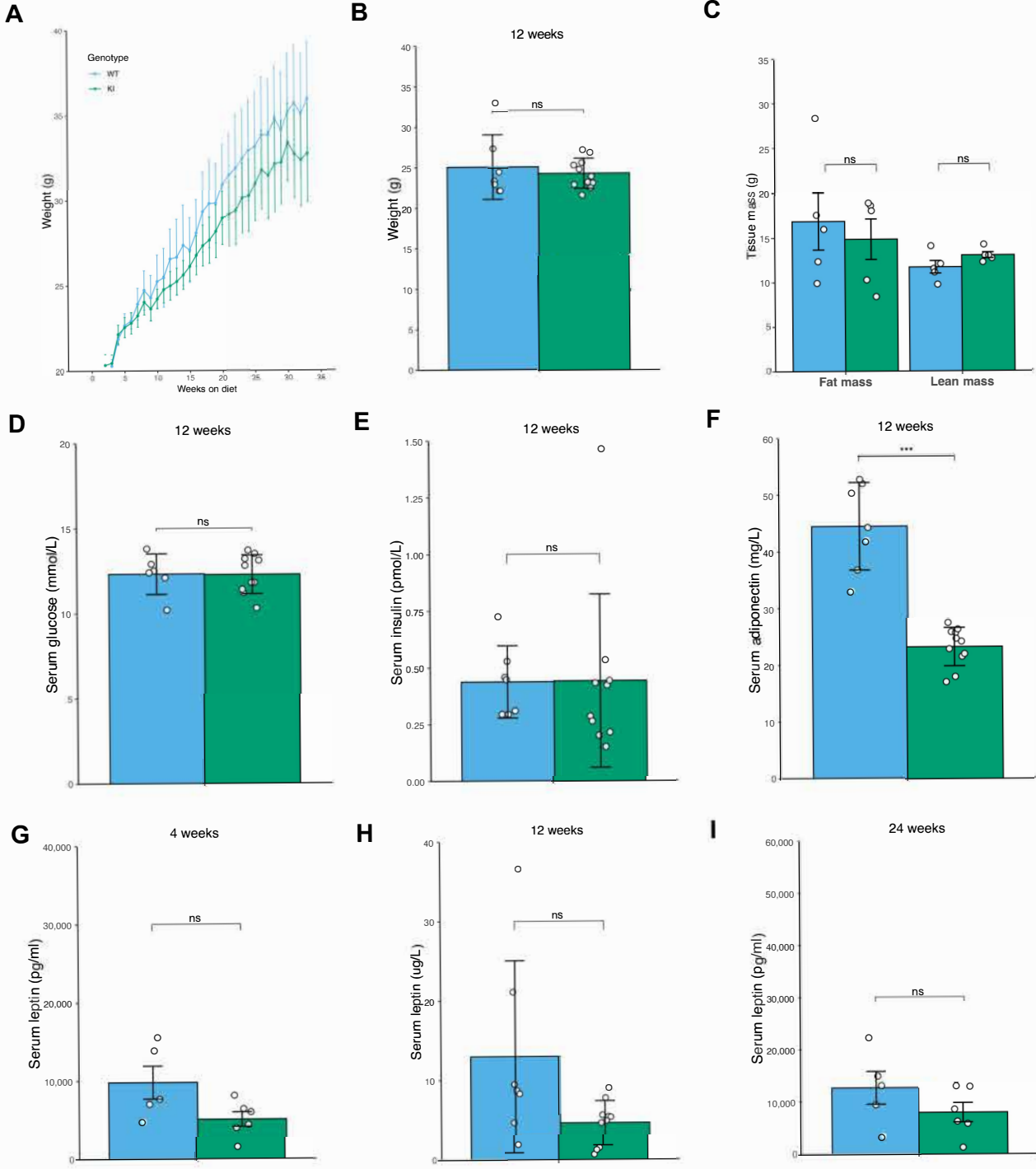
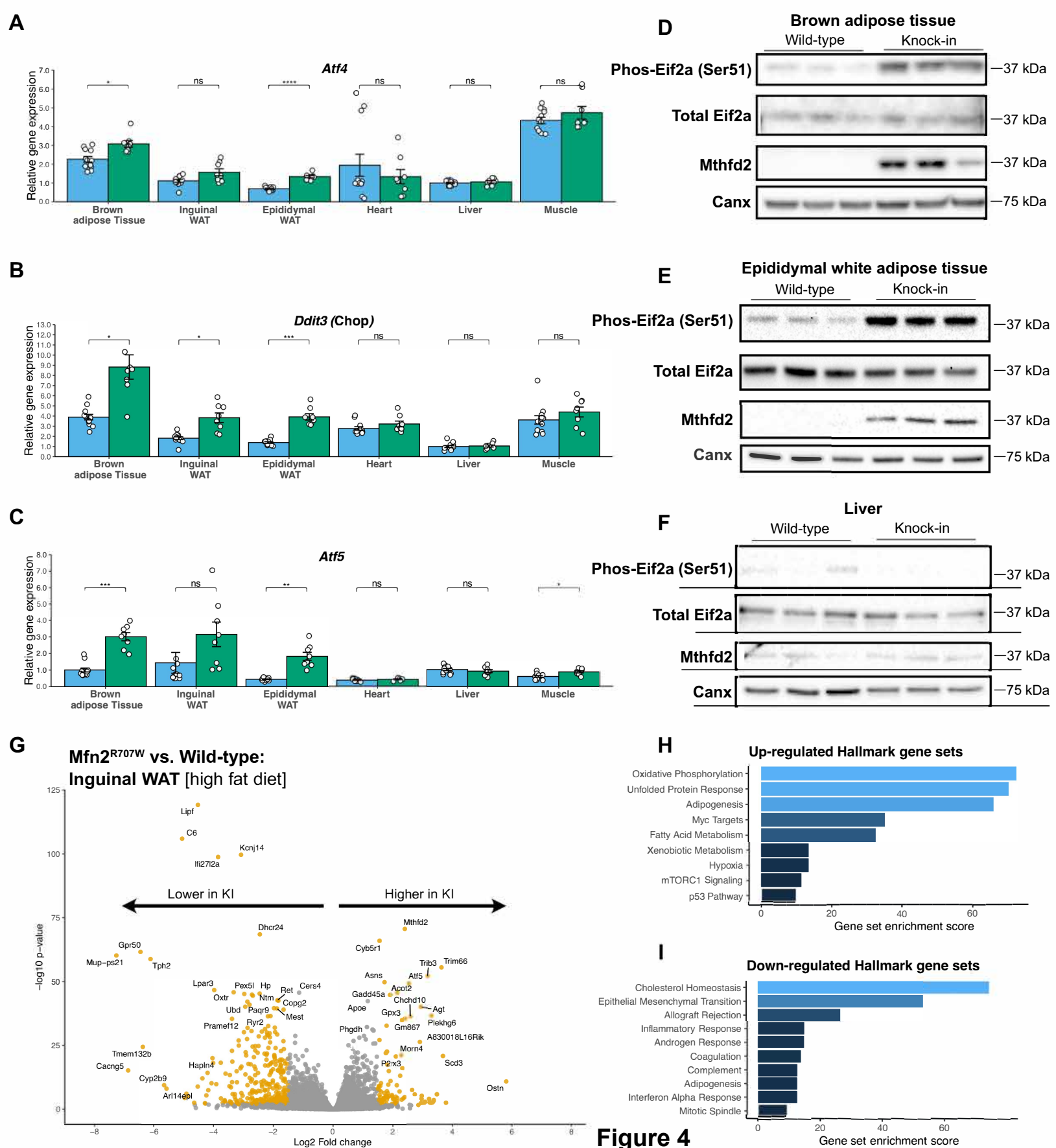
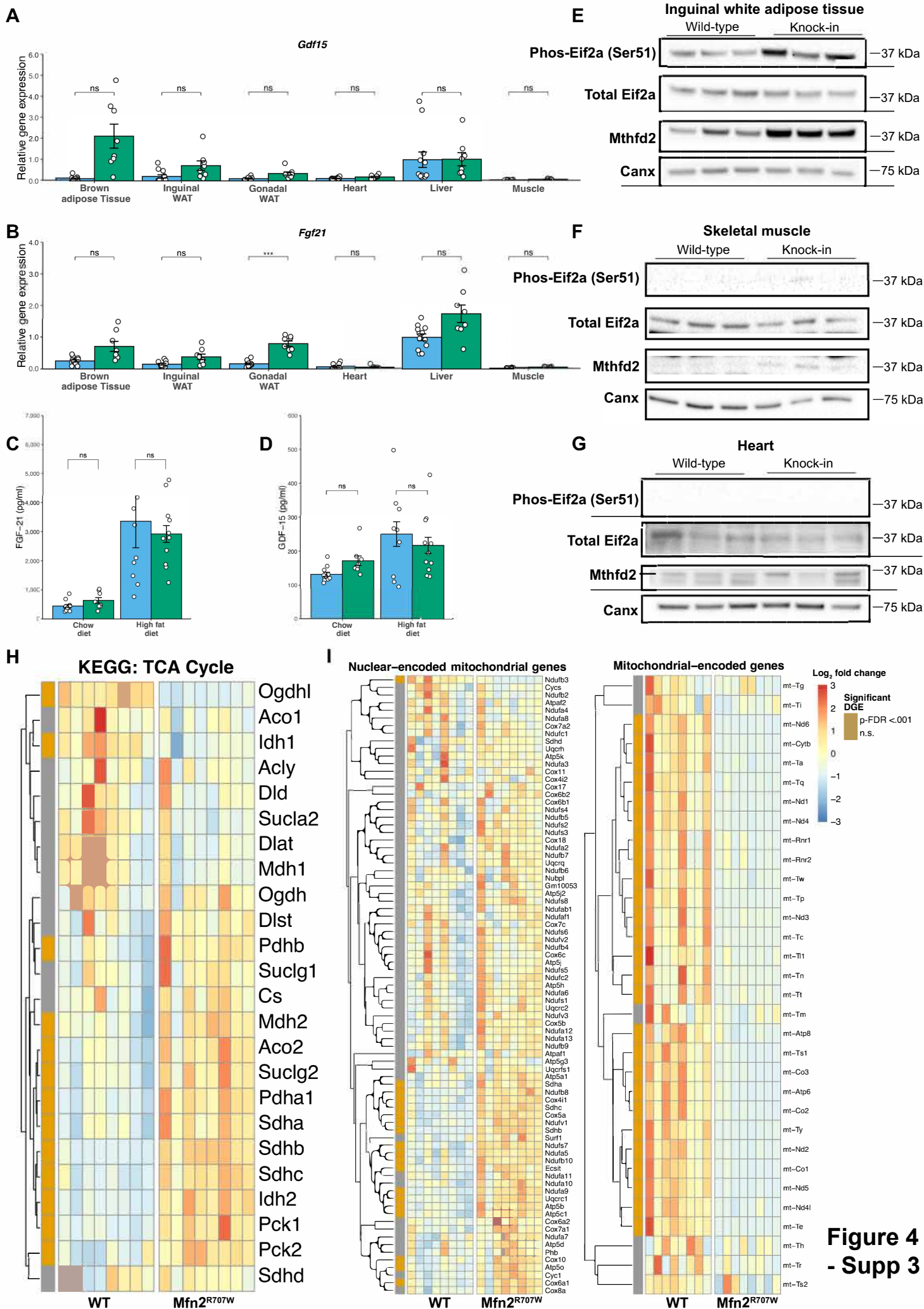


Figure 3 - Figure Supplement 2





**Figure 4
- Supp 3**

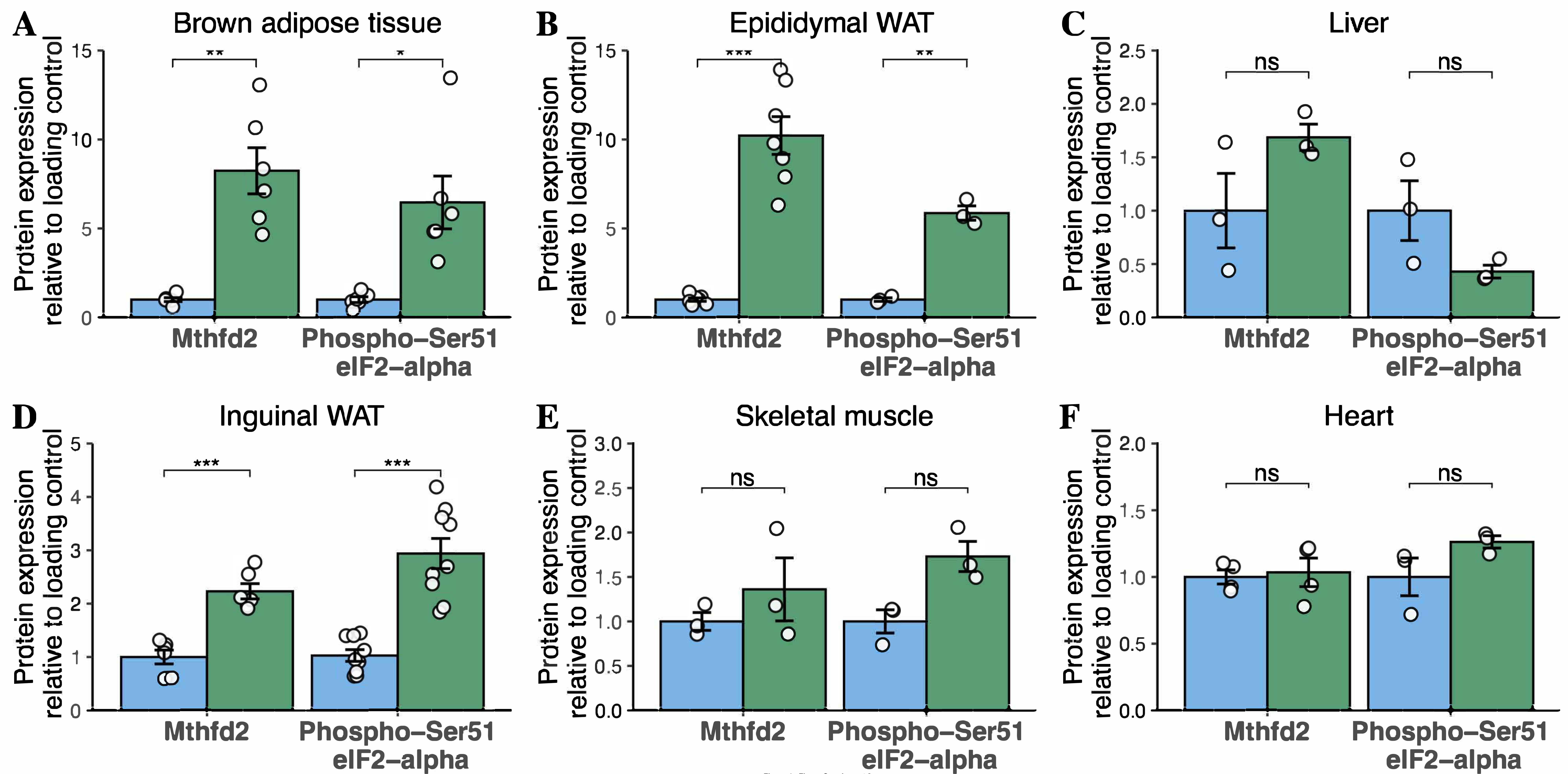


Figure 4 - Figure Supplement 2

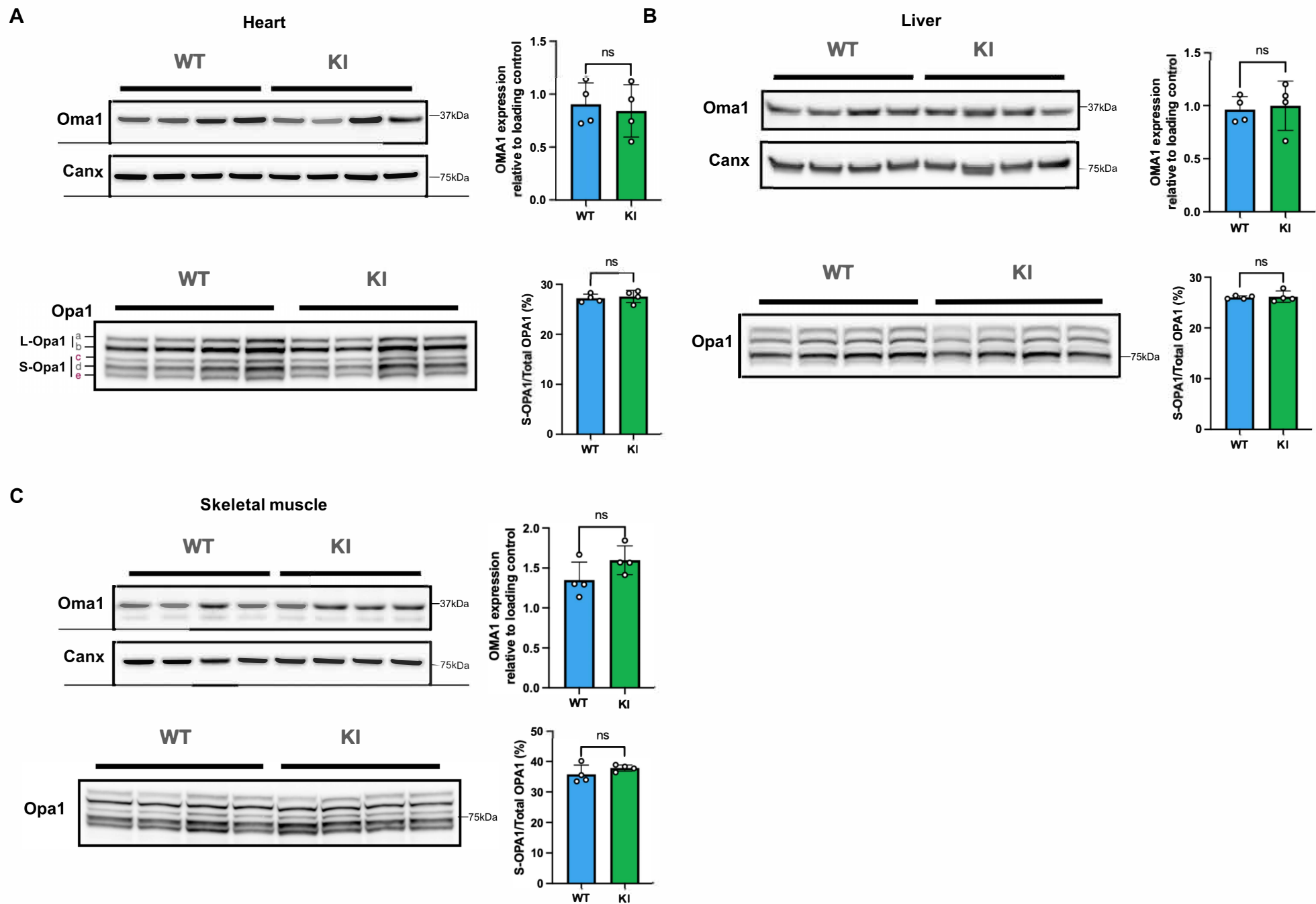


Figure 4 - Figure Supplement 3

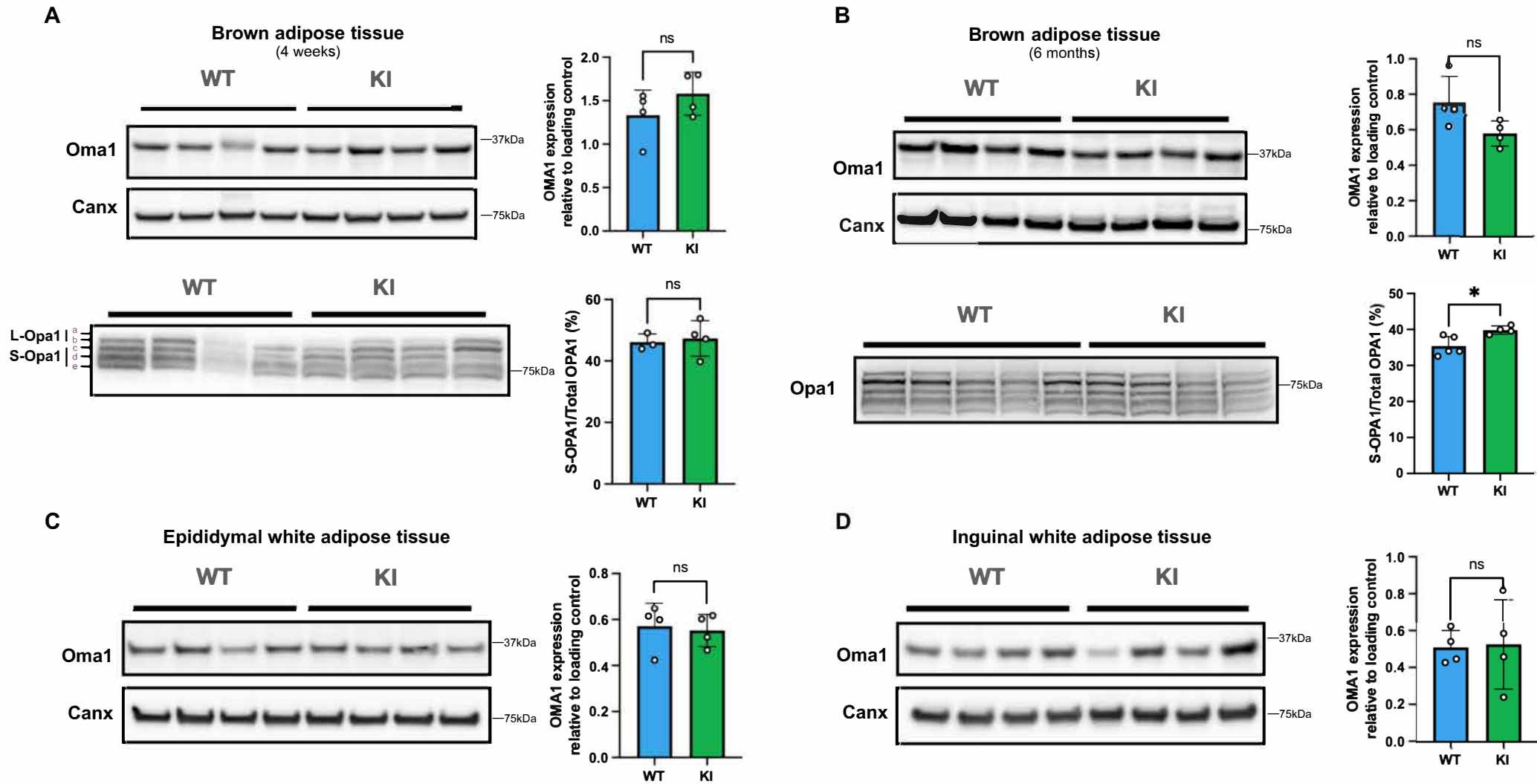


Figure 4 - Figure Supplement 4

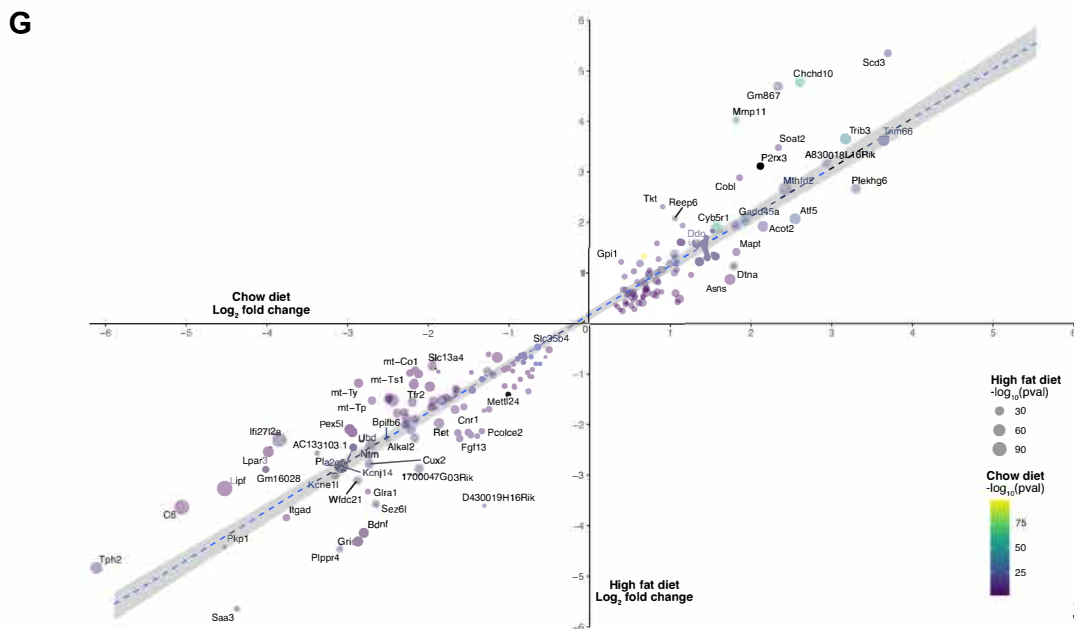
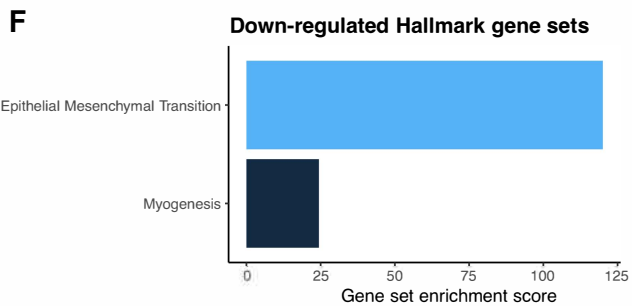
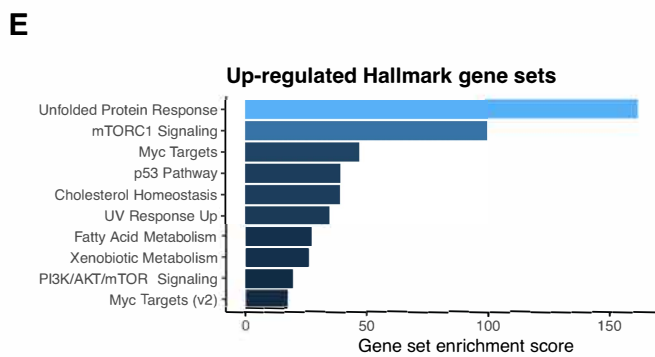
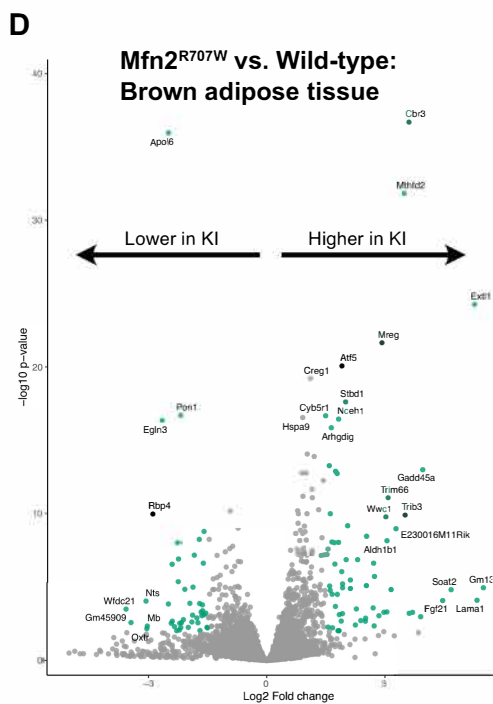
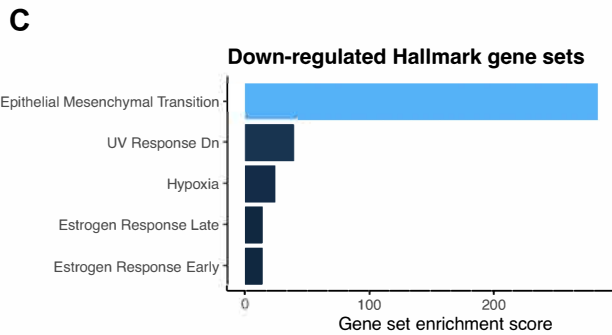
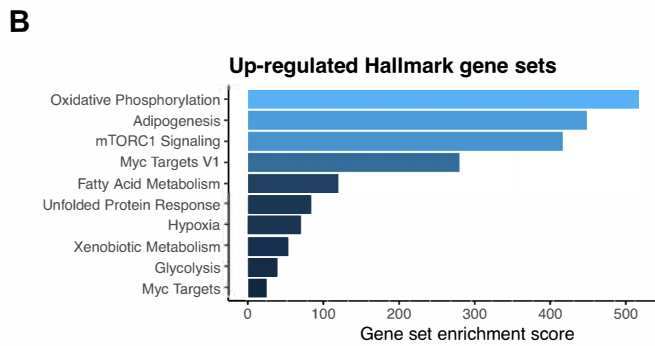
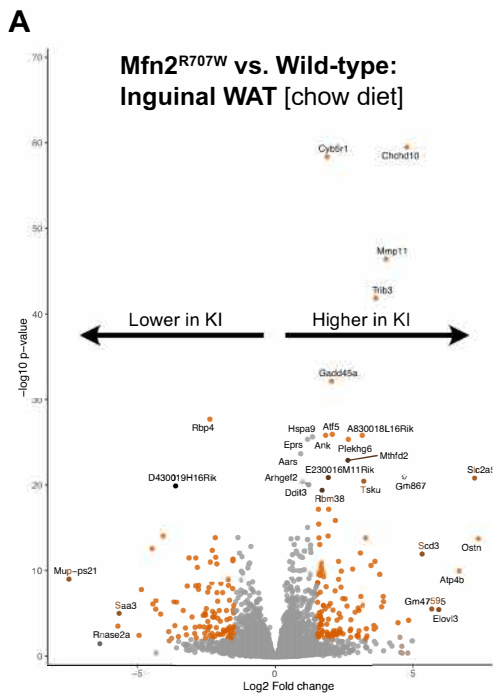


Figure 4 -Figure Supplement 5

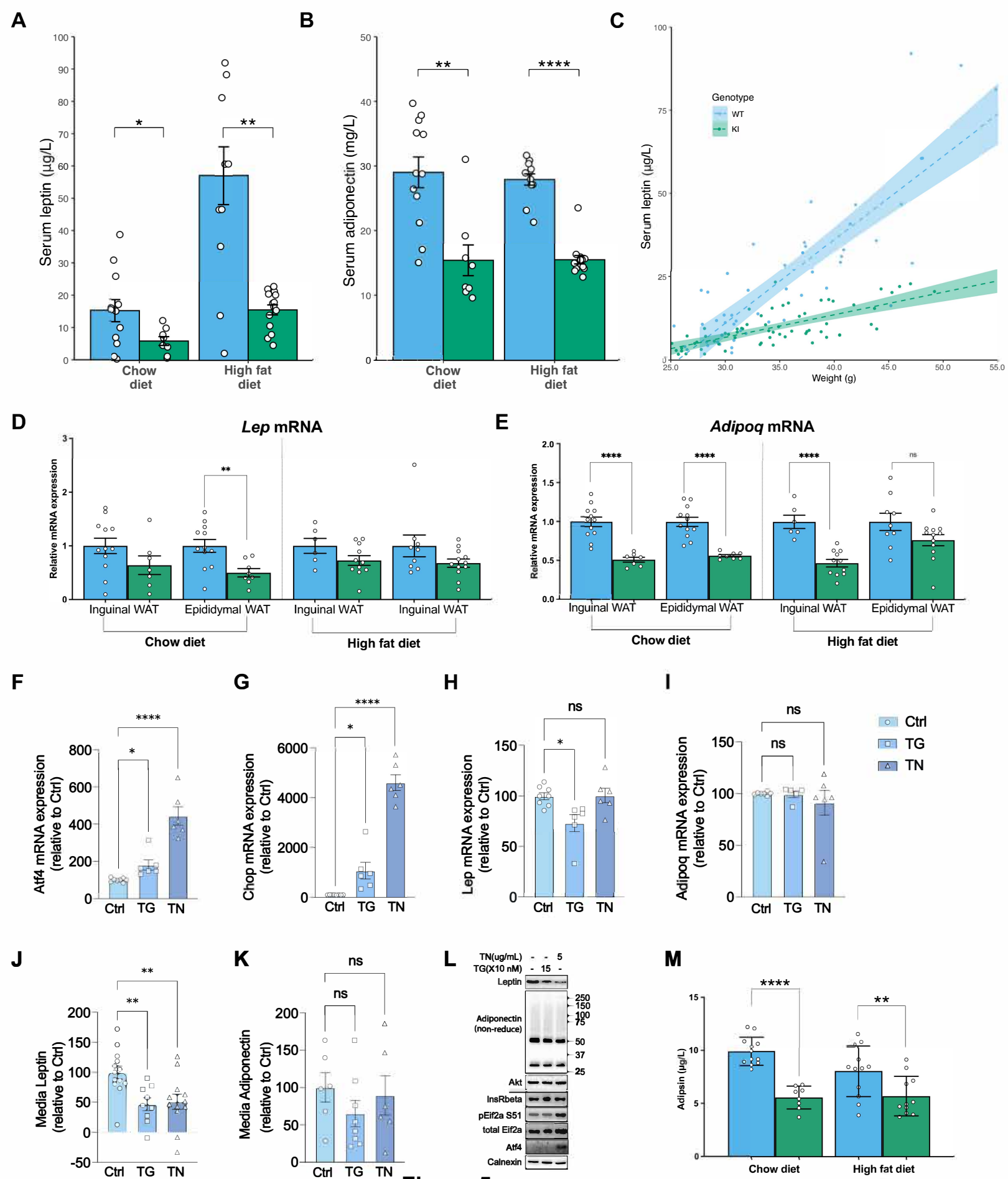


Figure 5

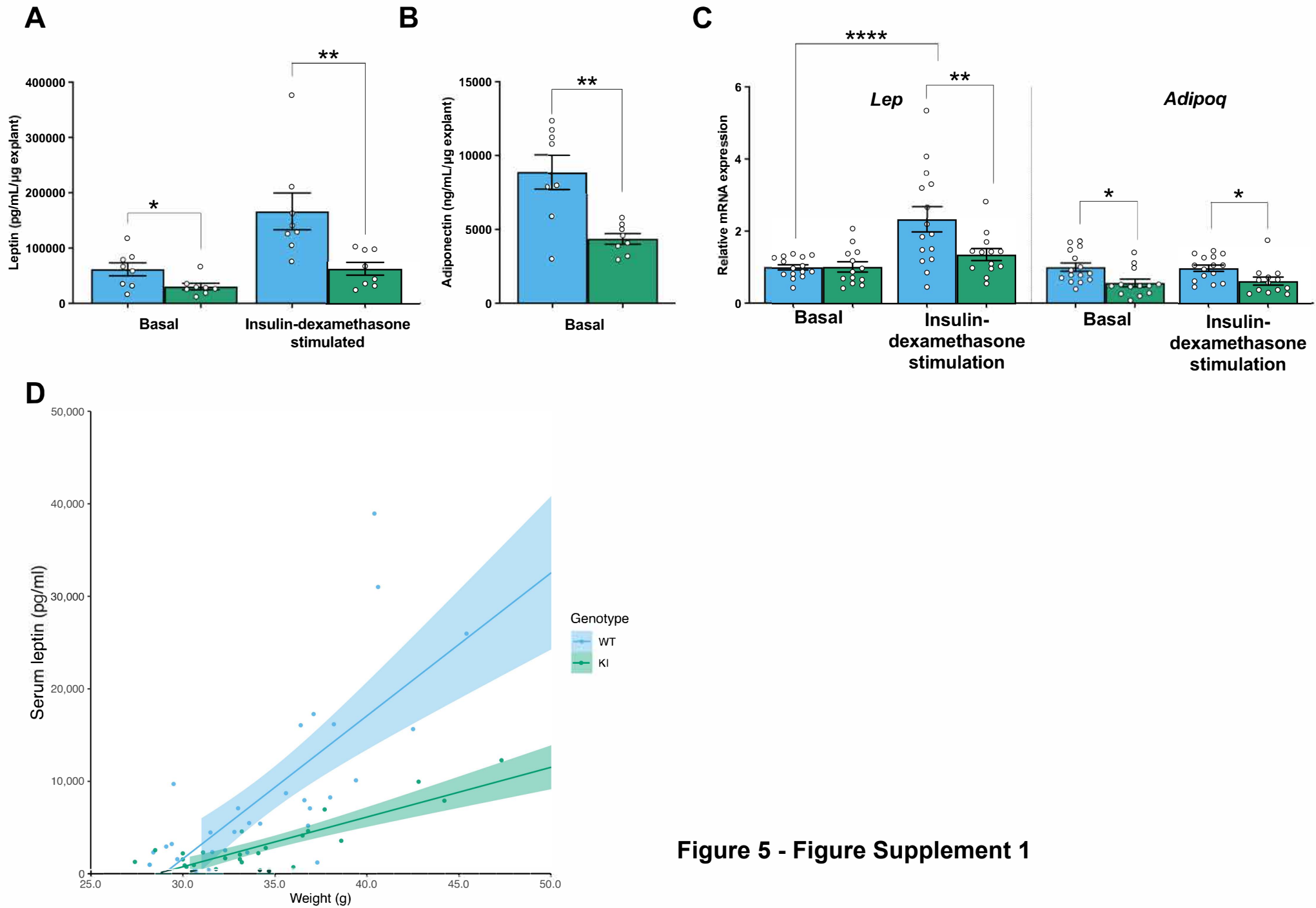


Figure 5 - Figure Supplement 1

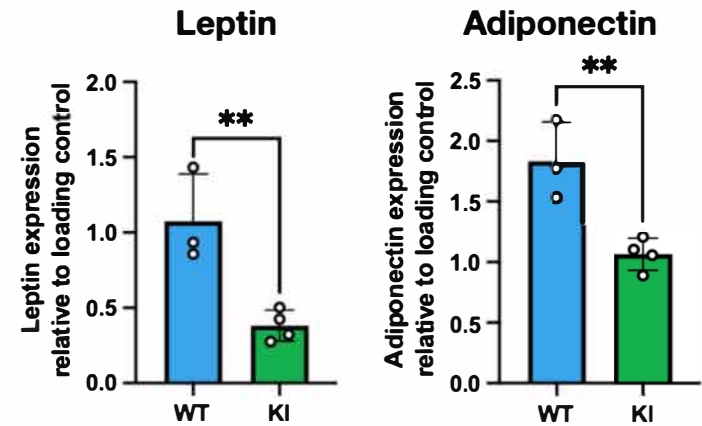
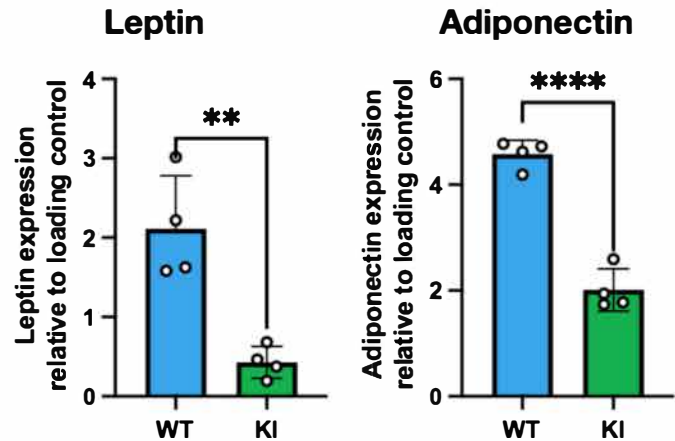
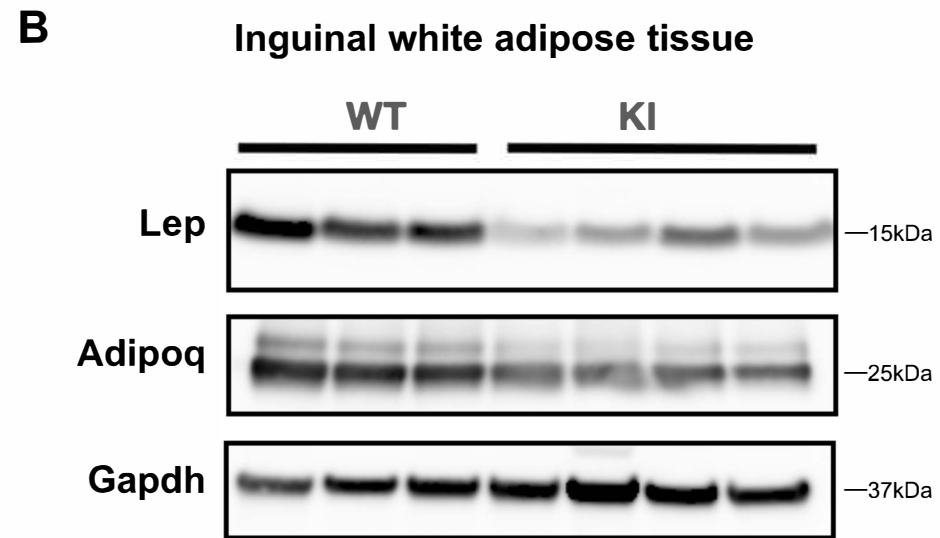
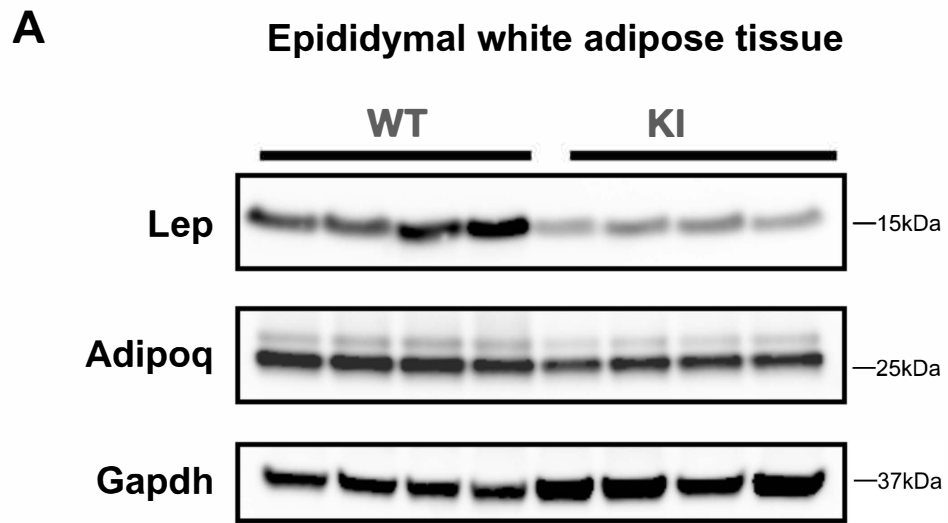


Figure 5 - Figure Supplement 2

Primary	Supplier	CatID	Concentration	Diluent	2 ^{ary}
Adiponectin	GeneTex	GTX80683	1 in 1000	5% milk	Mouse
AKT	Cell signalling	2920S	1 in 1000	5% BSA	Mouse
Anti-mouse HRP	Cell signalling	70765	1 in 5000	5% milk	N/A
Anti-rabbit HRP	Cell signalling	70751	1 in 5000	5% milk	N/A
Atf4	Cell signalling	11815S	1 in 1000	5% BSA	Rabbit
Beta-tubulin	Abcam	ab6046	1 in 1000	5% milk	Rabbit
Calnexin	Abcam	ab22595	1 in 5000	5% BSA	Rabbit
CitSynth	Abcam	Ab129095	1 in 1000	5% milk	Rabbit
Gapdh	GeneTex	GTX100118	1 in 5000	5% milk	Rabbit
Gapdh (for Opa1 blots)	Proteintech	10494-1-AP	1 in 1000	5% milk	Rabbit
InsR beta	Santa cruz	SC-57342	1 in 1000	5% BSA	Mouse
Leptin	Abcam	ab9749	1 in 1000	5% BSA	Rabbit
Mfn1	Abcam	Ab126575	1 in 250	5% milk	Mouse
Mfn2	Cell signalling	D2D10	1 in 1000	5% milk	Rabbit
Mthfd2	Proteintech	12270-1-AP	1 in 1000	5% milk	Rabbit
Oma1	Proteintech	17116-1-AP	1 in 1000	5% milk	Rabbit
Opa1	BD Biosciences	612606	1 in 1000	5% milk	Mouse
OXPPOS cocktail	Abcam	Ab110413	1 in 1000	5% milk	Mouse
Phos-Eif2a	Epitomics	10901	1 in 1000	5% BSA	Rabbit
Tom20	Abcam	Ab56783	1 in 500	5% milk	Mouse
Total Eif2a	D. Ron Lab	N/A	1 in 3000	5% milk	Rabbit

Supplementary File 1: Antibodies used in this study.

1

Primer	Sequence/TaqMan
36b4 Fwd	AGATGCAGCAGATCCGCAT
36b4 Rv	GTTCTTGCCCATCAGCACC
AdipoQ Fwd	GTTGCAAGCTCTCCTGTTCC
AdipoQ Rv	ATCCAACCTGCACAAGTTCC
Atf4 Fwd	GGGTTCTGTCTTCCACTCCA
Atf4 Rv	AAGCAGCAGAGTCAGGCTTTC
Atf5 TaqMan	Cat# Mm04179654_m1 (ThermoFisher Scientific)
B2m Fwd	ACTGATACATACGCCTGCAGAGTT
B2m Rv	TCACATGTCTCGATCCCAGTAGA
Ddit3 (Chop) Fwd	CCACCACACCTGAAAGCAGAA
Ddit3 (Chop) Rv	AGGTGAAAGGCAGGGACTCA
Fgf21 Fwd	CTGGGGGTCTACCAAGCATA
Fgf21 Rv	CACCCAGGATTTGAATGACC
Gdf15 TaqMan	Cat# Mm00442228_m1 (ThermoFisher Scientific)
gDNA_HK2_Fwd	GCCAGCCTCTCCTGATTTTAGTGT
gDNA_HK2_Rev	GGGAACACAAAAGACCTCTTCTGG
gDNA_Mt-Rnr2_Fwd	AACTCGGCAAACAAGAACCC
gDNA_Mt-Rnr2_Rev	CCCTCGTTTAGCCGTTTCATG
Hprt Fwd	AGCCTAAGATGAGCGCAAGT
Hprt Rv	GGCCACAGGACTAGAACACC
Lep3 Fwd	CCAGGAtgacaccaaaccct
Lep3 Rv	GATACCGACTGCGTGTGTGA
Mfn2 genotyping Fwd	AGTCCCTTCCTTGTCACTTAGT
Mfn2 genotyping Rv	ATCTCACAAGAAAGCGAAATCC

2 **Supplementary File 2:** Primer sequences used in this study. Fwd, forward primer; Rv, reverse primer.

3